UNIVERSITÀ DEGLI STUDI DI TRIESTE

Sede Amministrativa del Dottorato di Ricerca

FACOLTÀ DI SCIENZE MATEMATICHE, FISICHE, NATURALI

XXI Ciclo del Dottorato di Ricerca in

FISICA

The Silicon Strip Detector (SSD) for the ALICE experiment at LHC: construction, characterization and charged particles multiplicity studies.

(Settore scientifico-disciplinare: FIS/04 FISICA NUCLEARE E SUBNUCLEARE)

Dottorando :

Giacomo CONTIN

Coordinatore del Collegio dei Docenti :

Chiar.mo Prof. **Gaetano SENATORE**

Relatore e Tutore :

Prof. **Paolo CAMERINI**

ANNO ACCADEMICO 2007/2008

Riassunto

La presente tesi descrive le attività di ricerca legate alla costruzione, la caratterizzazione e la validazione del rivelatore a micro-strisce di silicio (SSD) per il sistema di tracciamento dell'esperimento ALICE presso il collisionatore LHC al CERN. Nel primo capitolo della tesi si introduce la fisica delle collisioni fra ioni pesanti e si descrivono le principali osservabili che saranno utilizzate dall'esperimento ALICE per studiare la formazione e la successiva evoluzione del Plasma di Quark e Gluoni.

Nel secondo capitolo è presentata una descrizione del rivelatore di ALICE e sono discusse in particolare le caratteristiche del sistema di tracciamento, di cui l'SSD è parte integrante, e le sue prestazioni in relazione alla fisica di ALICE.

La terza parte della tesi riguarda le attività correlate alla costruzione e alla caratterizzazione dell'SSD: dopo la produzione e i test di accettazione, è stata condotta un'indagine estensiva ed approfondita sui moduli difettosi, al fine di comprendere l'origine delle problematiche riscontrate e di elaborare soluzioni appropriate. Il lavoro effettuato ha permesso di recuperare numerosi moduli e di innalzare la qualità globale del rivelatore. Dopo le operazioni di assemblaggio, il rivelatore nella configurazione finale è stato completamente caratterizzato prima dell'installazione nel sito sperimentale. Una volta installato, le funzionalità dell'SSD e la sua integrazione in ALICE sono state infine verificate durante la fase di *commissioning*, attraverso un elevato numero di acquisizioni di dati di rumore e di raggi cosmici.

La caratterizzazione del rivelatore completo ha dimostrato l'importanza di un' efficace correzione hardware del *common mode* per l'efficienza e la qualità globali dell'SSD. A tal fine, gli effetti di questa particolare fonte di rumore sono stati studiati attraverso una serie di simulazioni. I risultati di questo studio sono presentati nel quarto capitolo della tesi e due algoritmi sono proposti per un efficiente trattamento e reiezione del rumore di common mode.

Infine, nell'ultimo capitolo viene descritto uno studio di fattibilità della misura

della molteplicità di particelle cariche con l'SSD. In vista della prima fase di acquisizione dati dell'esperimento ALICE, è stato simulato un campione di eventi protone-protone a 900 GeV di energia; l'efficienza di ricostruzione dei segnali di particella è stata studiata e misurata in funzione delle caratteristiche funzionali del detector. Infine, la correlazione tra i segnali ricostruiti nell'SSD e le osservabili fisiche simulate dal Monte Carlo è stata usata per caratterizzare l'interazione primaria.

Contents

Overview

The present thesis is focused on the construction, characterization and performance assessment of the Silicon Strip Detector (SSD) for the tracking system of the ALICE experiment at LHC. The first part introduces to the physics of heavy ions collisions and describes the main observables which are going to be studied with the ALICE detector as possible signatures of the onset of the Quark Gluon Plasma phase transition.

A description of the ALICE detector is presented in the second chapter, with particular emphasis on the tracking system, where the SSD plays an important role, and on its performances related to the ALICE physics topics.

The third part of the thesis deals with the activities related to the construction and characterization of the SSD: after the production and the acceptance tests, an extensive work was performed on the malfunctioning modules, in order to find out the origin of several defects and to develop proper solutions. Their application allowed to recover a fair number of modules and to enhance the global quality of the SSD. After the assembling operations, a complete characterization of the detector in the final configuration was performed before its installation in the experimental site. Once installed, it was tested and characterized during the commissioning phase, through a large set of noise and cosmic rays data acquisitions.

The characterization showed the relevance of a proper hardware common mode correction for the efficiency and overall quality of the SSD. In order to improve the SSD data quality, the effects of this particular source of noise were studied with a set of simulations. The results are presented in the fourth part of the present thesis; in addition, two different algorithms for an efficient common mode noise treatment and rejection are proposed.

In the last part of the thesis, the feasibility of a charged particles multiplicity measurement with the SSD was explored. In view of the first data taking phase of the

ALICE experiment, a 900 GeV proton-proton collisions sample was simulated, and the particles signals reconstruction efficiency was studied and measured as a function of the SSD quality, represented by the number of properly operating channels and their noise characteristics. Finally, the correlation between SSD reconstructed signals and the Monte Carlo simulated physical observables was used to characterize the primary interactions.

Chapter 1

The heavy-ion collisions physics

The Standard Model is the theory of the elementary particles and their fundamental interactions. This theory includes the strong interactions due to the color charges of quarks and gluons and a combined theory of weak and electromagnetic interactions. Proposed and developed since the 1960's, the Standard Model is today a well established theory applicable over a wide range of conditions: the high-energy physics has validated it and confirmed its predictions through a large variety of experiments.

In this context, the heavy ion physics is aimed at the application of this theory to complex and evolving systems of finite size, in order to understand the relations between collective phenomena and the microscopic laws of elementary-particle physics. In the sector of the strong interactions, the heavy ion physics studies the nuclear matter under conditions of extremely high temperature and energy density. In these conditions, the Standard Model predicts a new phase of the nuclear matter arising, where the quarks and the gluons are expected to be deconfined and to freely move. Moreover, the QCD lattice calculations predict that a phase transition toward this hot and dense state of matter should be accessible to experimental observations.

1.1 The phase transition

According to the Big Bang cosmological theory, a few microseconds after the Big Bang the early Universe was a very hot plasma of deconfined quarks and gluons. It evolved to its present state rapidly expanding and cooling, traversing a series of phase transitions predicted by the Standard Model. In these transitions, quarks and gluons became confined and the global features of our Universe, like the baryon asymmetry or the galaxy distribution originated. Today, the deconfined quarks and gluons are likely present in the core of the neutron stars, even if at lower temperature and higher density than in the early Universe; moreover, this plasma is not made of an equal mixture of matter and antimatter, but predominantly of matter.

The goal of the heavy ion experiments is to form such a phase colliding heavy ions at very high energy. In order to understand how the new phase forms, we can consider at first this picture, shown in fig. 1.1: composite nucleons with a finite spatial extension and made up of point-like quarks, if compressed, start to overlap above a critical density until each quark eventually finds within its immediate vicinity a considerable number of other quarks. It has no way to identify which of these had been its partners in a specific nucleon in the previous state at lower density. Therefore beyond a certain condition of high density, the concept of a hadron loses its meaning. At extreme densities, a medium constituted of unbound quarks forms [1].

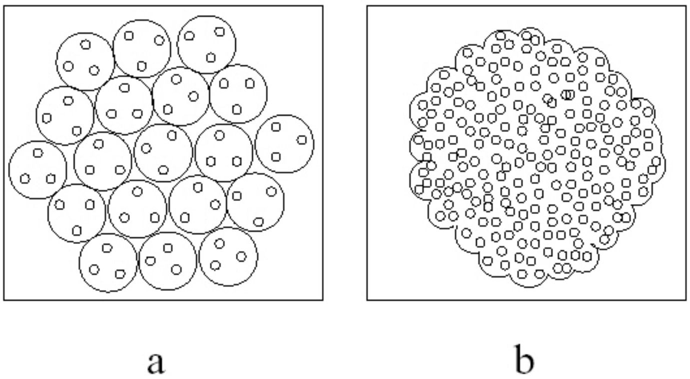

Figure 1.1: Pictorial view of the compression of the nuclear matter: the composite nucleons, with their finite spatial extension, are packed together (a); if compressed above the critical density, they start overlapping and the quarks can not identify their previous partners (b); the matter is thus deconfined.

In relativistic thermodynamics, higher densities can be obtained either by increasing the net baryon number[1], or by 'heating' the system, so that collisions between its constituents produce further hadrons. This leads to the phase diagram shown in fig. 1.2: for low values of temperature T and baryon density ρ_B, we have confinement and hence hadronic matter; for high T and/or ρ_B, deconfinement sets in

[1]The net baryon number N_B is the difference between the number of baryons and of antibaryons present in a system. The variation of energy due to an increase in the N_B is the baryochemical potential $\mu_B = \frac{\partial E}{\partial N_B}$. It increases with the baryon density ρ_B, thus it is an alternative way to express the baryon content of a system.

and we get a particular phase of the matter called the *Quark Gluon Plasma (QGP)* [2, 3, 4]. Compressing the nuclear matter at $T = 0$, its properties can be understood in terms of a degenerate Fermi quark gas.

By increasing T at low ρ_B, we are heating matter until it becomes a quark-gluon plasma. Strong interaction thermodynamics thus predicts the existence of new, deconfined states of matter at high temperatures and densities. In the following paragraphs, the creation of these states and its main features will be described.

Characteristics of QGP

Even before the formulation of the QCD, the existence of a phase transition to a new state of matter had been argued from the mass spectrum of resonances produced in hadronic collisions [5]. After the formulation of the QCD as an asymptotically free theory this observation has been related to a phase transition [6].

From QCD lattice predictions, the phase transition is expected at a critical temperature $T_c = 175$ MeV, corresponding to an energy density $\epsilon \approx 1$ GeV/fm^3. Starting from the ordinary nuclear matter, the ultra-relativistic heavy-ion collisions recreate the energy density conditions more favorable for the creation of this phase of coloured matter called the Quark Gluon Plasma (fig. 1.2).

As suggested by the extrapolations of the asymptotic high temperature behaviour of QCD in the region of the transition from hadronic to partonic matter, the QGP was expected to behave as an ideal non-interacting gas: instead the observation of large elliptic flow and jet quenching at RHIC seems to suggest a rapid thermalization of the dense matter created in relativistic heavy ion collisions.

This suggests that the hot and denser medium created in these collisions is still strongly interacting. Also the early non-perturbative study have shown that the high temperature phase of QCD is far from being simply an ideal quark and gluon gas; even at temperatures $T \approx (2-3)T_c$ large deviations from the ideal gas behavior have been deduced [7]. In order to compare the new scenario that should be accessible at LHC, the expected experimental condition sand the fireball characteristics are compared with the ones estimated at SPS and RHIC in table 1.1.

Deconfinement and chiral symmetry restoration

The phase transition from the hadronic matter to the QGP affects the masses of the quarks, due to the partial chiral restoration that takes place in this phase. When

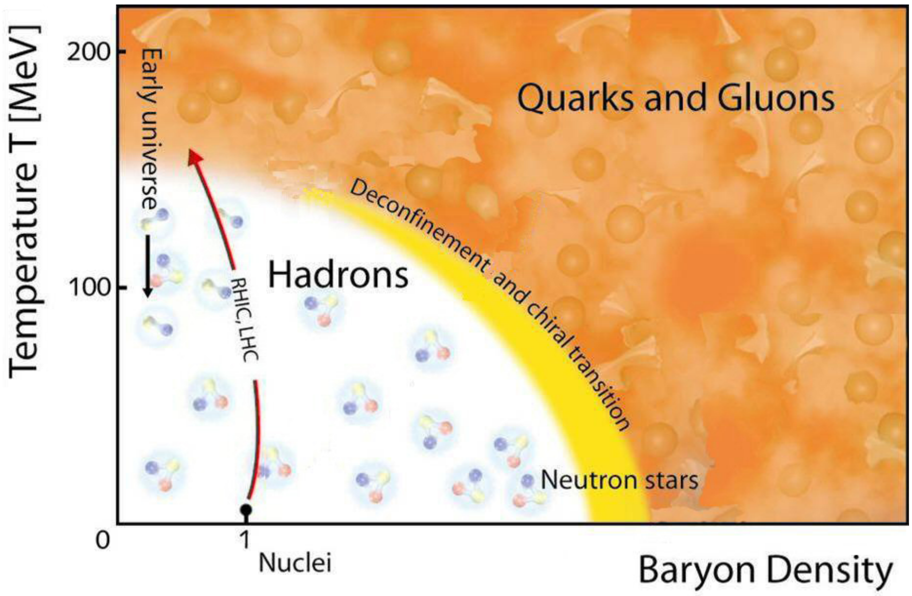

Figure 1.2: The nuclear matter phase diagram. For low temperature and baryon density the matter is in the ordinary nuclear conditions. Increasing the density and/or the temperature a phase transition to the Quark Gluon Plasma should occur. Moving along the axes, the matter should reach respectively the conditions that should be present in the neutron stars core (high density) and that presumably interested the matter in the Early Universe, few microseconds after the Big Bang (high temperature). The red arrows show approximately the range of temperature and density that studied by the RHIC and LHC experiments.

confined in hadrons, the quarks 'dress' themselves with gluons to acquire an effective constituent quark mass of about 300 MeV (resulting as the equivalent to 1/3 of the proton or 1/2 of the ρ-meson mass). On the other hand, the basic bare quarks in the QCD Lagrangian are almost massless, so that the mass of the constituent quarks in the confined phase must be generated spontaneously through the confinement interaction. Hence when deconfinement occurs, this additional mass is likely 'lost' and the quarks go back to their intrinsic *bare* mass [1].

A Lagrangian with massless fermions possesses chiral symmetry; this allows a decomposition of the quarks into independent left- and right-handed massless spin one-half states, which for massive fermions become mixed. For massless quarks, confinement must thus lead to spontaneous breaking of chiral symmetry, deconfinement to its restoration. Hence the mass shift transition in QCD is often referred to as chiral symmetry restoration. It's important to stress that it does not necessarily coincide with deconfinement: when the hadrons are dissolved into quark constituents, the free and now coloured quarks may still interact to form coloured bound states.

		SPS	RHIC	LHC
$\sqrt{s_{NN}}$	TeV	0.017	0.2	5.5
T/T$_c$		1.1	1.9	3-4
ϵ	GeV/fm^3	3	5	15-60
τ_{QGP}	fm/c	≤2	2-4	≥10
V$_f$	fm^3	few 10^3	few 10^4	few 10^5

Table 1.1: Experimental conditions and QGP characteristics expected at LHC, compared with the corresponding values estimated at SPS and RHIC.

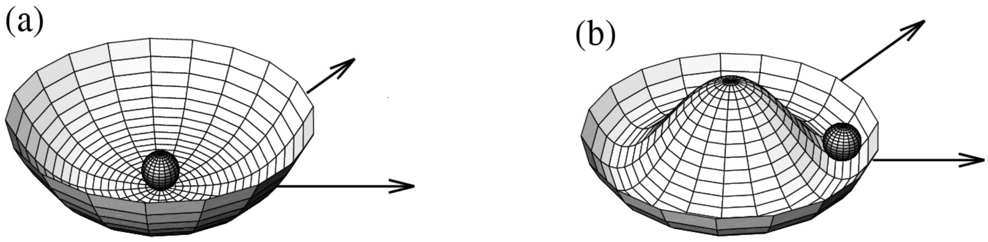

Figure 1.3: Pictorial view of the spontaneous breaking of the chiral symmetry. The quark, represented by the sphere, tends to occupy the minimum energy state: in the (a) configuration, it correspond to a symmetric state; in the (b) configuration, representing the confined quark in a nucleon, the parton is forced to break the symmetry and occupies an asymmetric state [8, 9].

Thus at low temperature and high density, the quark triplets in nucleons, once deconfined, might choose to recombine into massive coloured quark pairs (*diquarks*). When the density is increased further, the diquarks would break up into the massless basic quarks.

This results in a three-phase picture of strongly interacting matter, with hadronic matter as confined phase, then deconfinement, followed by a phase consisting of massive coloured diquark systems, and finally, after chiral symmetry restoration, a plasma of coloured massless quarks and gluons.

1.2 The Lattice QCD predictions

Even from simple phenomenological models it is possible to define the critical temperature $T_c \sim 170$ MeV and the critical energy density $\epsilon_c \sim$1 GeV/fm^3. Anyway, it is necessary to study the quark matter phase with the correct theory for interactions of quark and gluons, namely the QCD. Moreover, due to the long range of the interaction, their non-perturbative nature needs to be treated with QCD calculations on a space-time lattice.

Although the lattice calculations are affected by systematic errors, which are caused by the finite lattice cutoff and the use of quark masses larger than those in nature, they have achieved important results in the study of the phase transition: in particular, for zero baryochemical potential ($\mu_B = 0$), they expect it to occur at the critical temperature $T_c = 175 \pm 15$ MeV; the influence of the non-zero baryochemical potential expected at LHC is anyway estimated to be very small.

Moreover, the estimates of the order of the transition and of the critical temperature depending on the number of flavours and the values of the quark masses indicate that in the more realistic limit of 2 zero mass quarks plus the s quark, the transition is a crossover at zero baryochemical potential.

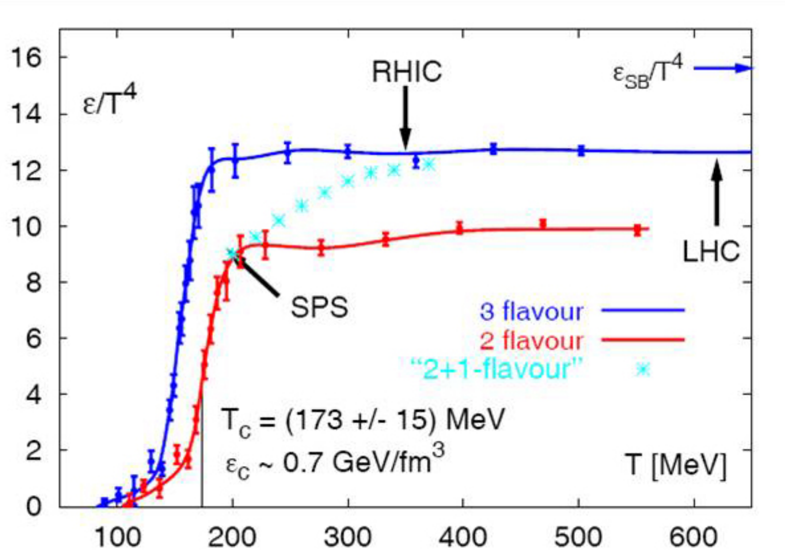

Figure 1.4: The energy density (b)in QCD with 2 and 3 degenerate quark flavours as well as with two light and a heavier (strange) quark. The arrow on the right-side ordinates show the value of the Stefan-Boltzmann limit for an ideal quark-gluon gas.

Order of the transition

From the QCD predictions, the phase transition should be of second order in the chiral limit of 2-flavour QCD, and of first order for 3-flavour QCD; on the other hand, in the case of the physically realized quark-mass spectrum, it is likely to be only a rapid crossover. This crossover can however take place in a narrow temperature range, which makes the transition between the hadronic and plasma phases still well localized. For this reason, the energy density rises rapidly near the crossover temperature. In fig. 1.4 the results of the lattice calculations are shown for what concerns the energy density in the limit of 2 and 3 zero mass quarks, as well as of 2 light and a heavier quark [10].

1.3 The Bjorken picture.

The heavy ions experiments like ALICE at the LHC are aimed at the creation of the QGP phase through the collision of heavy nuclei at very high energy. In the collisions, the density of matter is increased as far as possible beyond the ordinary nuclear matter density ($\rho_0 = 0.17$ nucleons/fm^3); while the energy increases, the nuclei penetrate each other bringing the matter form highly excited states to a quark gluon plasma: at the LHC energy case, the colliding nuclei pass through each other, leaving behind them the hot and dense matter that eventually decays into hadrons.

After the collision, the high energy density allows to turn on the degree of freedom normally hidden in the ordinary nuclear matter that successively turn off during the expanding and cooling down phase. The different stages of the event evolution can be qualitatively described by the picture formulated by Bjorken [11, 12]. In fig. 1.5 it's possible to follow this space-time representation of the event, from the collision to the final state:

1. At $t = 0$ the two nuclei collide: they are Lorentz contracted, thus the longitudinal coordinate of all the nucleons is the same.

2. During the *pre-equilibrium phase* the system reaches the maximum energy density, forming a not yet thermalized system of quark and gluons into a volume of some tens of fm^3; prompt leptons and photons can be emitted.

3. Then, thanks to the interactions among the partons, the system starts to thermalize: in these conditions and before the energy density drops below the critical value, the quark-gluon plasma forms and the matter deconfinement takes place, at a time estimated of order 1 fm/c after the collision (*QGP phase*); direct leptons and photons and hard jets are produced.

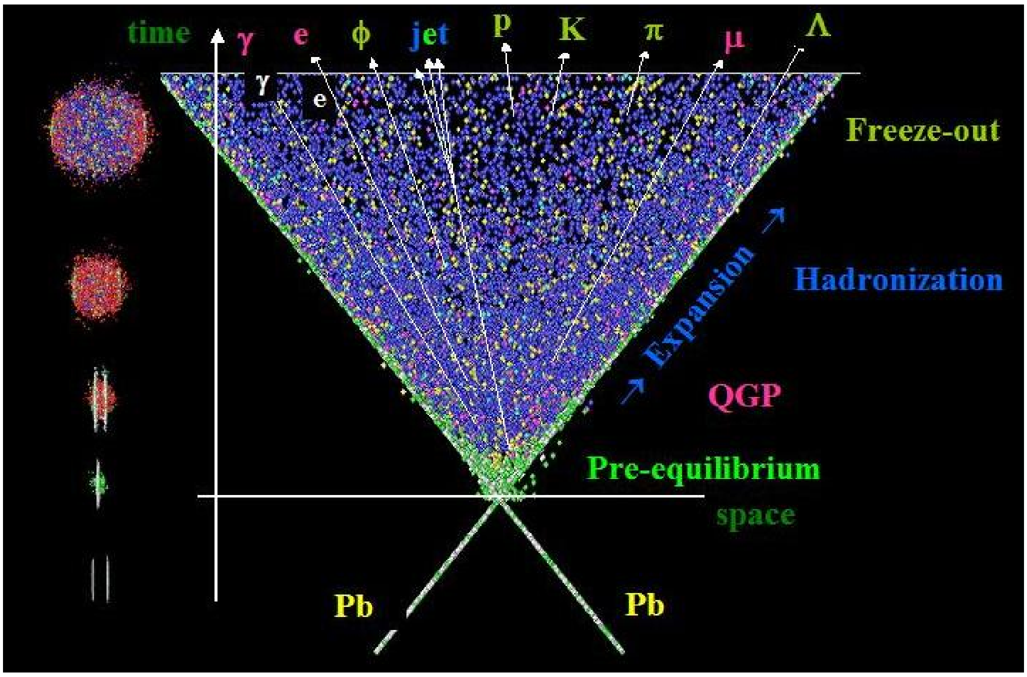

Figure 1.5: The space-time evolution of the heavy-ion collision. The various stages of the collision, drawn on the left part of the figure, are described, moving along the down-up direction, by the space-time representation and indicated with the conventional names on the right; on top, the particle types produced in the different stages of the evolutions are summarized. See the test for a more detailed description of the process as predicted by Bjorken.

4. The partons from different nucleon-nucleon collision rescatter leading to local thermal equilibrium and generating a thermodynamic pressure which brings to a collective expansion of the matter; the system cools down and the surface, already at a temperature below T_c evaporates into a hadron gas (*hadronization stage*).

5. The generated hadrons stop to interact $\sim$ 20 fm/c after the collision: the evaporation is completed and the hadron gas, now expanded in a region of about 10^4 - 10^5 fm^3 around the interaction point, should have reached its final chemical composition; the final hadrons produced in this *freeze-out stage* of the event move toward the detectors.

1.4 The QGP signatures

Since it is impossible to directly observe this short lived ($\sim$ some fm/c) QGP system, the HI experiments like ALICE take the challenge to study the different typologies of observables that would confirm the existence and the properties predictions by the theory for this matter phase and for the event evolution described before.

The signatures of the QGP can be divided in different categories, related to the different stages considered by the evolution picture described before: the deconfined medium (QGP), a possible interacting hadronic medium, and the final hadronic state [13]. The main direct hard probes of the creation of the QGP phase are:

- Hard emission of thermal dileptons and photons. These are a sort of *internal* probe: they are produced by the QGP itself and are not affected by the subsequent states of the medium, since they undergo only weak and electromagnetic interactions after their formation; therefore, they bear the imprints of the bulk properties of the early stages of the interaction and can be used as a thermometer of the medium, since they are produced also by the confined matter. However, this is also the main drawback of this study: it is very difficult to separate thermal dileptons and photons from the abundant hadronic production; moreover, the presence of a *prompt* component produced by early hard parton interactions in the primary and pre-equilibrium stages, has to be taken into account and separated as well.

- Production of quarkonium states (J/Ψ, Υ) in the primary parton collisions. These states are produced before the existence of any medium but their dissociation is possible only in a deconfined medium; their observed behaviour indicates therefore whether the subsequent medium was deconfined or not, resulting in a sort of *external* probe.

- Jet quenching. The energy loss of partons passing through the hot deconfined medium is expected to be larger than through the hadronic matter.

Informations about the evolution of the hadronic system, in particular about its last stage, where the hadrons are still interacting, can be provided by:

- In-medium modifications of resonances observable in their decays. The changes of their masses or widths can originate from the large rescattering cross section in the medium, where the final state interactions influence in particular the hadronic decays. The study of these changes should be useful to distinguish between different *expansion* and *freeze-out* scenarios.

The expected QGP probes produced in the hadronization phase, the so called *soft probes*, which appear when the density of the medium has dropped sufficiently to allow the existence of hadrons, are:

- Strangeness enhancement. A hot QGP should contain the different quark species in almost equal amounts, which, if preserved up to hadronization, should result in more abundant strangeness production than observed in p-p interactions, where the strange quark abundance is suppressed.
- Collective flow and transverse momentum broadening. Compared to p-p interactions, a hot initial QGP could lead to more pronounced expansion and specific expansion patterns.

In this sections, the main heavy-ion observables that will be measured and studied by the ALICE experiment as probes and signatures of the QGP are discussed, giving an overview of the present results, achieved by the previous experiments at SPS and at RHIC, and the perspectives for these topics research. Where necessary, the measurements of the same observables in proton-proton collisions will be discussed as a reference for nucleus-nucleus collisions. First of all, we will start from the study of one of the most important global properties of the event: the particle multiplicity.

1.4.1 Particle multiplicity

In the heavy-ion collisions, it's possible to determine the initial geometry of the collision and the way in which the initial available centre-of-mass energy is redistributed in the accessible phase space studying the global properties of the final state. The collision geometry, moreover, is an essential prerequisite to the study of any physics observable.

One of the most important observables that ALICE is expected to measure already from the first days of collisions is the charged particles multiplicity. The quantities related to the event geometry, like the impact parameter b, the number of participant nucleons in the interaction N_{part} and the number of nucleon-nucleon collisions, can be extracted from the measurement of the multiplicity in a rather

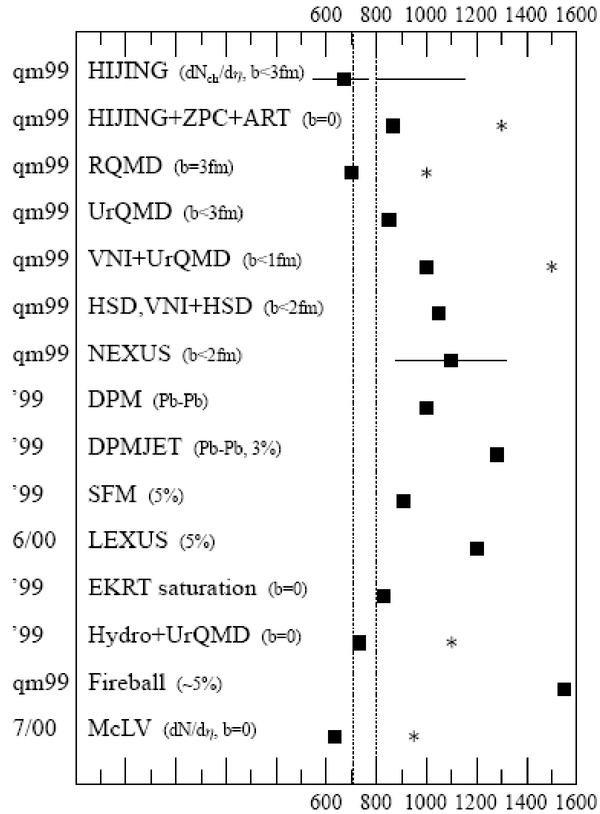

Figure 1.6: Predictions for $\mathrm{dN}_{ch}/\mathrm{d}y$ in Au+Au collisions at y=0, $\sqrt{s}$ = 200 AGeV, from different models before the appearance of the first RHIC data. The extrapolations vary widely, mostly overestimating the experimental result of less than 600 charged particles. The table is here shown to emphasize the variety of the extrapolations of the charged particle multiplicity, depending on the used model. For certain predictions (those marked by an asterisk), the 2/3 correction is applied to the total multiplicity prediction in order to obtain the charged particle one (*taken from [14]*).

model-independent way. Reconstructing the centrality of the collisions, it is possible to select and study in particular the collisions where the maximum energy density is reached; moreover, once determined the centrality of the collision, it's possible to study the physics observables as a function of b or N_{part} in order to locate the onset of the phase transition from the hadronic to the deconfined matter. A complete characterization of the event will be finally provided by the information about the temperature and the energy density reached in the collision, that can be inferred from the charged particle rapidity density $\mathrm{dN}_{ch}/\mathrm{d}y$ and the p_t distributions.

However, the multiplicity and another important global observable like the total transverse energy can not be calculated starting from the QCD Lagrangian, because the soft non-perturbative QCD and the processes on the large scale $R_A \approx A^{1/3}$ fm dominate these observables. Due to these causes, it is also difficult to extrapolate the expected multiplicity in the ALICE events from previous results obtained at SPS or even at RHIC. As already experienced before the start-up of RHIC, the extrapolations from SPS measurements at $\sqrt{s}$ = 20 to the 200 GeV RHIC energy varied widely [14], as shown in fig. 1.6, mostly overestimating the result. Even after the RHIC data, the extrapolations to 5500 GeV (ALICE) are still difficult.

In the following paragraphs the expectations of the particle multiplicity in proton-proton and in nucleus-nucleus collisions will be discussed.

Multiplicity in p-p collisions

The ALICE experiment will start measuring the charged particle multiplicity in proton-proton events, as a benchmark for the further study in A-A events but also to extract informations about the phase transition to QGP from the multiplicity fluctuations.

From the observations, the hadron rapidity density can be parametrized for charged particles by a quadratic polynomial in $\ln(s)$. At SPS energies, $\sqrt{s} = 20$ GeV, the charged-particle rapidity density is about 2 at $y = 0$; at RHIC energies, it is about 2.5; and extrapolates to about 5.0 at ALICE energies, as shown in fig. 1.7.

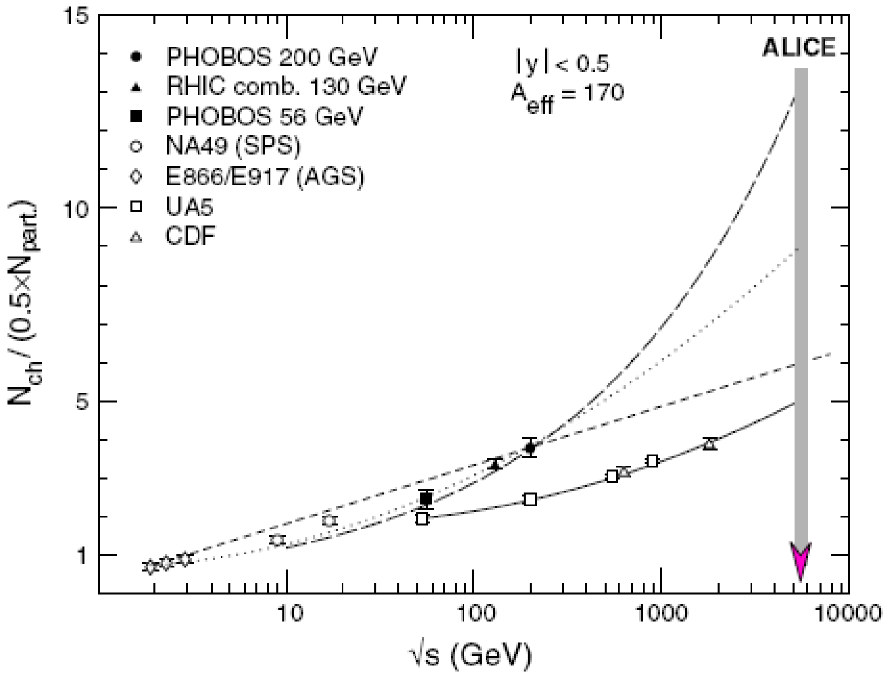

Figure 1.7: The charged-particle rapidity density per participant pair as a function of centre-of-mass energy for A-A and p-p collisions. The lines fit the experimental data with different parametrizations, substantially quadratic polynomials in $\ln(s)$. The dotted curve is $0.7 + 0.028\ln^2(s)$ and provides a good fit to data below and including RHIC, and predicts, for Pb-Pb collisions at LHC (A_{eff}=170), $N_{ch} = 9 \times 170 = 1500$. The long dashed line is an extrapolation to LHC energies using the saturation model (see paragraph 1.4.1) [15].

The general behaviour of multiplicity distributions in p-p collisions in full phase space is uncertain, so it is not safe to extrapolate to higher energies or to full phase space for distributions measured in limited rapidity intervals only.

As mentioned before, the study of the particle multiplicity in p-p collisions at LHC energies will be anyway interesting by itself: it will measure very high-multiplicity events with charged-particle rapidity densities at mid-rapidity in the range 60-70, i.e. about 10 times the average. This event class may give access to initial states where new physics such as high-density effects take place. Finally, local fluctuations of multiplicity distributions in momentum space can be a possible signature of a phase transition to QGP.

A study dedicated to the charged particle multiplicity measurement of the first ALICE p-p events at $\sqrt{s_{NN}} = 900$ GeV performed with the Silicon Strip Detector is described in the last chapter of this thesis.

Multiplicity in A-A collisions

According to the saturation model, the multipliticy in A-A collisions can be estimated on the basis of dimensional arguments [16, 17]. The basic idea of the parton saturation model can be intuitively explained considering the Lorentz contraction of a nucleus boosted to a large momentum: the partons sit on a thin sheet in the transverse plane and each one of them occupies the transverse area π/Q^2 determined by its transverse momentum Q by the uncertainty principle. The entire transverse area of the nucleus is $S \sim \pi R_A^2$. Above a certain number, the partons begin to overlap in the transverse plane and start interacting with each other. This happens when the transverse momenta of the partons are on the order of $Q_s^2 \propto \frac{N_A}{R_A^2} \propto A^{1/3}$, which is called the *saturation scale*. In the saturation regime, the multiplicity of the produced partons should be proportional to $N_s \propto Q_s^2 R_A^2 \propto A$. This leads, for the expected $Q_s = 2$ GeV at LHC, to an estimation of

$$N \propto Q_s^2 R_A^2 \propto (2\,GeV(200)^{1/3} fm)^2 = 3500 \tag{1.1}$$

produced particles. The theoretical models of the LHC multiplicity basically aim to determine the energy dependence of Q_s in order to achieve more accurate estimation of its value.

The study of heavy-ion collisions allows to discover new effects ascribed to the new scale $A^{1/3}$ fm and not observed in p-p collisions. Thus the measured multiplicities of p-p and A-A collision have to be compared. This comparison can be easily done computing the number of participants in the collision N_{part}, which is 2 in the case of a p-p collision, and increases up to $2A$ in central A-A collisions, and can be estimated as a function of the impact parameter b. We can observe that a p-p collision at $\sqrt{s} = 200$ GeV produces 2.5 particles, while an A-A collision produces 3.8 particles (+50%). Extrapolating at the ALICE energies, up to $\sqrt{s} = 5.5$ TeV, while a p-p collision produces 5 particles, an A-A event produces 13 particles per nucleon pair (+160%). A prediction for the total multiplicity in an A-A event with $A_{eff} = 170$ is N $\approx 13 \times 170 \approx 2200$.

However, when theoretical predictions are compared with experimental observations, some corrections have to be taken into account:

- the experiments measure the charged multiplicity, which is approximately 2/3 of the usually predicted total multiplicity;
- the experiments measure the pseudorapidity distribution, where the theory considers the rapidity distribution;
- the centrality of the collision has to be accurately estimated in order to know the A_{eff};
- the multiplicity is defined at a certain stage of the evolution of the event.

These corrections have been applied both to the data in the table of fig. 1.6 and to those plotted in fig. 1.8, which compares the experimental data with the saturation model predictions. As we will see in the chapter dedicated to the detector, a prior estimation of the expected particle multiplicity has been fundamental in its technical design, most of all to define the requirements in terms of granularity. Although the estimations are still affected by a large uncertainty, the ALICE detectors should assure very good performances in terms of granularity since it has been designed to manage the maximum predicted pseudorapidity density $dN_{ch}/d\eta = 8000$, at least at central pseudorapidity.

1.4.2 Collective flow

Another collective observable that can provide information about the evolution of the matter in the heavy-ion collision is the flow. The flow can be defined as a collective expansion of the matter and can follow different possible patterns, evolving both

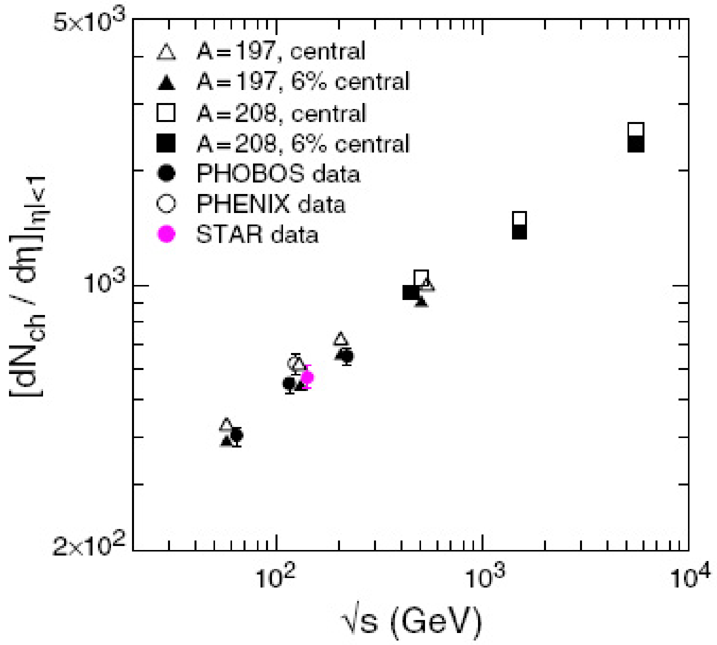

Figure 1.8: The charged particle multiplicity per pseudo-rapidity at $\eta = 0$ as a function of centre-of-mass energy per nucleon pair. Experimental data (*circles*) and predictions of the saturation model are compared. Note that experimental points measured at the same energy have been slightly displaced for visibility.

with an isotropic expansion and with a non-isotropic component, like in non-central collisions. In particular, this phenomenon affects all the particles involved in an event, showing the presence of multiple interaction between them. In proton-proton collisions this effect is absent, while it was observed in every nucleus-nucleus collision class, from the low energy fixed-target reactions below 100 A MeV up to the RHIC collision at $\sqrt{s_{NN}} = 200$ GeV; it is as well expected to be observed by ALICE.

Different medium effects can influence the flow, depending on the energy of the collision: at low energies, flow effects are mostly caused by the nucleons belonging to the incoming ions and can be interpreted as caused by two-body interactions and mean field effects. At high energy, the larger number of produced particles dominates the flow effects while the initial nucleons are supposed to give a minor contribute, especially at central rapidities. Measuring the flow, it is thus possible to distinguish if it originates from partonic matter or from the hadronization stage.

In fig. 1.9 the three most common flow phenomena are schematically represented. The *radial flow* interests central collisions: here the initial state is symmetric in azimuth, causing an isotropic azimuthal distribution even of the particles in the final stage (see fig. 1.9a). The relevant observables to study such effects are the transverse momentum distributions of the various particle species.

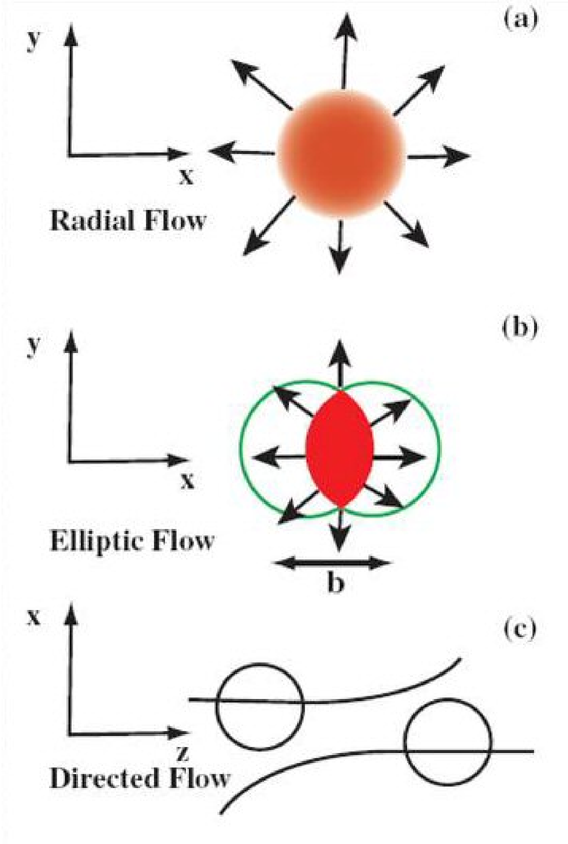

Figure 1.9: Illustration of the three most common flow phenomena.

Instead, in non-central collisions the pressure gradients are in general azimuthally asymmetric. These pressure gradients cause a correlation between the event configuration and the momentum distributions. For this *anisotropic flow*, the pattern depends on the collision energy, the considered phase-space region and the particle species. The flow of the nucleons from the nuclei have its maximum in the plane determined by the impact parameter and the beam axis, i.e. the reaction plane. Moreover, the flows of particles originating from the two nuclei are equal in magnitude but opposite in direction, thus it is called *directed flow* (see fig. 1.9c). At ultra-relativistic energies the particles are mostly produced within the interaction volume and can exhibit additional flow patterns; this results in the so-called *elliptic flow* (see fig. 1.9b). Several different methods has been proposed to measure the anisotropic flow, based for example on the event-by-event reconstruction of the reaction plane, performed by correlating the directions of the produced particles with the event plane, or on the study of the two-particle correlations without reconstructing the reaction plane.

1.4.3 Particle production

The partonic matter created in the heavy-ions interactions at ultrarelativistic energies hadronizes into a large number of hadronic species. Through the study of the yields, the momentum spectra and the correlations of the produced particles, it's possible to extract information on the initial state matter phase and on the hadronization process, in order to understand the evolution of the system.

As described by the Bjorken picture, a large fraction of particles will originate after the QGP phase, during the hadronization. The *chemical freeze-out* stage of the event, where the inelastic interactions stop, will govern the composition of the emitted hadrons; the elastic interactions will be still possible until the kinetic freeze-out is reached: thus, the measurements of the momentum spectra of the different particle types will allow a reconstruction of the event since the hard initial collisions until the soft final interactions. The different behaviour of chemical and kinetic freeze-out conditions in the $T - \mu_B$ plane is shown in fig. 1.10. The proposed empirical unified description shows that the hadronic composition of the final state is determined by an average energy per hadron being approximately 1 GeV in the rest frame of the produced system [18].

Strangeness enhancement

In order to observe the variations in the production of strange particles in presence of the QGP, it is useful to define the strangeness content as the ratio

$$\lambda_s \equiv 2\frac{\langle s\bar{s}\rangle}{\langle u\bar{u}\rangle + \langle d\bar{d}\rangle}, \tag{1.2}$$

where the quantities in brackets represent the number of quark-antiquark pairs [19].

The particle yields are studied with the aim to reconstruct the strange-to-light-quarks λ_s ratio at the hadronization point before the decays, even if it is difficult since the u, d quark number increases significantly in the secondary decays. Other yield studies can regard certain chosen particle ratios, like K/π, for different systems at different energies.

The production of strange particles is suppressed in the ordinary nuclear matter by the larger s quark mass with respect to the u and d masses. The absence of

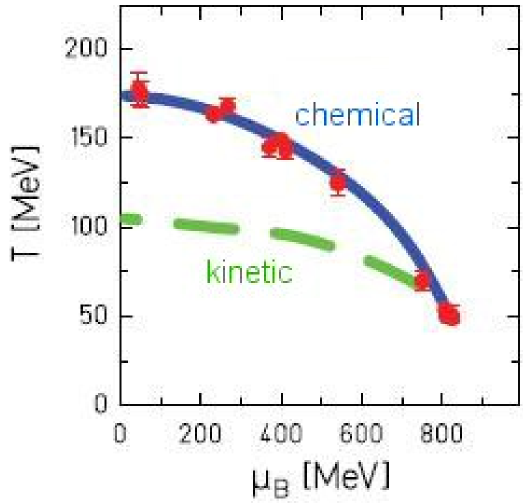

Figure 1.10: The chemical freeze-out condition (*solid blue line*) compared with the temperatures where kinetic freeze-out (*dashed green line*) is observed [18]. The chemical freeze-out line is a phenomenological behaviour extrapolated from the parameters observed at SIS, AGS, SPS (40 $A \cdot GeV$ and 160 $A \cdot GeV$) and RHIC. The resulting final state is composed of hadrons with 1 GeV average energy per hadron in the rest frame of the produced system.

strange valence quarks in the colliding nucleons causes a suppression of the strange baryons production in the low-energy nucleon-nucleon collisions. Instead, the yields for strange-particle species in ultrarelativistic nucleus-nucleus collisions should be higher than the corresponding yields at the same energy in nucleon-nucleon collisions, if the deconfinement occurs: here the reactions leading to strangeness production are partonic and have lower thresholds and higher cross sections, in particular if the strange mass is reduced by the partial restoration of the chiral symmetry; as explained before (section 1.1), in these conditions the quarks should retain only their *bare* mass, decreasing from ∼500 MeV to ∼150 MeV, and the threshold for the $s\bar{s}$ pairs should be consequently lowered allowing their production via gluon-gluon fusion in the QGP conditions. Moreover, in a system rich of baryons with respect to the antibaryons with high concentration of up and down quarks, the Pauli principle could block the production of $u\bar{u}$ and $d\bar{d}$ pairs: the energy of the lowest free level available for a light quark should grow enough to be comparable with the energy needed to create an $s\bar{s}$ pair.

The resulting enhancement in the strange particle production has been observed by the NA57 and WA97 experiments: the results are visible in fig. 1.11, grouped for different species of hyperons and normalized to the yields measured in the p-Be interactions. No enhancements are seen for p-Pb, while for Pb-Pb the enhancement exists and increases with the centrality of the collision. Moreover, the enhancements are systematically larger according to the strangeness content of the particle: for the Ωs, the enhancement reaches the value of 20 for the most central collisions [20]. At

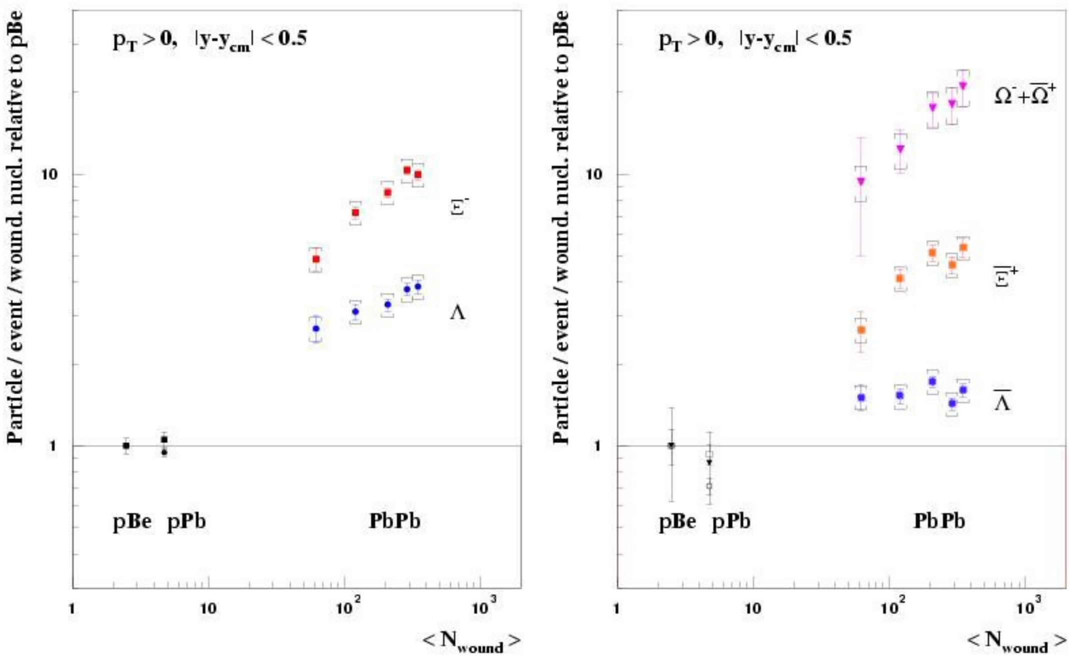

Figure 1.11: The strangeness enhancement as observed at SPS. The yields of the different hyperons in p-Be, p-Pb and Pb-Pb collisions, normalized to the p-Be production are plotted as a function of the number of participants.

LHC, the expected enhancement should follow the same behaviour observed at SPS and RHIC, but some non-equilibrium models predict even greater enhancements.

Anyway, ALICE will be capable to measure this factor in order to understand the strangeness production mechanisms in different systems at the same energy.

1.4.4 Electromagnetic probes: photons and dileptons

The importance of the observation of collision products that undergo only electromagnetic and weak interactions has been stressed in the introduction of this overview of the QGP observables: probes with such characteristics can provide information about the different stages of the event evolution without being influenced by the traversed matter. In this section the study of the electromagnetic probes, namely photons and dileptons, is discussed.

Photons

The photons are produced in all the different stages of a heavy-ion collision and, owing to their small electromagnetic coupling, they do not interact with the surrounding matter [21, 22]. In particular the different production stages can be summarized qualitatively as follows:

1. The 'prompt' photons are produced early in the pre-equilibrium stage of the collision, by parton-parton scattering in the primary nucleus-nucleus (or nucleon-nucleon) collisions. In the high p_t domain ($p_t > 10$ GeV/c), the photons are produced in QCD hard-scattering processes. Although their rate decreases as an inverse power of p_t, photons up to several hundred GeV are expected to be detected at LHC: their yield should be suppressed by the nuclear shadowing and the in-medium parton energy loss, but should be increased thanks to the partonic transverse momentum and to the photon radiation induced by the medium. The production nuclear effects and the medium effects have to be disentangled comparing the Pb-Pb observations with the p-p and the p-Pb ones. The data from Tevatron experiments on p-p events and from RHIC appears to be well described by perturbative QCD. It has to be stressed that an important background to direct photon production is the decay $\pi^0 \to \gamma\gamma$, produced in similar hard partonic processes.

2. In the equilibrium stage of the collision, the quark gluon plasma is expected to be formed with a temperature of up to 1 GeV. In the thermal bath, photons are radiated off the quarks which collide with other quarks and gluons. This production adds to the *prompt* photons in the low p_t domain ($p_t < 10$ GeV/c).

3. After the QGP phase, the plasma expands and cools. At the critical temperature a hadronic phase is formed. In this phase, photons can be produced in the scattering of π, ρ, ω or in resonance decays. This mechanism continues until the resonances stop to interact, when the freeze-out temperature of ~100 MeV is reached. The theoretical predictions of the direct thermal photon spectra are based on two step calculations: the photon production rates from an equilibrated QGP and hadron gas are calculated and then convoluted with a model for the space-time evolution of the fireball.

4. After freeze-out, further photons can be produced by the decay of π, η and

higher resonances, with energies in the range of up to a few hundred MeV.

Photons produced by π decays, either from the primary collisions or final-state contribution, constitute a large but reducible background to direct photon production over the whole p_t range. Thus they can be subtracted from the data. Instead, the prompt photons provide an irreducible background but its estimate is necessary to extract the rate of thermal photons.

Dileptons

Another important tool for probing the temperature and the dynamical properties of the matter during the evolution of a relativistic heavy-ion collision is the production of lepton pairs, the so-called *dileptons*. Even for the dilepton production, as for the photons, it's possible to distinguish among prompt, thermal and freeze-out decay components:

- considering the dilepton mass range, above pair mass M $\sim$ 2 GeV the prompt contribution is dominated by semi-leptonic decays of heavy-flavour mesons and by the Drell-Yan process ($q\bar{q} \rightarrow l^{+}l^{-}$). Since these leptons originate from hard scatterings, their rates can be calculated in perturbative QCD;

- at lepton pair masses above $\sim$ 1.5 GeV , since the thermal radiation is very sensitive to temperature variations, it is expected to originate from the early hot phases, probably from qq annihilation. Similarly to the photon case, the thermal QGP radiation has to be discriminated of from the large prompt background;

- finally, at low masses, less than 1.5 GeV, thermal dilepton spectra are dominated by the radiation process from the hot hadronic phase.

1.4.5 Heavy-quark and quarkonium production

Among the *hard probes* that could provide direct information on the deconfined medium produced in the heavy-ion events, charm and bottom quarks are very suitable to understand the dynamics of the collisions: their production takes place on a timescale of the order of $1/m_Q$ where m_Q is the heavy-quark mass. On the other hand, thanks to their long lifetime, charm and bottom quarks can live through the thermalization phase and be affected by its presence.

In order to extract information about the plasma from the features of heavy-quark production in A-A collisions it's very important to well understand their production in p-p and p-A interactions and compare some observables like the total production rates, the transverse momentum distributions and the kinematic correlations between the heavy quark and antiquark.

Both the productions of bound states of $c\bar{c}$ and $b\bar{b}$ (*quarkonia*) and of open charm and bottom will be extensively studied by ALICE, either as different probes of the event evolution and as interrelated topics. The study of the correlations between the properties of open charm and bottom and quarkonia spectra will allow to understand the dynamics of the dense medium: in the very low p_t region, which will be accessible to ALICE, the production of heavy quark-antiquarks pairs should increase the probability of forming quarkonia. In the region of perturbative production, i.e. at large p_t, the quarkonium suppression should take place.

Moreover, the different effects of enhancement in the productions of quark-antiquark pairs and of the quarkonium suppression, which will be introduced in the following paragraphs, should be disentagled by the study of the correlations between quarkonium and open heavy-quark momentum spectra.

Open charm and beauty observation

The measurement of open charm and open beauty production allows one to investigate the mechanisms of heavy-quark production, propagation and, at low momenta, hadronisation in the hot and dense medium formed in high-energy nucleus-nucleus collisions. The open charm and open beauty cross sections are also needed as a reference to measure the effect of the transition to a deconfined phase on the production of quarkonia: a direct measurement of the D and B mesons yields would provide the normalization for charmonia and bottomonia production.

Finally, the measurement of B meson production is necessary within the search for the quarkonia suppression, which will be further discussed, in order to estimate the contribution of secondary J/Ψ (from $B \rightarrow J/\Psi + X$) to the total J/Ψ yield: B mesons decay into J/Ψ mesons with a branching ratio of about 1%. Since B mesons are produced by a factor of 5 more abundantly than J/Ψ mesons, and since direct J/Ψ production might be further suppressed by QGP effects, secondary J/Ψ mesons are conceivably contributing a large fraction to the observable J/Ψ signal.

The measurement of charm and beauty production in proton-proton and proton-nucleus collisions, besides providing the necessary baseline for the study of medium effects in nucleus-nucleus collisions, is intrinsically interesting as a test of both perturbative and non-perturbative sectors of QCD in a new energy domain.

Quarkonia observation

At the QGP phase high temperature, the quark-antiquark pairs can be produced and form quarkonium states: these states are bound by energies comparable with the mean energies of the plasma ($\sim$ few hundred MeV) and therefore have large probability to break up.

The dissociation of heavy-quark bound states can be explained with this picture, for example for the J/Ψ case: it is the $1S$ bound state of a $c\bar{c}$ pair; in the hot medium of deconfined quarks and gluons, the colour screening will dissolve the binding and separate the c and the $\bar{c}$. When the medium cools down to the confinement transition point, the separated quarks will be too far to see each other and to interact: the charm quark (antiquark) will thus combine with a light antiquark (quark) and form a D ($\bar{D}$). Therefore the J/Ψ production will be suppressed by the presence of the QGP.

The NA38 and NA50 experiments at SPS have extensively studied the production of the charmonia (J/Ψ and Ψ'). The data refer to different systems, from O-U and S-U (NA38), with a projectile energy of 200 GeV per nucleon, to Pb-Pb (NA50) with a projectile energy of 158 GeV per nucleon [23]. Also p-p and p-nucleus interactions (with proton energy as high as 450 GeV) have been studied in detail as a benchmark to understand the nuclei-nuclei interactions.

The data collected with proton, Oxygen and Sulphur beams on several targets show that the J/Ψ yield is suppressed with respect to the Drell-Yan process ($q\bar{q} \rightarrow l^+l^-$) yield. Namely, the J/$\Psi$ to Drell-Yan ratio shows a suppression that increases with the mean length of nuclear matter crossed by the $c\bar{c}$ pair. This suppression is interpreted in terms of nuclear absorption of the cc pair prior to J/Ψ formation.

The extrapolation to the Pb-Pb system of the normal suppression pattern observed with lighter systems represents the baseline to which the Pb-Pb data can be compared and is indicated by the solid curve in fig. 1.12 as a function of the transverse energy E_T. Conversely, the measured yield in Pb-Pb collision show a stronger suppression, growing more rapidly than expected with the E_T. This larger suppression is explained as an effect of the deconfined matter and the consequent colour

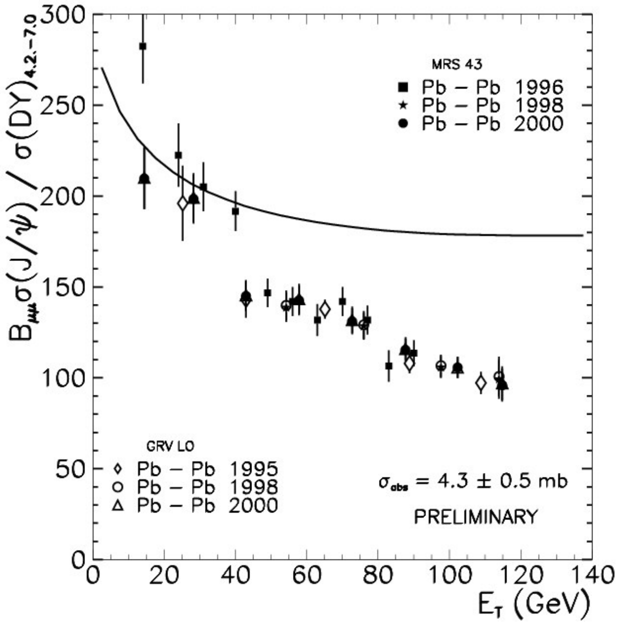

Figure 1.12: The J/Ψ suppression observed in A-A collision (*points*), compared with the suppression extrapolated from p-p collisions data (*black curve*) [23].

screening.

In addition, other effects have to be taken into account where higher centre-of-mass energies are available (RHIC and LHC): the study of charmonia show significant differences with respect to the SPS energies. Here, in addition to prompt charmonia produced directly via hard scattering, secondary charmonia can be produced according to different mechanisms which might result in an enhancement instead of a suppression of charmonium states.

Recent data taken by the PHENIX experiment at RHIC exhibit a factor three suppression for most central Au-Au collisions at $\sqrt{s} = 200$ GeV at RHIC [24]. The comparison with theoretical models suggests that it's necessary to consider the existence of recombination models in order not to overestimate the suppression in the extrapolation from the SPS experiments. At present the statistics of the present Au-Au data sample is too low to confirm those models. This problem is expected to be solved by the LHC statistics. Moreover, at LHC, the much higher energy offers the possibility of measuring with significant statistics the bottomonium yields providing another probe for QGP studies. In fact, the spectroscopy of the Υ, whose dissolution energy can not be reached at RHIC, should reveal at LHC energies new information on the characteristics of the QGP.

1.4.6 Jet quenching

In hadronic collisions, hard parton scatterings occurring in the initial interaction produce cascades of consecutive emissions of partons, called *jets*. At the end of the event evolution previously described, the jets fragment in hadrons during the hadronization phase. The final state is characterized by clusters of particles close in the phase space: their transverse momenta relative to the jet axis is small compared to the jet momenta and this collimation increases with increasing jet energy. The jets lose their energy while propagating in the hot and dense medium due to the gluon radiation, resulting in the suppression of hard jets (the so-called *jet quenching* effect); the parton energy loss grows quadratically with the in-medium path length.

High-energy nucleus-nucleus collisions allow to study the properties of this medium through modifications of the jet-structure:

- Suppressed particle yield: the in-medium energy loss results in a suppression of the hard jets and in a reduction of the high-p_t particle yield.
- Back-to-back azimuthal suppression: the interaction of the hard jets with the deconfined medium leads also to a suppression in the production of jet pairs. Studies of the angular correlation of high-p_t particles shows a peak ad opposite azimuthal angles. Instead in a deconfined matter, one of the two fast partons,

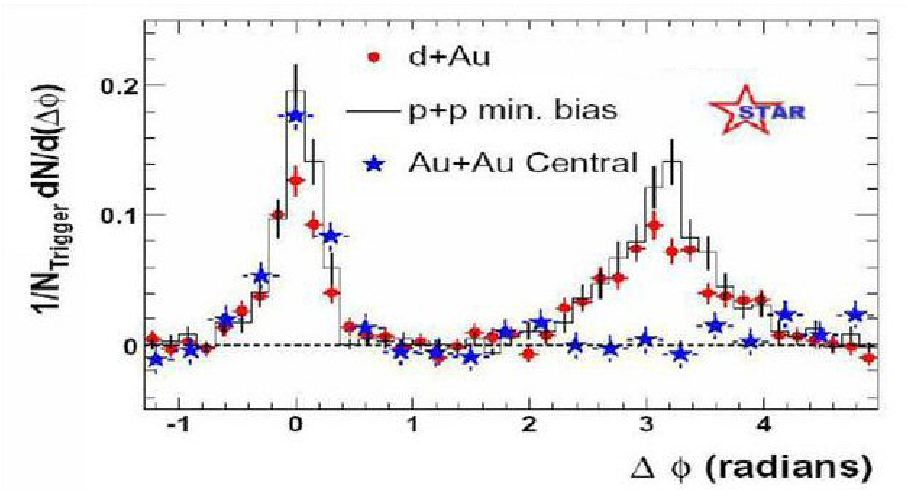

Figure 1.13: Two-particle azimuthal distribution for pp collisions (black line), central d-Au (filled points) and central Au-Au collisions (stars) observed at RHIC. The away-side jet disappears for central AA collisions [25].

covering a shorter distance to escape the medium, can emerge and be detected;

the other one goes through a longer path with respect to its partner, loses its energy interacting with the medium and is not detected. In fig. 1.13 this effect as observed by the STAR experiment at RHIC is shown.

- Impact parameter dependence: since the characteristics and the size of the dense medium should depend on the centrality of the initial collision, a correlation of the *jet quenching* effect with the impact parameter is expected to be observed.

All these discussed physics topics will be extensively studied by ALICE through a very composite detector that will be described in the next chapter.

Chapter 2

The ALICE experiment

ALICE (A Large Ion Collider Experiment) is a general-purpose experiment aimed at the study of the physics of strongly interacting matter at extreme energy densities at the CERN LHC. Through its composite detector, ALICE is designed to observe Pb-Pb collisions at the ultra-relativistic energy $\sqrt{s_{NN}} = 5.5$ TeV, measuring and identifying hadrons, electrons, muons and photons produced in the heavy-nuclei collisions. The ALICE physics program includes dedicated runs at the maximum LHC energy in order to collect reference data and to develop a specific p-p program. In addition it will take data with proton beams with proton and lighter ions, also at lower energy.

In this section the experimental conditions at LHC and the ALICE running program are briefly described. Then an overview of the ALICE detector is given: the design and technology features of the various components is considered in relation to their tasks and performances. A particular attention is devoted to the Inner Tracking System and to its role within the experiment, since a part of it, the Silicon Strip Detector, is the main subject of this thesis.

2.1 The experimental conditions at LHC

The ALICE detector was designed taking into account the expected LHC features. On the other side, the LHC programme has been planned in order to satisfy the competing physics requirements of the different LHC experiments. The planned ALICE physics programme, anyway still liable for mofications, is summarized in the next paragraph, followed by a brief discussion on the LHC luminosity and on the radiation levels concerning ALICE.

2.1.1 The ALICE physics programme

A comprehensive heavy-ion programme at the LHC is aimed at two main objectives: colliding the largest available nuclei at the highest possible energy and a systematic study of different collision systems (p-p, p-A, A-A) at different beam energies.

The LHC is expected to start with several months of pp running followed at the end of each year by several weeks of heavy-ion collisions. For rate estimates, all LHC experiments use an effective time per year of $10^7 s$ for pp and $10^6 s$ for heavy-ion operation. The initial ALICE programme is summarized below:

- Regular pp runs at $\sqrt{s_{NN}} = 14$TeV.
- Initial heavy-ion programme:
    - Pb-Pb physics pilot run;
    - 1-2 years Pb-Pb;
    - 1 year pPb-like collisions (pPb, dPb or αPb);
    - 1-2 years Ar-Ar.

The operation characteristics for a ten-year period are resumed in table 2.1.

	pp	Ar-Ar	Ar-Ar	Pb-Pb	dPb
$\langle\mathcal{L}\rangle$ (cm^{-2} s^{-1})	3×10^{30}	3×10^{27}	10^{29}	10^{27}	8×10^{28}
σ_{inel} (mb)	70	3000	3000	8000	2600
Rate (s^{-1})	2×10^{5}	9×10^{3}	3×10^{3}	8×10^{3}	2×10^{5}
Runtime (s)	10^{8}	1.0×10^{6}	2.0×10^{6}	5×10^{6}	2×10^{6}
Events	2×10^{13}	9×10^{9}	6×10^{11}	4×10^{10}	4×10^{11}
Particles per event	100	2400	2400	14200	500
N_{tot}	2.1×10^{15}	2.2×10^{13}	1.4×10^{15}	5.7×10^{14}	2×10^{14}

Table 2.1: Experimental conditions for a ten-year period in different collision type periods.

2.1.2 Luminosity in Pb-Pb collisions.

One of the most important experimental issues in the design of the experiment and of its physics programme is the luminosity for Pb-Pb collisions. It depends on the limitations imposed by both the detector and the accelerator. Among the sub-detectors, the most constraining limits come from the main tracking device, the Time-Projection Chamber (TPC), and the forward muon spectrometer. The TPC limits the maximum usable luminosity because of event pile-up during the 88 μs drift time. The TPC is expected to be operated even at luminosities above $10^{27} cm^{-2} s^{-1}$, given that the multiplicity in the Pb-Pb collisions will remain around 4000 per unit of pseudo-rapidity. On the other hand, the maximum acceptable illumination of the muon spectrometer trigger chambers limit the luminosity to $(2-4) \cdot 10^{28} cm^{-2} s^{-1}$.

However, the limitations of the LHC are stronger than those imposed by the sub-detectors technologies: the machine will provide the nominal luminosity of $\mathcal{L}_0 = 10^{27} cm^{-2} s^{-1}$.

2.1.3 Dose rates and neutron fluences

Another important issue taken into account while designing the ALICE detector is the radiation level [26]. Considering all the collision types, i.e. protons, light-ions and heavy-ions beams for different time periods and different luminosities, the radiation load on the various parts of the detectors must therefore be calculated for a combination of beam conditions.

The main sources of radiation in ALICE are: the particles produced in the collisions, the beam losses from the injection point of LHC and the beam-gas interactions in p-p runs. The dominant contribution comes anyway from particles produced at the interaction point. The ten-year integrated values for the doses and the neutron fluences in the various sub-detectors and in the electronic racks are listed in table 2.2. The radiation load reaches its maximum (2kGy dose, 1×10^{12} neutrons cm^{-2}) close to the beam pipe, in the Silicon Pixel Detector region, and scales with $\sim 1/r^2$.

2.2 The ALICE detector layout

The ALICE detector, shown in figure 2.1, consists of a central detector system, covering mid-rapidity ($|\eta| < 0.9$) over the full azimuth, and several forward sub-detectors.

System	Radius (cm)	Dose (Gy)	Neutron fluence (cm^{-2})
SPD1	3.9	2.2×10^{3}	8.0×10^{11}
SPD2	7.6	5.1×10^{2}	5.6×10^{11}
SDD1	14	1.9×10^{2}	4.5×10^{11}
SDD2	24	1.0×10^{2}	4.2×10^{11}
SSD1	40	4.0×10^{1}	4.1×10^{11}
SSD2	45	2.6×10^{1}	4.1×10^{11}
TPC (in)	78	1.3×10^{1}	3.6×10^{11}
TPC (out)	278	2.0×10^{0}	2.4×10^{11}
TRD	320	1.6×10^{0}	1.5×10^{11}
PID	350	1.1×10^{0}	1.0×10^{11}
HMPID	490	5.0×10^{-1}	8.0×10^{10}
RackLoc1		5.6×10^{-1}	8.4×10^{7}
RackLoc2		3.8×10^{-1}	1.5×10^{6}
RackLoc3		2.2×10^{-6}	3.5×10^{3}
RackLoc4		7.8×10^{-6}	9.2×10^{3}

Table 2.2: Dose and neutron fluences in ALICE detectors and in electronics.

The central detectors are placed inside the large solenoid magnet constructed for the L3 experiment at LEP, with an internal length of 12m and a radius of 5m and a 0.5 T nominal field. The field homogeneity in the volume of the detectors has been improved with respect to the L3 situation reducing the variations below 2% of the nominal field value.

The central system includes, from the interaction vertex to the outside, six layers of high-resolution silicon detectors (Inner Tracking System), the main tracking system of the experiment (Time-Projection Chamber), a transition radiation detector for electron identification (Transition-Radiation Detector), and a particle identification array (Time-Of-Flight). The central system is complemented by a small-area array of ring-imaging Cherenkov detectors for the identification of high-momentum particles (High-Momentum Particle Identification Detector), and two electromagnetic calorimeters, one consisting of a small arm of high-density crystals (PHOton Spectrometer) for the photon and neutral mesons detection, and the other, much larger than the PHOS, made of Pb-scintillators, for measuring jet properties, and

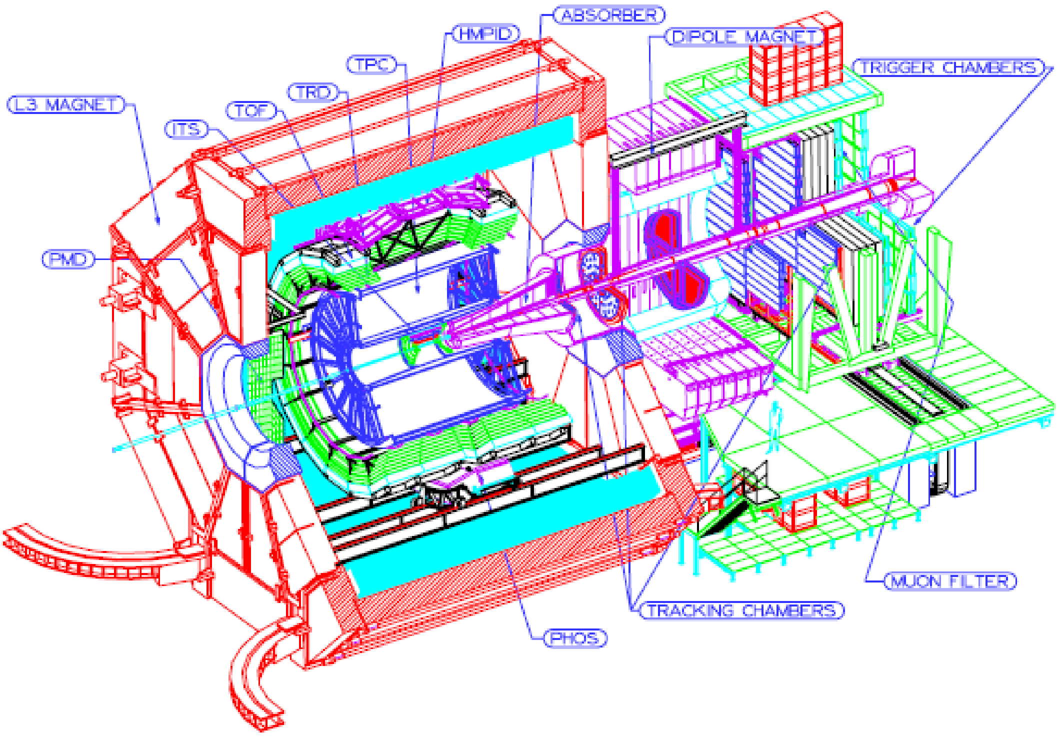

Figure 2.1: The ALICE detector layout

called EmCal.

Outside the L3 magnet, some detectors are placed for triggering (T0 and V0) or to measure global event characteristics (Photon Multiplicity Detector and Zero-Degree Calorimeter). Finally, the detection and identification of muons are performed with a dedicated Muon Spectrometer, placed outside the magnet, that exploits the beam-perpendicular field of a large warm dipole magnet. The polarity of the magnetic fields in both the solenoid and dipole magnets can be reversed within a short time.

In the following section an overview of the sub-detectors is given, with a detailed description of the design and the performances of the Inner Tracking System, which is the main subject of this thesis.

2.3 The Inner Tracking System

The Inner Tracking System is placed close to the interaction point and it was designed to accomplish some tasks which result crucial for the ALICE physics programme. These task are:

- to reconstruct the primary vertex with a resolution better than 100 μm;

- to reconstruct the secondary vertices and to measure the impact parameter for the decays of hyperons and D and B mesons;
- to track and identify the low-p_t ($< 100 MeV$) particles, which are not seen from the outer detectors;
- to improve the TPC momentum resolution for the high-p_t particles;
- to track and identify the particles traversing the dead zones of the TPC.

Moreover, in cooperation with the other detectors, the ITS characteristics allow to improve the performances in the study of many ALICE physics topics: the global observables of the heavy-ion collisions, like the charged particle multiplicity and the particle spectra and correlations; the resonance production and possible variations in their parameters; a precise mass measurement of the heavy-quark states to improve the signal-to-background ratio for the observation of the quarkonia suppression; the jet observation, covering also the TPC dead zones.

These tasks will be accomplished by the ITS thanks to its design and construction characteristics, which are described hereafter.

ITS characteristics

The Inner Tracking System (ITS) is placed very close to the interaction point. It consists of six concentric cylindrical layers of silicon detectors, the innermost of them located at a radius r = 3.9 cm, the outermost at r = 43.9 cm (fig. 2.2), and it is placed inside the Time Projection Chamber.

The number, position and segmentation of the layers are optimized for efficient track reconstruction and high impact-parameter resolution. In particular, the overall ITS dimensions are constrained by the geometry of the neighbouring parts of the ALICE apparatus: the inner radius is the minimum allowed by the beam pipe, a 800 μm-thick beryllium cylinder of 6 cm outer diameter, coaxial with the ITS detector layers; the outer radius is instead determined by the necessity to match the reconstructed tracks with those from the TPC.

The layers dimensions along the beam axis allow to cover a rapidity range of $|\eta| < 0.9$ for all vertices located within the length of the interaction diamond, i.e. $\pm 1\sigma = \pm 10.6$ cm along the beam direction. The first layer covers a more extended

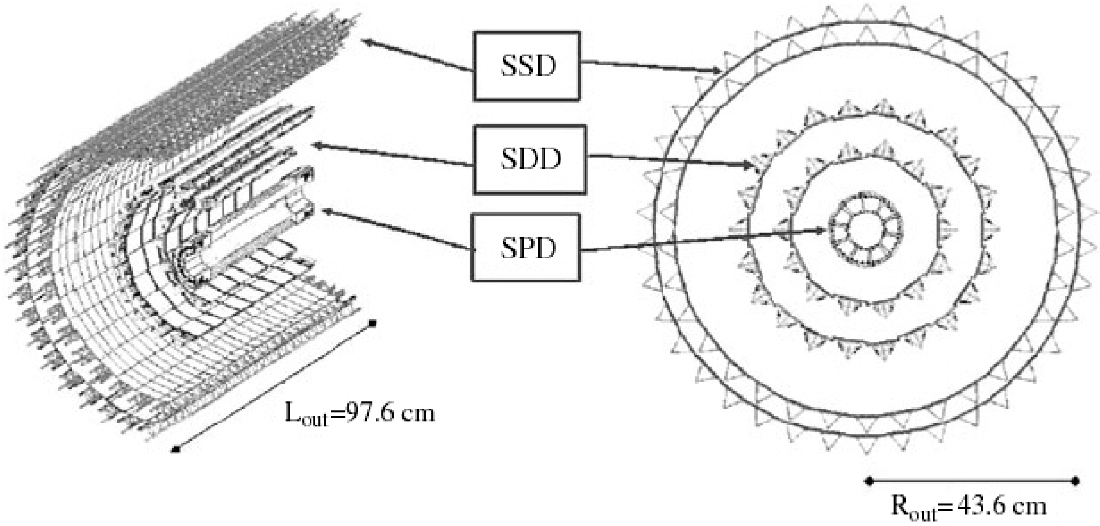

Figure 2.2: The Inner Tracking System layout.

range ($|\eta| < 1.98$) in order to provide, together with the Forward Multiplicity Detectors (FMD), a continuous coverage in rapidity for the measurement of the charged-particles multiplicity. The position and the dimensions of the ITS are listed in the table in fig. 2.3.

Layer	Type	r (cm)	$\pm z$ (cm)	Active Area (m^2)
1	Pixels	3.9	14.1	0.07
2	Pixels	7.6	14.1	0.14
3	Drifts	15.0	22.2	0.42
4	Drifts	23.9	29.7	0.89
5	Strips	37.8	43.1	2.09
6	Strips	42.8	48.9	2.68

Table 2.3: Position and dimensions of the ITS sub-detectors.

Besides the rapidity coverage, the ITS has been designed to meet the experimental requirements in terms of granularity, spatial resolution and particle discrimination. In the two innermost layers, where the particle density is expected to reach $\sim$50 particles/cm^2, highly segmented pixel detectors have been chosen: their granularity allows to detect and resolve the particles keeping the occupancy low and to reconstruct the space points with high spatial precision.

The other four layers provide also the $\mathrm{d}E/\mathrm{d}x$ information on a large dynamic range for the particle identification, allowing the ITS to operate as a stand alone low-p_t spectrometer: the central layers are equipped with silicon drift detectors, with true two-dimensional read-out like the pixels, providing high spatial precision in both directions; finally on the outermost layers, where the particle density is expected to be lower and the granularity requirements are less stringent, double-sided microstrip detectors have been placed, assuring high precision in the bending direction (∼20 μm) and minimizing the fake track probability.

Hereafter the detailed description of the three different types of silicon detectors is given, followed by a discussion of their tasks and performances.

2.3.1 The Silicon Pixel Detector (SPD)

The ALICE SPD are made of hybrid silicon pixel detectors, consisting of a two-dimensional matrix of reverse-biased silicon detector diodes bump-bonded to readout chips. On each silicon diode, a conductive solder bump is soldered to a contact on the readout chip corresponding to the input of an electronics readout cell. The readout is binary: when the signal, pre-amplified and shaped by the read-out chip, surpasses the applied threshold, the corresponding cell outputs a *logical 1*. In fig. 2.3 the layout of the SPD is shown. The characteristics in terms of geometry, active area and other operating parameters are summarized in table 2.4.

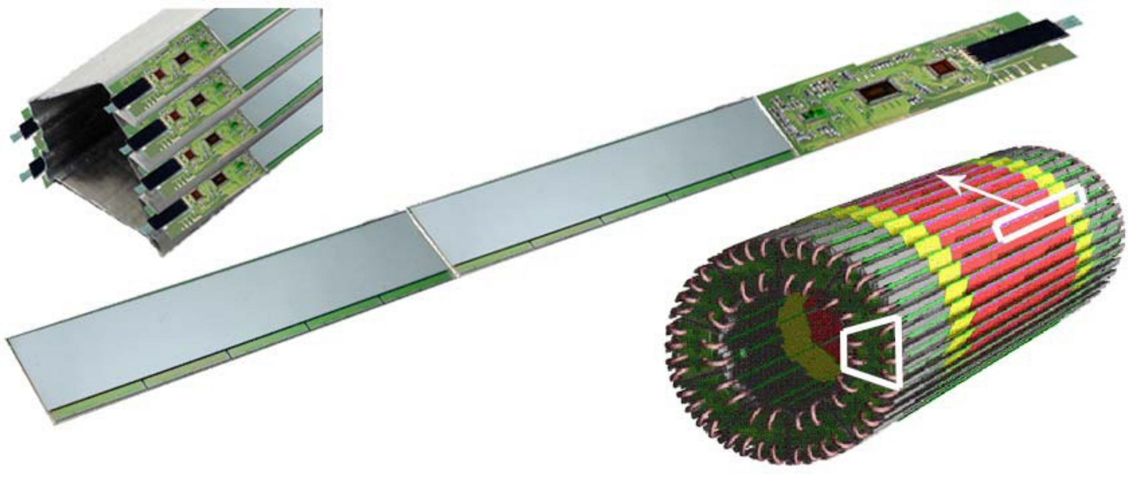

Figure 2.3: The Silicon Pixel Detector layout: the pixel barrel (*bottom right figure*), and two details.

As already mentioned, the SPD is fundamental for the primary vertex reconstruction and for the measurement of the impact parameter of secondary tracks originating from the weak decays of strange, charm and beauty particles, namely for the secondary vertices reconstruction. Besides the high performances requested in terms of granularity and spatial precision, the SPD is radiation hardened in order to operate in a relatively high radiation environment: for the 10 years running period foreseen for the experiment, in the case of the inner layer, the integrated levels of total dose and fluence are estimated to be 220 krad (2.2 kGy) and 10^{12} n$\cdot$cm^{-2} (1 MeV neutron equivalent), respectively.

In addition, its design minimizes the material budget (down to $\sim$1% of the radiation length X_0 per layer, for a straight track perpendicular to the surface) in order to reduce the Coulombian scattering of the traversing particles.

The sensor is 200 μm thick; its high segmentation allows to keep the diode capacitance low, resulting in an excellent signal-to-noise ratio at high speed. The SPD is cooled with an evaporative system based on C_4F_{10} that allows the detector to operate at an average temperature range 25^{o}C to 30^{o}C: cooling capillaries are embedded in the supports, while a high thermal conductivity grease transfers the heat from the front-end electronics.

Finally, exploiting the speed of the detector response, each pixel chip provides a *Fast-OR* digital pulse when at least one pixels in the matrix is hit. The pre-processed *Fast-OR* data can contribute to the *Level 0* trigger decision in the ALICE acquisition. This feature is very useful in particular in the case of events with very low multiplicities in p-p runs and significantly improves the background rejection in these interactions and the event selection in heavy-ions runs.

2.3.2 The Silicon Drift Detector (SDD)

The two central layers of the ITS, where the charged particle density is expected to reach up to 7 cm^{-2}, are equipped with Silicon Drift Detectors (SSD). The Silicon Drift Detectors provide the localization of the impact point of a particle in two dimension, exploiting the silicon segmentation on one coordinate and the measurement of the transport time of the deposited charge to measure the second coordinate. The high resolution and multi-track capability are provided at the expense of speed. They are therefore well suited to the ALICE experiment in which very high particle multiplicities are coupled with relatively low event rates.

A linear SDD has a series of parallel, implanted p$^+$ field strips, connected to

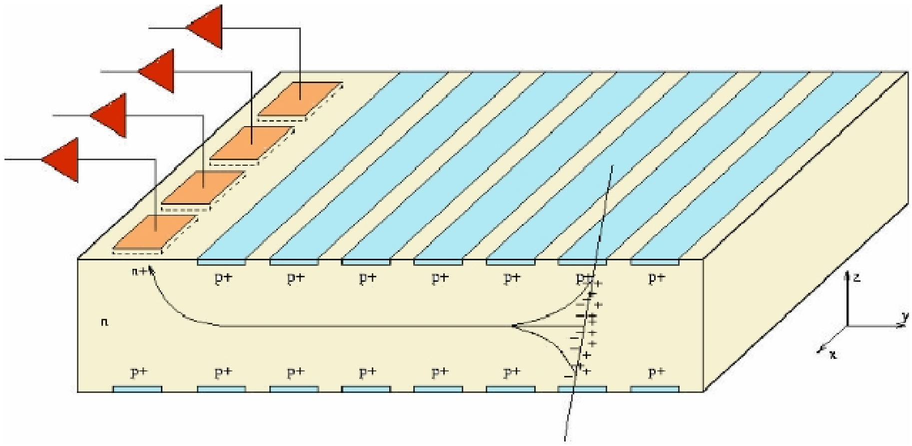

Figure 2.4: Schematic view of the charges drifting inside the SDD sensor. See the text for a brief working principle description.

a voltage divider on both surfaces of the high-resistivity n-type silicon wafer. The voltage divider is integrated on the detector substrate itself. The field strips provide the bias voltage to fully deplete the volume of the detector and they generate an electrostatic field parallel to the wafer surface, thus creating a drift region.

Electron-hole pairs are created by the charged particles crossing the detector. The holes are collected by the nearest p^+ electrode, while the electrons are focused into the middle plane of the detector and driven by the drift field towards the edge of the detector where they are collected by an array of anodes composed of n^+ pads. The small size of the anodes, and hence their small capacitance, imply low noise and good energy resolution. The flowing mechanism is shown in the scheme in fig. 2.4.

The ALICE SDD is produced from homogeneous high-resistivity (3 kΩcm) 300 μm thick Neutron Transmutation Doped (NTD) silicon.

It's layout is shown in fig. 2.5: the sensitive area is split into two drift regions by the central cathode strip, HV-biased with 2.4 kV. In each drift region the drift field parallel to the wafer surface is generated by the p^+ cathode strips that fully deplete the detector volume, a row of anodes collects the charges and three rows of MOS charge injectors monitor the drift velocity which depends on temperature. This dependence ($v_{drift} \propto T^{-2.4}$) causes a velocity variation of 0.8%/K at room temperature. Owing to the diffusion during the drift, the electrons reach the anode region with a Gaussian distribution. The coordinate perpendicular to the drift direction is given by the centroid of the collected charge. The coordinate along the drift direction is measured by the centroid of the signal in the time domain, taking into account the

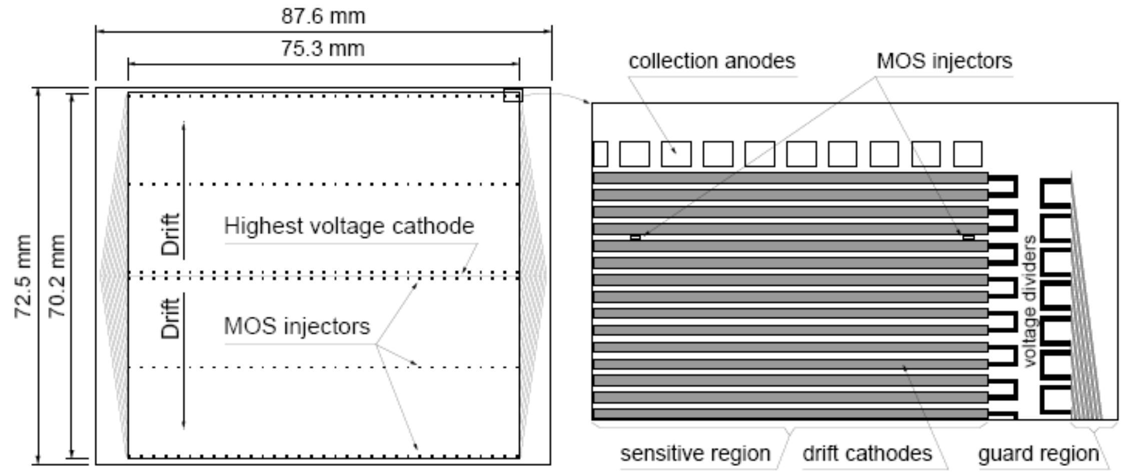

Figure 2.5: Schematic view of the ALICE SDD. The sensitive area is split into two drift regions by the central, highest voltage, cathode. On each drift region 256 anodes provide to collect the charges and three rows of 33 point-like MOS charge injectors are used to monitor the drift velocity.

amplifier response.

With these constructive characteristics, the SDD achieves a space precision as good as $35\mu m$ and $25\mu m$ along the drift direction ($r\varphi$) and along the anode (z) respectively. Moreover, the detector provides two out of the four dE/dx samples needed for the ITS particle identification.

2.3.3 The Silicon Strip Detector (SSD)

The outer layers of the ITS are composed of 1698 Silicon Strip Detector (SSD) modules: they use 300 μm thick double sided silicon sensors with 768 strips on each side; the strips, with a pitch of 95 μm, form a stereo angle of 35 mrad between the two opposite module sides, which assures a stereo view and the reduction of ambiguities, even at high particle densities. An SSD module is visible in the picture in fig. 2.6.

The SSD layers are crucial for the matching of tracks from the TPC to the ITS. They provide a two dimensional measurement of the track position and $\mathrm{d}E/\mathrm{d}x$ information to assist particle identification, in particular for low-momentum particles.

The ALICE silicon strip detector and its features will be described in detail in chapter 3, specifically devoted to its construction, assembling and validation.

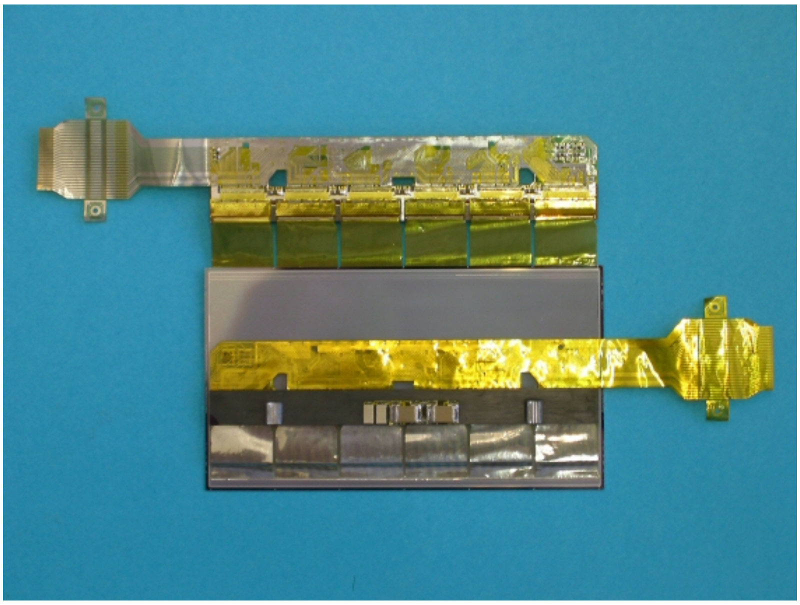

Figure 2.6: An SSD module during the construction, after the assembling of the sensor with the electronics.

2.3.4 The ITS performances

Thanks to the described constructive characteristics, the ITS is capable to satisfy the requirements imposed by the challenging ALICE physics programme [27, 28]. In this section the basic performances of the ITS, as expected from Monte Carlo simulations, are discussed in relation to the main observables that will be studied by the experiment. The most important parameters of the ITS are summarized in table 2.4.

- **Acceptance**. The rapidity acceptance of the ITS ($|\eta| < 0.9$) allows to study the global observables of the heavy-ion collisions, like the particle ratios, the p_t spectra and the particle correlations on an event-by-event basis. Within the covered rapidity range, the ITS is able to detect and track the thousands of particles emitted in each heavy-ion collision, resulting necessary in particular to detect the decay of large mass, low p_t particles. With its full azimuthal coverage, the ITS can provide also an efficient rejection of low-mass Dalitz decays.

  Moreover, the inner SPD layer, covering the range $|\eta| < 1.98$ for interactions taking place at $z = 0$, can provide a continuous coverage in rapidity for the measure of charged particles multiplicity over about 8 η-units if combined with

Parameter		Pixel	Drift	Strip
Spatial precision $r\varphi$	(μm)	12	35	20
Spatial precision z	(μm)	100	25	830
Two track resolution $r\varphi$	(μm)	100	200	300
Two track resolution z	(μm)	850	600	2400
Cell size	(mm^2)	50×425	202×294	95×40000
Active area per module	(mm^2)	12.8×69.6	72.5×75.3	73×40
Readout channels per module		40960	2×256	2×768
Total number of modules		240	260	1698
Total number of readout channels	(k)	9835	133	2608
Total number of cells	(M)	9.84	23	2.6
Max. occupancy in Pb-Pb (layer 5)	(%)	2.1	2.5	4
Max. occupancy in Pb-Pb (layer 6)	(%)	0.6	1.0	3.3
Power dissipation in barrel	(W)	1350	1060	850
Power dissipation end-cap	(W)	30	1750	1150

Table 2.4: The parameters of the various ITS sub-detectors. The mentioned *module* represents a single sensor element.

the Forward Multiplicity Detector (FMD). From simulation-based studies, it turns out that the measurement of the multiplicity and of the pseudorapidity distribution can be efficiently performed with the two SPD layers in their full acceptance regions ($|\eta| < 2$ for layer 1, $|\eta| < 1.4$ for layer 2). Two methods can be used: counting the number of clusters N_c for each layer or counting the number of *tracklets* N_t, where a tracklet is defined as the association of two clusters in the two layers connected by a straight line pointing to the primary vertex. In fig. 2.7 it is shown the reconstruction of *true* (simulated in this case) charged multiplicity, achieved with the tracklets method after the application of the acceptance correction. A study on the measurement of the charged particle multiplicity performed with the Silicon Strip Detector is the subject of chapter 5.

- **Spatial precision and granularity**. The granularity of the ITS detectors is capable to cope with the expected thousands of particles per Pb-Pb event,

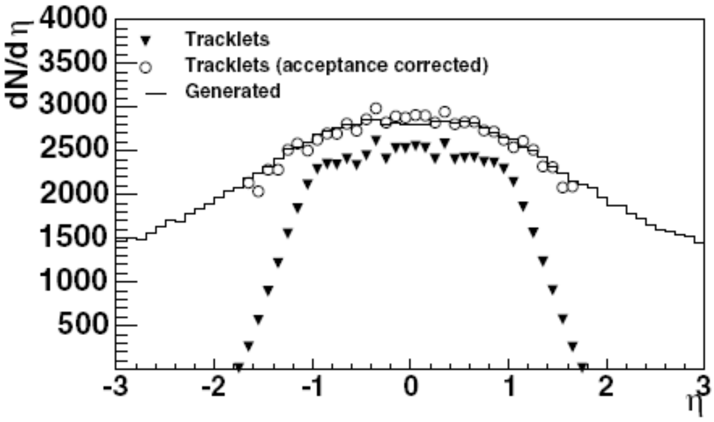

Figure 2.7: The reconstructed η distribution of charged particles compared with the simulated one, in a 400 high multiplicity event sample, generated with a random vertex longitudinal position in the range ±5 cm and a magnetic field B = 0.4 T. The multiplicity reconstructed by the SPD with the *tracklets* methods (*triangles*) and after the acceptance correction (*open circles*), is compared with the simulated distribution (*solid line*).

since it was designed for a maximum track density of 8000 tracks per unit of rapidity, while more recent extrapolations from RHIC data set to ∼ 4000 tracks the expected value for ALICE. The millions of effective cells that compose each layer of the ITS can keep the system occupancy low, at a few percent, even in events where it will detect about 10000 tracks simultaneously.

The resolution of the vertices and the impact-parameter measurement is determined by the spatial resolution of the ITS detectors, that reaches the value of $12\mu m$ for the first pixel layer: the simulations show a 10 μm resolution in the determination of the vertex z-position in case of heavy-ion collisions, and 110 μm (70 μm in the transverse coordinate) for the average pp event ($\mathrm{d}N_{ch}/\mathrm{d}\eta$ = 6-7) after the track reconstruction.

With these performances, the ITS allows to carry out for example the study of the open charm, through the observation of the D_0 weak decays, which have a proper decay length of few hundred microns ($c\tau$ = (123.0±0.4) μm). For $p_t \simeq 1$ GeV/c, the SPD layers allow a resolution of about 60μm for the impact parameter projection in the bending plane: with this resolution it is possible to reduce the combinatorial background by selecting a few displaced tracks out of the large number of primary vertex tracks.

This high resolution is fundamental also in the study of the suppression of the J/Ψ production, in particular to discriminate prompt from secondary J/Ψ

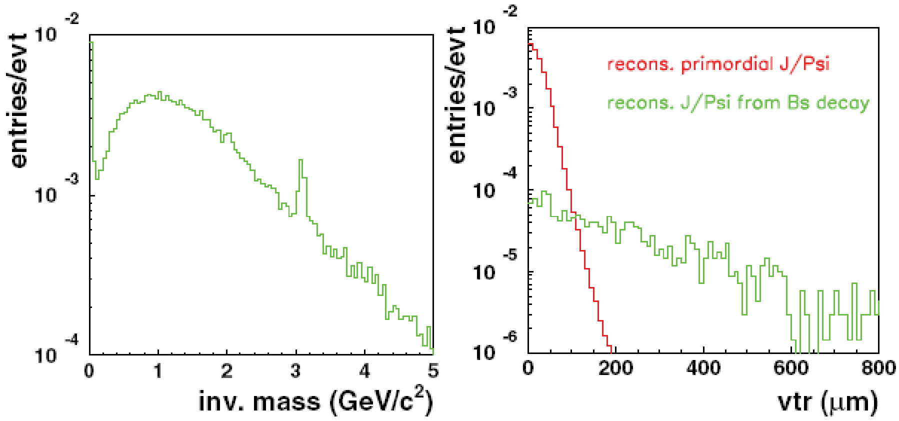

Figure 2.8: Invariant mass distribution of pairs with displaced vertices (left panel) and distance to primary vertex dependence of the J/Ψ signal (right panel).

originating from B decay. From the impact parameter measurement, indeed, it is possible to identify the e^+e^- pairs produced by a displaced vertex and to select them as secondary J/Ψ decays (see in fig. 2.8).

Moreover, the spatial precision is also crucial for the study of the strange baryon production.

- **Particle identification dE/dx measurement**. The ITS contributes to the particle identification through the measurement of specific energy loss. Four layers of the ITS (two silicon-drift and two silicon-strip detector layers) provide signal amplitude information, which can be used for PID in the low-momentum range by measuring ionization energy loss dE/dx. This is estimated as a truncated mean (using the two or three lowest amplitude signals out of four) in order to minimize the influence of Landau fluctuations. The dynamic range of the analogue readout must be large enough to provide dE/dx measurement for low-momentum, highly ionizing particles, down to the lowest momentum at which tracks can still be reconstructed with a reasonable ($> 20\%$) probability. The resulting correlation plot is shown in figure 2.9. The resolution of the ITS dE/dx measurement allows a good π/K separation up to 450 MeV/c and a good K/p separation up to about 1 GeV/c. A typical ITS response function, for momenta in the range 400-425 MeV/c, is shown in figure 2.10.

- **Material budget.** While traversing the detector material, the multiple scattering worsens the resolution of the momentum and impact parameter measurement of particles with small transverse momenta. The silicon detectors

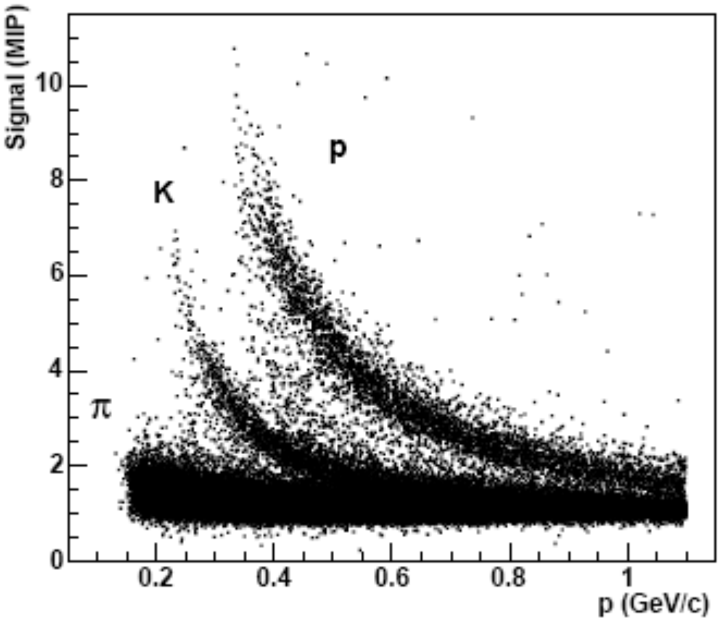

Figure 2.9: Plot of the correlation between the specific SDD/SSD signals (MIP units) calculated by the truncated mean method and the particle momentum obtained from the TPC and ITS tracking for different particle species.

have been designed and produced minimizing the total amount of material: as mentioned in the description of the various ITS sub-detectors, the pixel sensors were produced with the minimum achievable thickness of 200μm, while the drifts and the strips, which measure the ionization density dE/dx, have the minimum thickness capable to provide a good signal-to-noise ratio, namely ~300μm.

Taking into account the overlaps needed for a full coverage of the entire solid angle and the incidence angles of tracks, the detectors effective thickness amounts to 0.4% of the radiation length X_0. A comparable effective thickness is added by the electronics, cables, supports, cooling systems and other not sensible material. In table 2.5 the values for the ITS are shown. The resulting momentum resolution that can be achieved with ITS is better than 2% for pions with momentum between 100 MeV/c and 3 GeV/c.

- **Readout rate.** The ALICE detector will acquire data in two different readout configurations, triggered by different trigger classes that operate simultaneously. A first trigger activates the readout of the whole of ALICE, for the central collisions generating large events; the trigger of the muon arm acti-

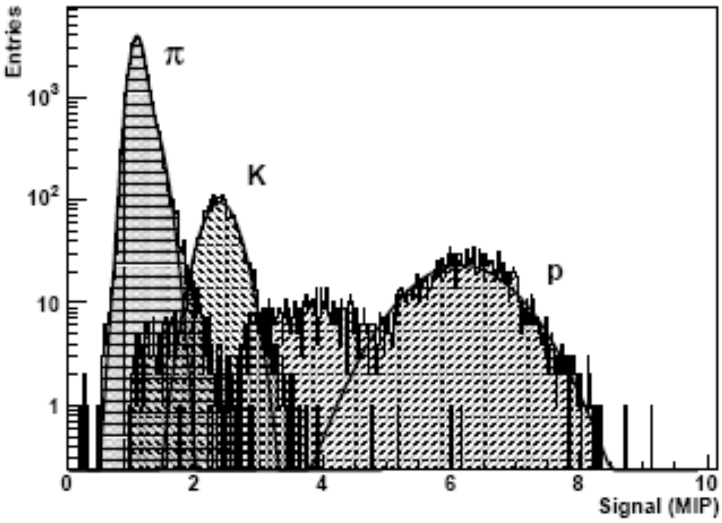

Figure 2.10: Distributions of the truncated mean SDD and SSD signals (MIP units) obtained with the HIJING generator for pions, kaons and protons for a reconstructed momentum of 400-425 MeV/c. The curves are the result of Gaussian approximations.

	Pixel		Drift		Strip	
	Inner	Outer	Inner	Outer	Inner	Outer
Detector	1.14	1.14	1.13	1.26	0.83	0.86
Thermal shield/Support		0.52	0.25		0.53	
Total	7.18 (7.26 including Air)					

Table 2.5: ITS material budget traversed by straight tracks perpendicularly to the detector surface. Units are percentages of radiation length.

vates instead the readout of a subset of fast readout detectors, including the two pixel layers of the ITS, and it is kept active even when the centrality trigger is disabled because of bandwitdth saturation. This trigger system requires the readout time for the pixel detectors to be set at less than $400\mu s$.

2.4 The Time Projection Chamber

The ALICE Time Projection Chamber (TPC) is the main tracking detector of the central barrel and is optimized to provide, together with the other central barrel detectors, charged-particle momentum measurements with good two-track separation, particle identification, and vertex determination.

It consists of a cylindrical gas volume (barrel), divided into two half volumes of equal size, separated by a 30 μm thick HV electrode to generate the drift field. Installed around the ITS, it has an inner radius of ~80 cm and an outer radius of ~280 cm, with an overall length of 500 cm in the beam direction. Multi-wire proportional chambers with pad readout are mounted at both ends of the barrel.

To minimize the multiple scattering and the secondary particle production, the material budget of the TPC field cage is kept low (3.5% X_0 at central rapidity). The TPC layout is shown in fig. 2.11. The TPC covers the pseudo-rapidity range

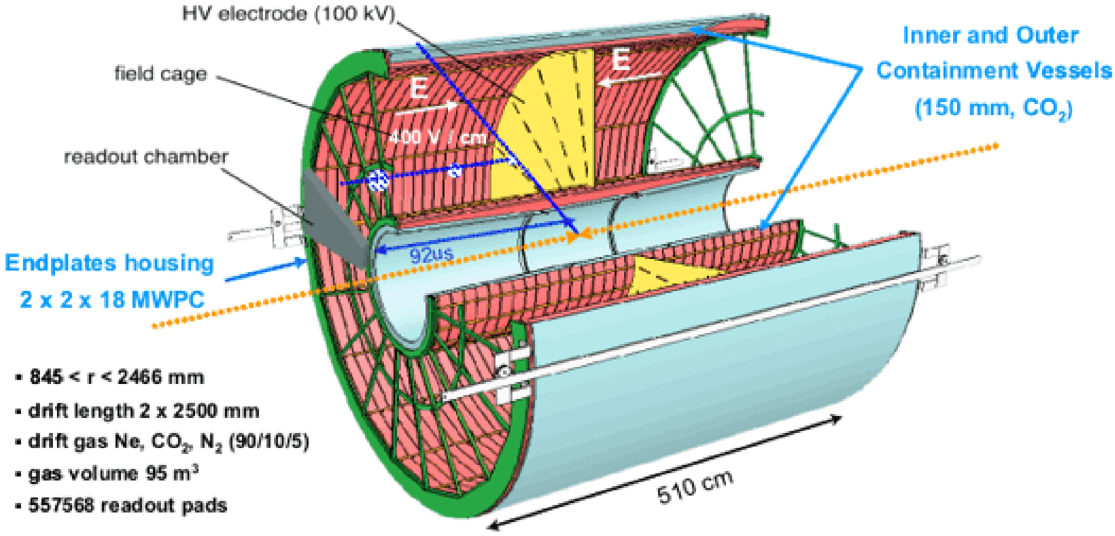

Figure 2.11: The Time Projection Chamber layout and main characteristics.

$|\eta| < 0.9$ and the full azimuth, with the exception of the dead zones in-between the readout chambers.

A high momentum resolution is required to the TPC both for the study of soft hadronic observables and for the hard probes in the high-p_t region. For low-p_t particles, between 100 MeV/c and 1 GeV/c, reconstructed in the TPC, the momentum resolution is between 1% and 2%, while it is larger than 10% at 20 GeV/c, quickly increasing with p_t. Thus it is necessary to use the TPC in combination with the other tracking detectors (ITS and TRD) to measure higher momenta: using these detectors we can achieve about 10% momentum resolution for tracks with p_t of 100 GeV/c at 0.5 T magnetic field (see fig. 2.12 for the momentum resolution comparison between different combinations of detectors).

The TPC dE/dx measurement has an estimated resolution that slightly depends on the charged-particle density: for particles with momentum around 0.5 GeV/c, it changes from 5.5% for p-p events to 6.5% for central Pb-Pb collisions.

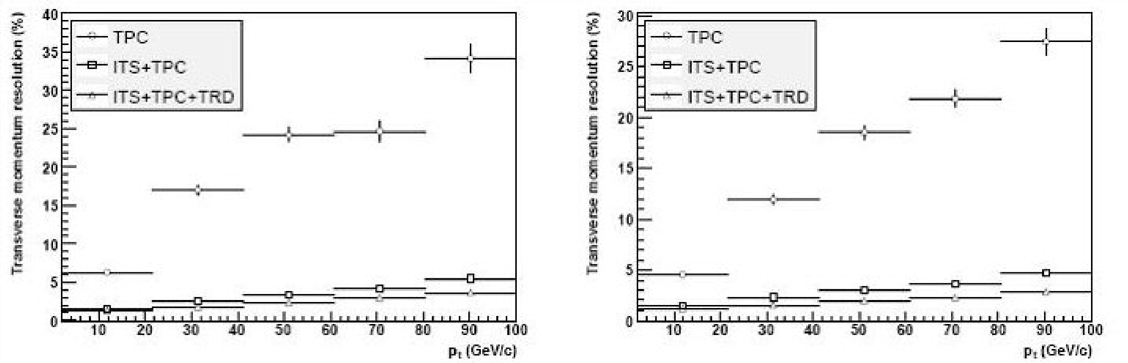

Figure 2.12: The Time Projection Chamber transverse momentum resolution in the $p_t >$ 10 GeV region compared with the resolution obtained in combination with the ITS and the TRD, for simulated central Pb-Pb collisions (*left*) and p-p collisions (*right*).

2.5 The particle identification detectors

2.5.1 The Transition Radiation Detector

The Transition Radiation Detector (TRD) has to provide electron identification in the central barrel for momenta above 1 GeV/c [29]. Above 1 GeV/c, the transition radiation from electrons traversing a radiator can be exploited together with the specific energy loss in a suitable gas mixture measured by multi-wire proportional read-out chambers. This working principle is schematically presented in fig. 2.13.

The TRD is composed of 540 individual readout detector modules: each module consists of a radiator of 4.8 cm thickness, a multi-wire proportional read-out chamber and the front-end electronics for this chamber. The signal induced on the cathode pad is read-out. In the Xe/CO_2 (85%/15%) gas-mixture of the chambers, a minimum ionizing particle liberates 275 electrons cm^{-1}. The gas gain will be of the order of 5000.

The TRD was designed to derive a fast trigger for charged particles with high momentum. It can significantly enhance the recorded Υ-yields, high-p_t J/Ψ, the high-mass part of the dilepton continuum as well as jets. The TRD achieves a pion rejection estimated in 1% of pions erroneously identified as electrons at an electron

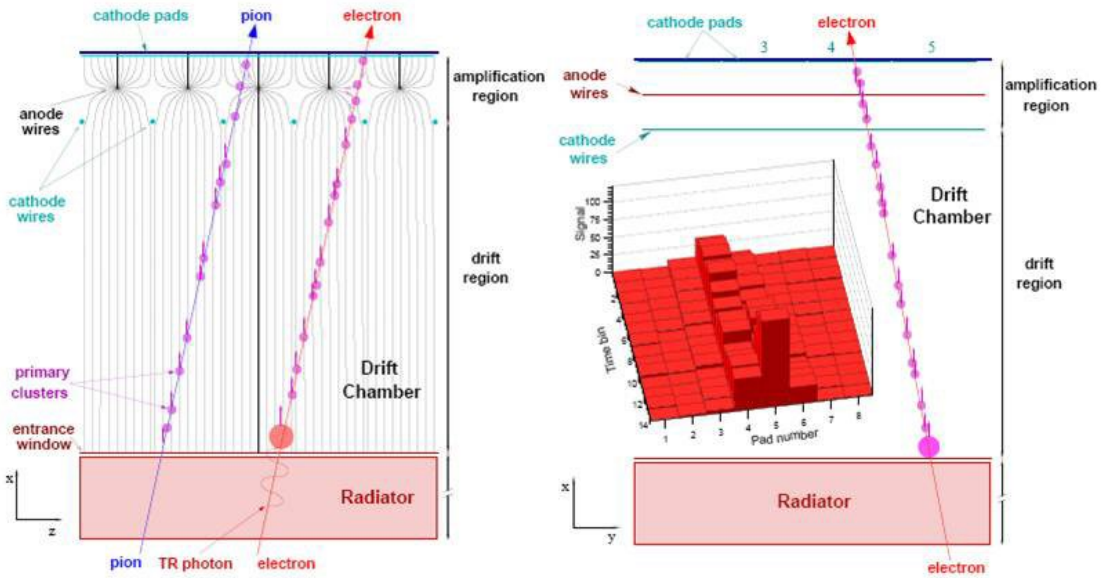

Figure 2.13: Schematic view of a detector module in $r\varphi$ direction, illustrating the TRD working principle. The left panel shows a projection in the plane perpendicular to the wires. Electrons produced by ionization energy loss (dE/dx) and by transition radiation absorption drift along the field lines towards the anode wires. The right panel shows a projection in the bending plane of the ALICE magnetic field; the inset shows the charge deposit from an inclined track, used for the momentum reconstruction.

efficiency of 90%; matching the TPC, it allows an overall mass resolution of about 100 MeV/c^2 at the Υ-mass (for B = 0.4 T).

2.5.2 The Time-Of-Flight detector

The Time-Of-Flight (TOF) detector is a large area array of Multi-Gap Resistive-Plate Chamber (MRPC) strips covering the central pseudo-rapidity region ($|\eta| < 0.9$). Its main task is the particle identification in the intermediate momentum range, below ~2.5 GeV/c for pions and kaons, up to 4 GeV/c for protons, with a π/K and K/p separation better than 3σ. The kaons identified by the TOF detector will allow invariant mass studies, in particular the detection of open heavy-flavoured states and vector-meson resonances such as the ϕ meson.

The detector has a modular structure corresponding to 18 sectors in $r\varphi$ and to 5 segments in z direction. The whole device thickness corresponds to 30% of a radiation length. The MRPC strips are placed inside modules that define and seal the gas volume, acting also as Faraday cages, and support the external front-end electronics and services. As resulting from laboratory tests on a sample of MRPC strips, these devices reach an intrinsic time resolution better than about 40 ps and an efficiency close to 100% (see the test results in fig. 2.14).

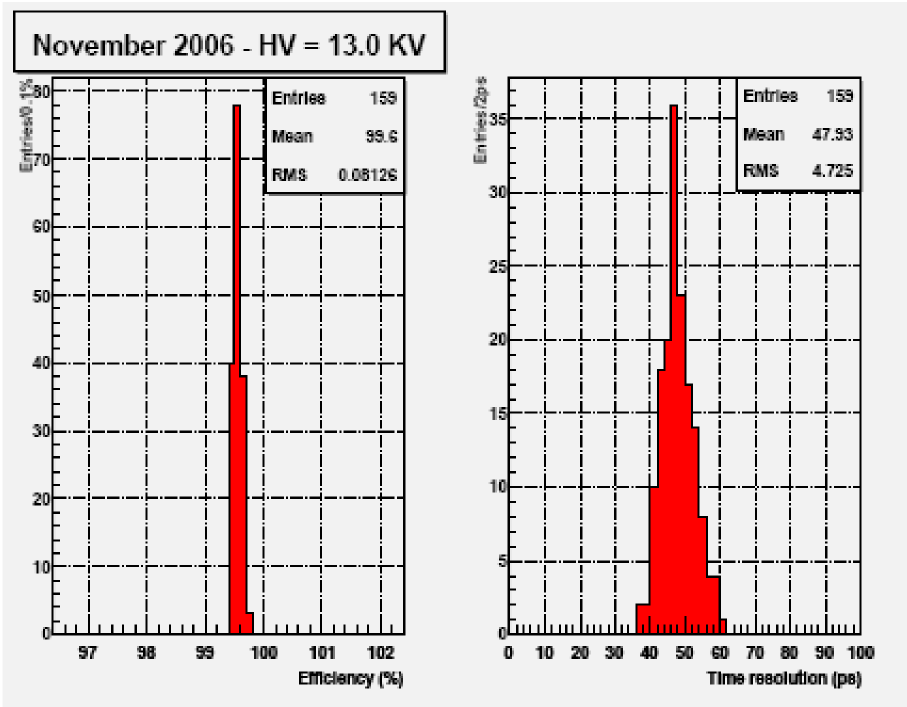

Figure 2.14: The TOF performances: efficiency (*left*) and time resolution (*right*) for a sample of TOF Multi-Gap Resistive-Plate Chamber strips measured in several positions (pads) along and across each strip, at fixed high voltage.

2.5.3 High-Momentum Particle Identification Detector

The High-Momentum Particle Identification Detector (HMPID) is dedicated to the identification of hadrons with $p_t > 1$ GeV/c. It plays an important role in the identification of particles beyond the momentum interval studied through energy loss by the ITS and the TPC and through the time-of-flight measurements by the TOF detector.

The HMPID is based on proximity-focusing Ring Imaging Cherenkov (RICH) counters: its working principle is schematically presented in fig. 2.15 . The momentum range covered is defined by the radiator used in the detector, i.e. a 15 mm thick layer of C_6F_{10} (perfluorohexane) liquid: the index of refraction of this material (n=1.2989 at λ=175 nm) corresponds to a minumum speed β_{min}=0.77, thus to the threshold momentum p_{th}=1.21 m, with p in GeV/c and the mass m in GeV/c^2.

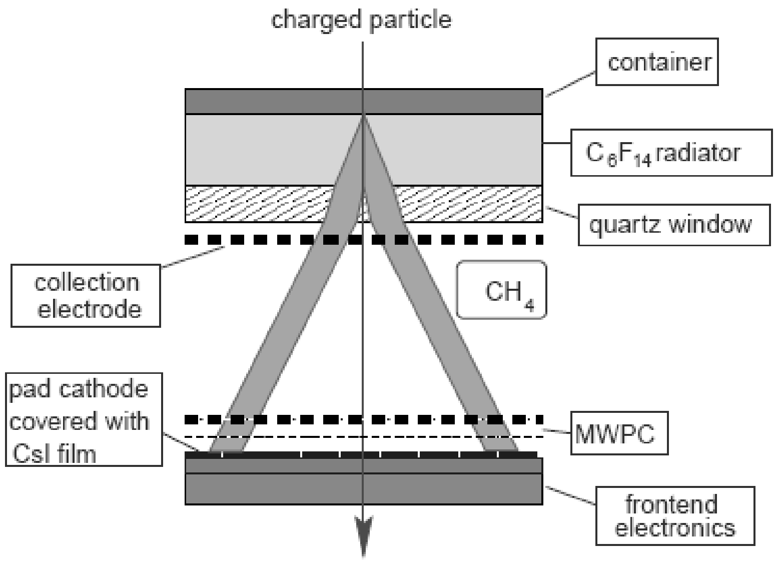

Figure 2.15: The HMPID working principle. The Cherenkov photons, emitted when a fast charged particle traverses the radiator, are detected by a photon counter, consisting of a thin layer of CsI deposited onto the pad cathode of a multi-wire proportional chamber (MWPC).

2.6 The electromagnetic calorimeters

2.6.1 The PHOton Spectrometer (PHOS)

The PHOton Spectrometer (PHOS) is a high-resolution electromagnetic spectrometer covering a limited acceptance domain at central rapidity. The PHOS is capable to measure low-p_t photons emitted in the initial phase of the collision, in order to study its thermal and dynamical properties; moreover, it is designed to measure the high-p_t π^0 and $\gamma - jet$ correlation in order to study the jet quenching effects.

The PHOS is made of almost 18000 cells, i.e. dense scintillating crystals of lead-tungstate ($PbWO_4$), like the one shown in fig. 2.16, arranged in five different modules and operated at a temperature of -25°C to increase their light yield; the modules are installed on the bottom of the ALICE apparatus, 4.6 m from the interaction point. The $PbWO_4$ has been chosen because of its characteristic small *Molière radius* and for the sufficient light output which allows to measure the lowest energies of interest with good resolution. Its high segmentation allows to keep the cell occupancy at a manageable level of about 10-20%.

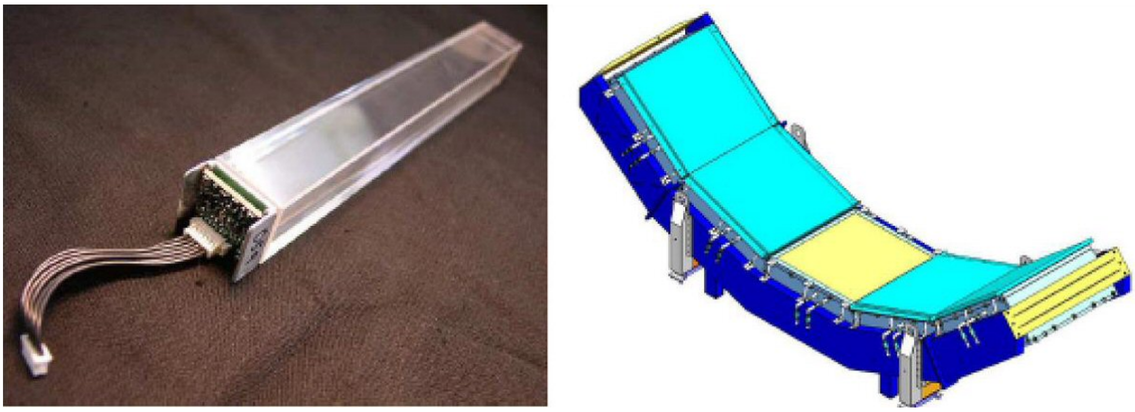

Figure 2.16: The Photon Spectrometer: the left picture shows one of the almost 18000 lead-tungstate scintillating crystal composing the PHOS; on the right, the layout of the sub-detector, with its five modules installed on the bottom of the ALICE apparatus.

2.6.2 The ElectroMagnetic Calorimeter (EMCal)

The ElectroMagnetic Calorimeter is a Pb-scintillator sampling calorimeter with longitudinal wavelength-shifting fibres, read out via avalanche photo diodes. It measures the neutral energy component of jets, enabling full jet reconstruction in all collision systems, from p-p to Pb-Pb, and provides a fast and efficient trigger for hard jets, photons and electrons.

With its cylindrical geometry, it is located adjacent to the ALICE magnet coil at 4.5 m from the beam line, approximately opposite in azimuth to the high-precision PHOS calorimeter, covering $|\eta| < 0.7$ and $\Delta\varphi = 107°$. It is larger than PHOS, but with lower granularity and energy resolution.

2.7 Muon spectrometer

The forward muon arm is designed to detect muons in the pseudo-rapidity region $-4.0 < |\eta| < -2.5$, corresponding to the the polar angular range 171°-178°. It gives the possibility to study the $\mu^+\mu^-$ decay channel of the heavy-quark vector-mesons resonances like J/Ψ, Ψ', Υ, Υ', Υ'' in the same experimental condition and with a mass resolution sufficient to separate all states.

The detector consists of a composite absorber to absorb hadrons and photons coming from the interaction vertex, a high-granularity tracking system of 10 detection planes, a large dipole magnet with a 3 T·m integral field placed outside the L3 magnet, a passive muon-filter wall, followed by four planes of trigger chambers for the identification of the muons and the triggering; both the absorbers and the detectors are designed to achieve the required invariant-mass resolution of 100 MeV/c^2 in the 10 GeV/c^2 dimuon invariant-mass region, needed to resolve the Υ, Υ', Υ'' resonances. Finally, a dense conical absorber tube provides to shield the spectrometer from secondary particles created in the beam pipe. The layout of the muon spectrometer is shown in fig. 2.17.

Figure 2.17: The Forward Muon Spectrometer layout.

2.8 Forward and trigger detectors

Finally, some small specialized detectors are used for triggering the ALICE acquisition or to measure global properties of the events:

- The T0 detector, consisting of two arrays of Cherenkov counters, measures the event time with very good precision (< 25 ps); this time is used to generate the start time for the TOF detector, to measure the vertex position (with a precision ± 1.5 cm) in each interaction and to provide a trigger when the position is within the acceptable range.

- The V0 detector, consisting of two arrays of segmented scintillator counters installed on either side of the ALICE interaction point, provides the minimum bias trigger and is used for the beam-gas background rejection.

- The Forward Multiplicity Detector (FMD), consisting in rings of silicon strip detectors located at three different positions along the beam pipe, provides charged particle multiplicity information over a large fraction of the solid angle ($-3.4 < \eta < -1.7$ and $1.7 < \eta < 5$). Partially overlapping the SPD sensors, it provides a continuous coverage for this measure, as shown in fig. 2.18.

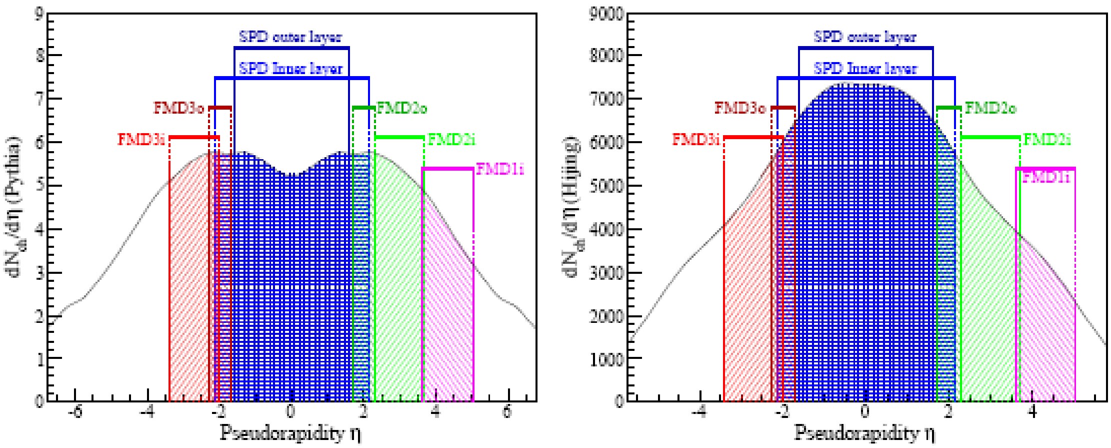

Figure 2.18: The continuous pseudorapidity coverage provided by the Forward Multiplicity Detector together with the SPD, superimposed on simulated multiplicity distributions to illustrate which regions are measured by each detector. The distributions refer to p-p events at $\sqrt{s_{NN}} = 14$ TeV in the left panel (simulated with the PYTHIA event generator) and to Pb-Pb events $\sqrt{s_{NN}} = 5.5$ TeV in the right panel (HIJING generator).

- The Photon Multiplicity Detector (PMD) measures the multiplicity and spatial distribution of photons event-by-event in the region $2.3 < \eta < 3.7$. It consists of two planes of gas proportional counters, preceded by two lead converter plates of 3 radiation lengths each.

- Two sets of two compact calorimeters each will be used to measure and trigger on the impact parameter of the collision (Zero Degree Calorimeter ZDC). They are made of tungsten (neutron calorimeters, ZN) and brass (proton calorimeters, ZP) with embedded quartz fibres, and located on both sides in the machine tunnel, about 116m from the interaction region. In addition, two small electromagnetic calorimeters (ZEM) are installed 7 m from the vertex, to improve the centrality selection.

- Finally, an array of 60 large scintillators (ACORDE) on top of the L3 magnet will trigger on cosmic rays for calibration and alignment purposes, as well as for cosmic ray physics.

Chapter 3

Construction and commissioning of the SSD

The Silicon Strip Detector (SSD) occupies the two outer layers of the ALICE Inner Tracking System. It consists of 1698 double-sided microstrip silicon devices installed in order to create two concentric cylidric sensitive surfaces covering the central rapidity region over the full azimuth. With its two-dimensional spatial resolution, excellent in the bending $r\varphi$ direction ($\sim$20μm), and the provided dE/dx information over a large dynamical range (0$\div$14 MIP), the SSD contributes to the challenging performances of the ITS and is crucial for matching with the TPC reconstructed tracks.

Its basic unit is the *module*, namely the sensor assembled with its read-out front-end electronics. The first part of this chapter is devoted to the description of the production phase of the modules, namely the $\sim$ 40% of the total amount of devices that was assembled, tested and validated in Trieste; the rest of the modules was produced with similar procedures but with identical quality validation criteria in Helsinki (Finland) and in Strasbourg (France).

The following part of the chapter concerns the assembly of the modules forming the *half-ladders* (or simply *ladders*), i.e. the minimum group of modules biased by the same power line. The characterization of the ladders, together with the classification of their defects, are described.

Finally, the installation of the entire detector in the experimental site and the subsequent integration with the other detector and the services, like the cooling system, the power supplies, the slow control and the data acquisition systems, are treated in the last part. During this *commissioning* phase, first physics data were acquired from cosmic rays and during the LHC beam tests.

This long and successful path that brought the SSD to be ready for the upcoming experimental activity, started with the production of the modules, which is described is the following section.

3.1 The SSD components

The *module* is made of a double-sided silicon microstrip sensor read-out by two hybrid circuits; in the assembled and unfolded configuration, it appears as in fig. 3.1. In this section the assembly of the different parts composing the module are described, focusing the attention on the description and the features of the single components and on the assembling operations.

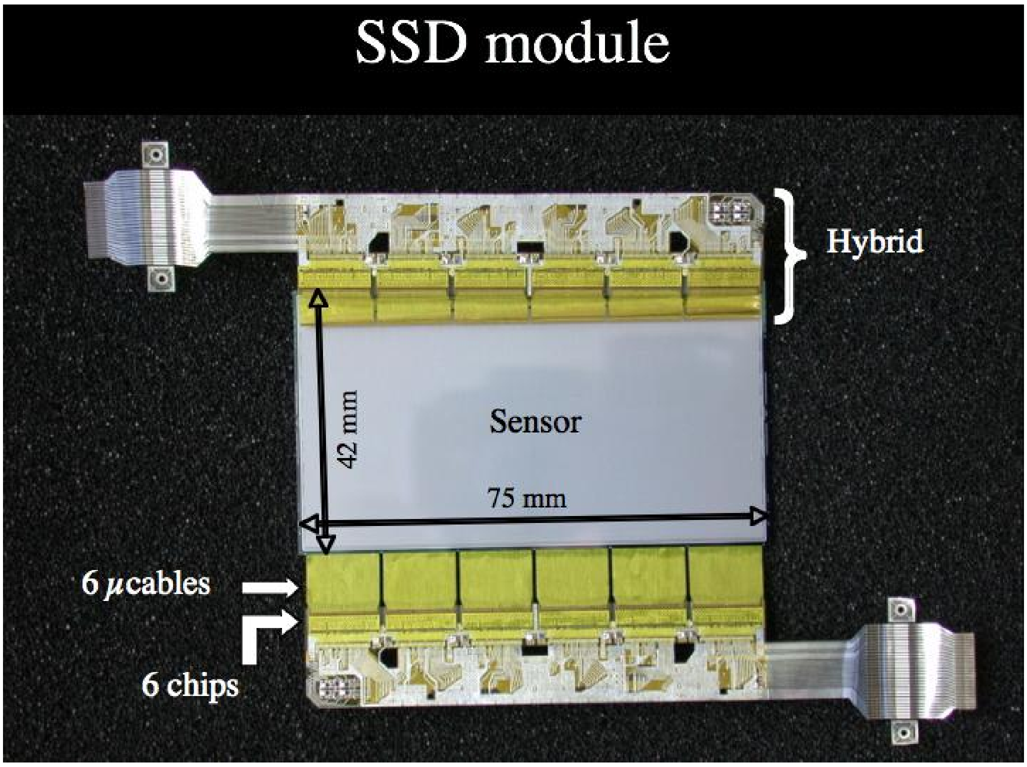

Figure 3.1: An SSD module, after the assembly of hybrids and sensor, as it appears in the unfolded configuration. The top and bottom hybrids are connected to the sensor front and rear face, respectively. Each hybrid is populated by 6 front-end chips, which are hidden by the μ-cables in the picture.

The sensor

The sensor is 300 μm thick and has a total area of 75×42 mm^2 [30, 31, 32]. 768 strips are implanted on each side; each strip is 40 mm long and the pitch between strips is 95 μm. The surface of each sensor side is surrounded by a line providing the bias voltage (*bias ring*) and another one protecting the sensor from border instability effects (*guard ring*); these lines occupy 1 mm along each side of the sensor, reducing the active area to 73×40 mm^2. On p-side, the strips are biased by punch-through from the bias ring; a similar scheme has been adopted on n-side, where the strips are biased by injection of electrons toward the bias ring, across a potential barrier created by the insulation structure (p-stop or p-spray). The strips of the sensor are oriented with an angle of 7.5 mrad with respect to the short edge of the sensor on the p-side and with an angle of 27.5 mrad on the n-side, forming an overall stereo angle of 35 mrad (see fig. 3.2).

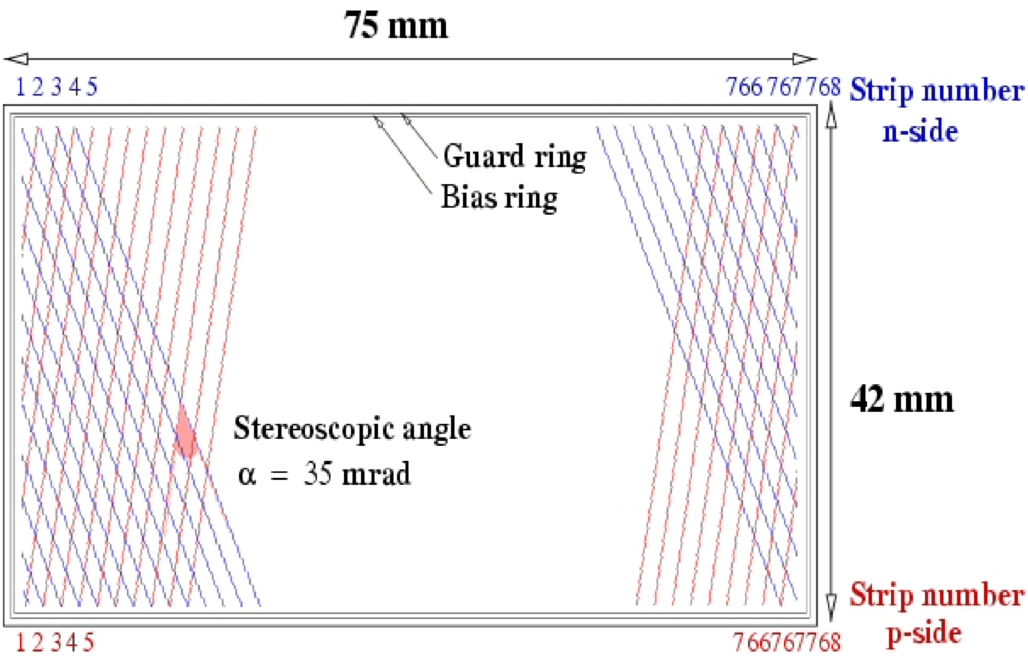

Figure 3.2: Sketch of the SSD sensor layout. The strip are disposed in order to form with the shorter sensor edge an angle of 7.5 mrad on the p-side and of 27.5 mrad on the n-side. The *bias ring* and the *guard ring* all along the sensor edges provides the bias voltage to deplete the junction and avoids border instability phenomena respectively.

This small stereo angle has been selected to limit the number of ambiguities resulting from the expected high particle densities. In these conditions, the probability to detect more than one particle with the same sensor is quite large: several strips can be fired in this case, or the same strip can interact with even more than one particle. The point reconstruction is thus ambiguous: in fig. 3.3, four fired strips allow the reconstruction of 4 different points; only one pair is originated by particle interactions, while the other two points are *ghost events*. Normally such ambiguities can be resolved thanks to the charge correlation between the P-side and N-side. As shown by simulations, the 35 mrad stereoscopic angle optimizes this ambiguity resolution.

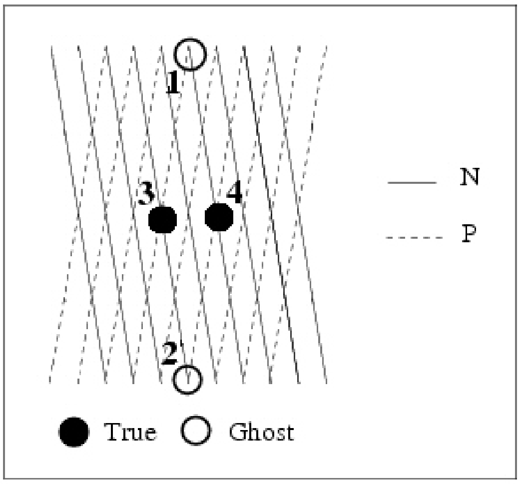

Figure 3.3: Ambiguities in the event reconstruction in case of two simultaneously fired pairs of strips. The actual interactions (3 and 4) can be discriminated from the ghost events (1 and 2) studying the charge correlation between the two sides of the module.

Mounting the sensors with the n- or p-side facing the interaction region in layers 5 and 6 respectively results in four different orientations of the strips with respect to the beam direction. This reduces the fake track probability significantly, resulting in much more robust tracking. The sensors are mounted with the strips nearly parallel to the magnetic field, so that the best position resolution is obtained in the bending direction. The main geometric characteristics of the sensor are listed in table 3.1. Before being used for assembly a detector, each sensor is extensively tested an a probe station in order to check its behaviour in terms of leakage current, depletion voltage and strip insulation and other parameters. The details can be found in [33, 34].

SSD sensor	
total area	75×42 mm^2
active area	73×40 mm^2
strip pitch	95 μm
read-out strips for each side	768
strip inclination (p side)	7.5 mrad
strip inclination (n side)	27.5 mrad
short strips (p side)	3
short strips (n side)	11
$r\varphi$ spatial precision	20 μm
z spatial precision	820 μm

Table 3.1: Main geometric characteristics of the SSD sensor. The *short strips* are the strips ending at the short sensor border, due to their inclination.

The HAL25 chip

The HAL25 is a mixed analogue-digital ASIC designed for the SSD read-out [35, 36, 37]. HAL25 has been designed in a 0.25 micron CMOS process; in addition, special design techniques have been used to meet the demands of low noise, low power consumption and radiation hardness required by the ALICE experiment. HAL25 has a very large dynamic range (about $\pm 350,000$ electrons, corresponding to about $\pm$ 14 MIPs in the case of 300 μm thick sensor) with a good linearity. The linearity of the response over the total dynamic range is shown in fig. 3.4 as resulted from laboratory measurements [38].

The chip has 128 input channels in a single row with 80 μm pitch and all its functionalities are remote-controlled via $JTAG$[1] protocol. Each channel consists of a preamplifier, a shaper and a capacitor to store the voltage signal proportional to the collected charge on a strip of the sensor. The pre-amplifier converts the charge input from the sensor into an analogue voltage step whose magnitude is a function

[1] $JTAG$ indicates the *Joint Test Action Group*, i.e. a group of electronics and semiconductor manufacturers which met to establish a solution to the problems of board test and to promote a solution as an industry standard. This solution is the IEEE Standard Test Access Port and Boundary-Scan Architecture: it allows test instructions and data to be serially loaded into a device and enables the subsequent test results to be serially read out [39].

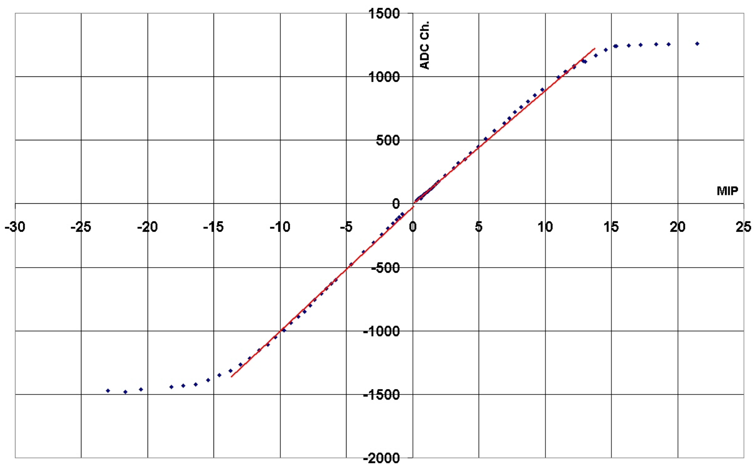

Figure 3.4: HAL25 dynamic range: for signals within the ±14 MIP range, the response is linear, with an error ≤ 4%.

of the charge. It uses a signal shaper whose shaping time is adjustable between 1.4 and 2.1 μs. The analogue signals are stored in a sample-hold circuit, controlled by an external HOLD signal. Once the analogue signals are stored they can be read out serially at 10 MHz through an analogue multiplexer. This voltage signal is finally converted to a differential current signal by a differential output buffer. A fast clear input allows abortion of the readout sequence when the event is rejected by the ALICE trigger system.

The chip is programmable via the JTAG protocol which allows:

- to tune the parameters of the analogue chains;
- to check the analogue behaviour of the chip by injecting adjustable charges to the inputs of selected channels with a programmable pulse generator;
- to test the interconnections and the chip functionalities (*boundary scan*).

These tests and read-out operations would be otherwise unfeasible, given the extremely reduced dimensions of its components: the particular technique used to connect the chip to the conducting traces allowed to reduce the channel pitch to 80 μm and the global chip dimensions to 11.9 mm × 3.65 mm × 0.15 mm.

The chipcables

The chipcables consist of a 10 μm thick polyimide foil which supports 14 μm thick aluminum traces [40, 41]. A chipcable fitting in a plastic frame, which facilitates handling and testing, is shown in fig. 3.5. All connections between the chips and the sub-hibrid and between the chips and the sensor are made by chip-cables connected via TAB[2] bonding. They allow for an easy testing of the chip before further use

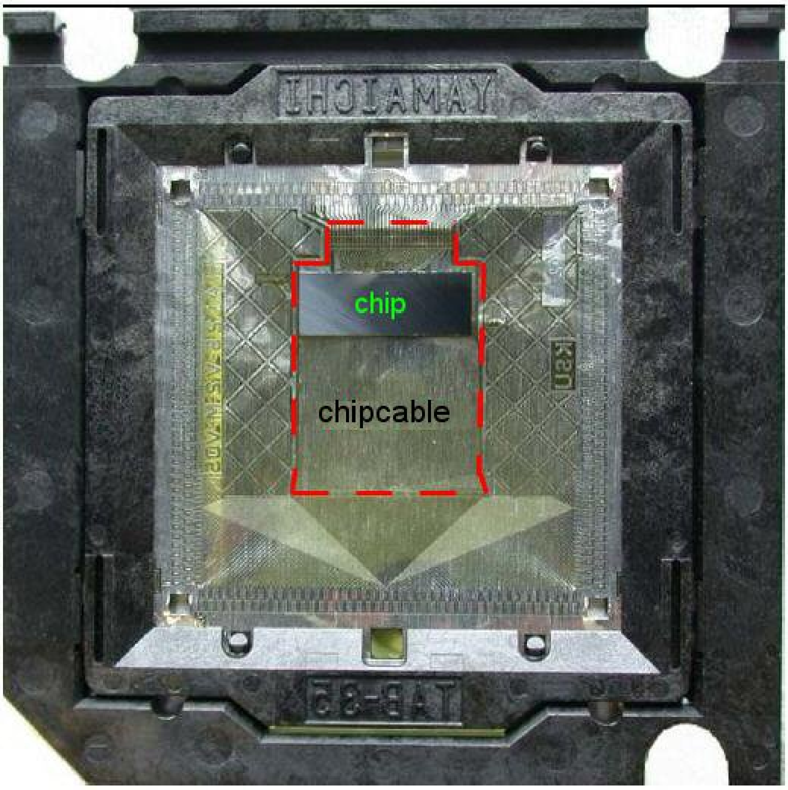

Figure 3.5: A framed microcable assembled with the chip to form a framed-chip. Once the microcable traces have been aligned with the pads of the chip, they are connected via TAB technique. Only the microcable region within the dashed red line is actually assembled in the detector, while the rest has the only functions to contact the test system and to fit in the plastic frames. Once connected to the HAL25 chip and tested, the surplus part is cut away.

and function as a pitch adapter between the sensor pads (95 μm pitch) and the chip input pads (80 μm pitch). In addition, the use of a flexible connection between

[2]TAB is the acronym for *Tape Automatic Bonding*: with this procedure, the input and output pads of a chip are soldered to the microcables and contacted with the sensor on one side and with the acquisition system on the other side. The TAB uses the ultrasonic micro-soldering technique: with a programmable and automatic procedure, the microcable is superimposed on the desired pad and pressed, while an ultrasonic emission provides to solder the objects together.

sensor and electronics makes it possible to fold the hybrids on top of the sensor, creating a compact object.

The hybrid

The hybrid is obtained placing six HAL25 chips on a sub-hybrid, i.e. an aluminum-on-polyimide hybrid circuit supported by a carbon fibre stiffener. The sub-hybrid is shown in fig. 3.6.

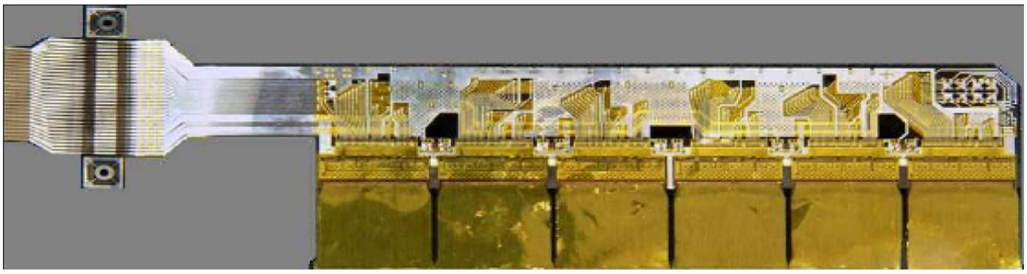

Figure 3.6: A hybrid, with 6 chips bonded on top, connected to the test system. The carbon fiber stiffener is on the rear side.

The sub-hybrid is made of a two layer flex circuit, each layer having 30 μm thick aluminum traces on top of 20 μm polyimide. It hosts power lines as well as digital and analog lines needed for controlling and reading the chips, while the stiffener provides mechanical support and cooling distribution. The electrical connections between the chip channels and the sensor strips are obtained bonding the aluminum chipcable traces with the pads present on the sensor surface via tape automatic bonding (TAB) technique (128 connections per chip); the same for the connections between chip and sub-hybrids traces ($\sim$55 connections per chip). This assembly provides optimal electrical, mechanical and thermal performances associated to a very low mass for good radiation transparency.

3.2 The construction of the SSD modules

The two layers of the SSD contain a total of 1698 modules. In additions, the construction of spare devices is requested: therefore the overall number of produced SSD modules grows up to about 2000. These large numbers require an efficient assembly procedure and an exhaustive test protocol. The procedures have been designed and scheduled in order to allow the monitoring of the operations: at the end of each single production stage the intermediate products have been tested in order to verify their complete functionalities, both with electronic tests and with accurate visual inspections.

The module assembly is split in three steps:

1. In the first step HAL25 front-end chip is assembled with a chipcable into a *tabbed chip*: the chipcable pads and the chip pads are aligned to match with a precision better than 5 μm. Vacuum and mechanical locks keep steadily in position the chip and the chipcable through specifically designed holders. The pads are connected via TAB bonding and the product (the so called *tabbed-chip*) is tested; after disposing a protective glue on the bonds, the tabbed-chips are tested again and cut out from the frame. The procedure is summarized in fig. 3.7;

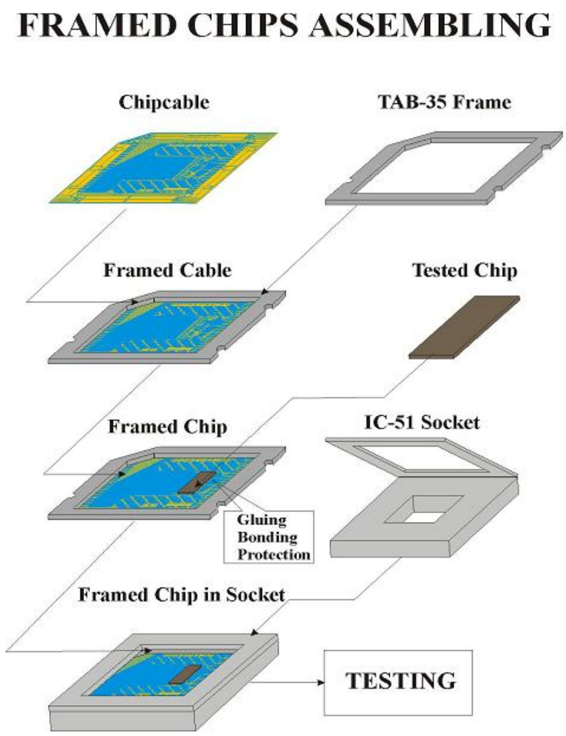

Figure 3.7: The assembly steps of a chip on the microcables. From top: the chipcable fitting a frame is aligned and bonded with a chip; the assembled tabbed-chip is glued to protect the bonds and tested.

2. Six tabbed-chips are then mounted on a sub-hybrid to make a hybrid: the procedure uses a hybrid holder equipped with seven separate vacuum lines

to keep a sub-hybrid and six tabbed-chips in position. In the hybrid building phase the hybrid holder is placed on the aligning base, where also sits a dummy sensor. Once the tabbed chips are aligned with the sub-hybrid and with the dummy sensor pads at the same time, the chips are glued on the sub-hybrids; finally they are interconnected via TAB bonding to form a hybrid, that is then tested. Fig. 3.8 schematically shows the operations performed in this step;

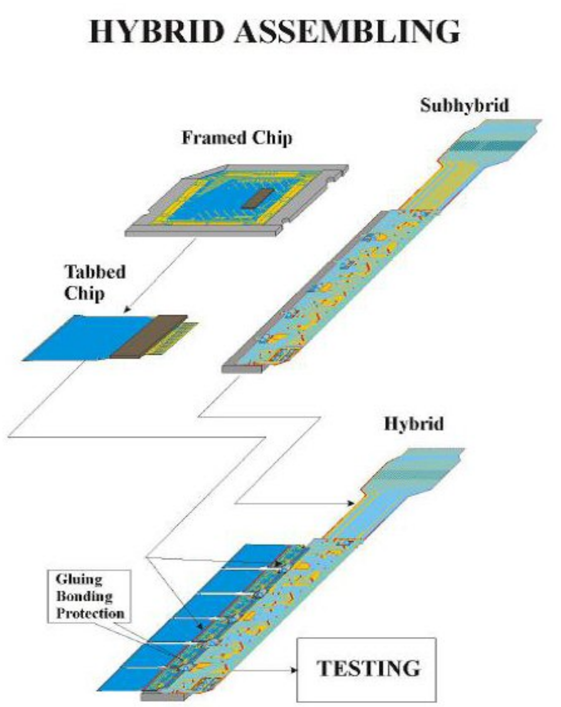

Figure 3.8: The assembly steps of a framed chip on a hybrid. From top: six working framed chips are cut out from the frame and connected via TAB bonding to a sub-hybrid forming a hybrid; the bondings are then protected and fixed with glue; thus the hybrid is tested.

3. Finally, two hybrids are mounted on a sensor according to the schemes of fig. 3.9: firstly a hybrid is aligned on the sensor and its traces are TAB-bonded on the sensor pads; the resulting half-module is accurately tested. Then the half-module is flipped up side down and the second hybrid is aligned and interconnected. The produced module is tested and its hybrids are folded on top of the sensor. The module is now ready for the final quality validation test.

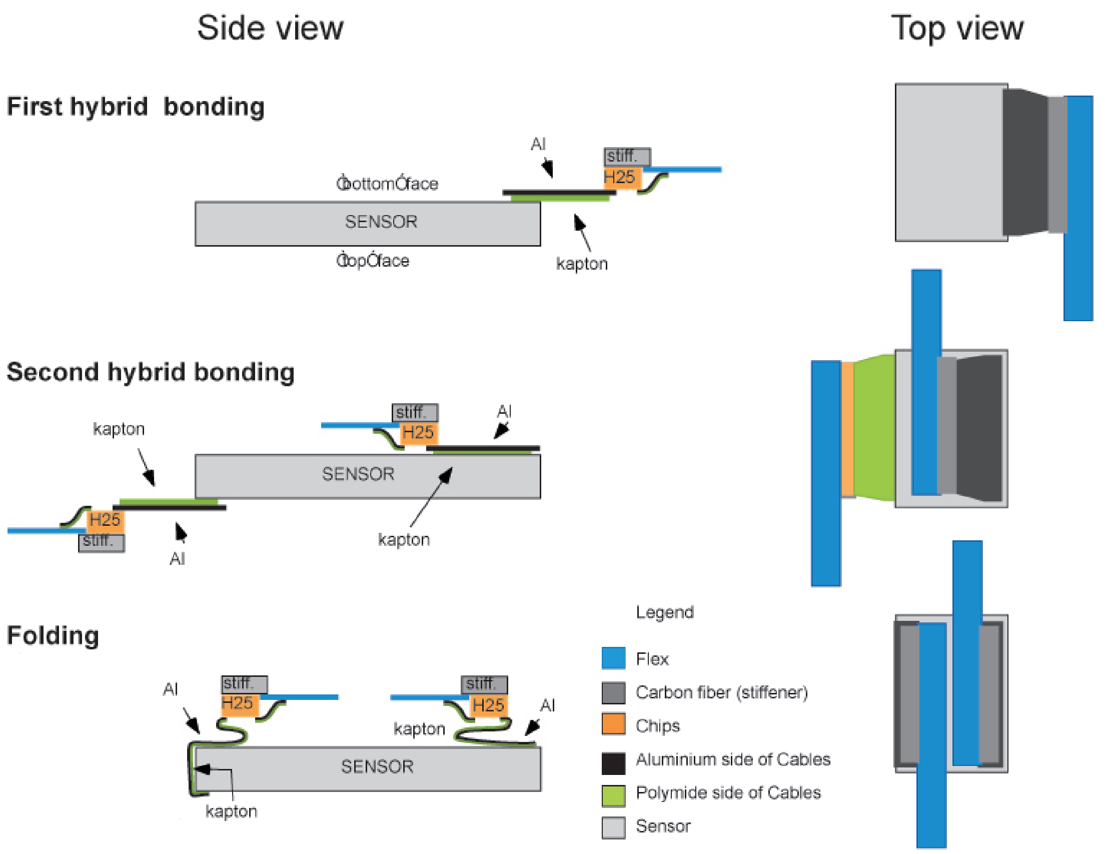

Figure 3.9: The three assembly steps of two hybrids on a sensor. From top: the hybrids are aligned and bonded on the module in two steps as by the figure. The device is tested after each operation; both hybrids are folded on one side of the produced module.

3.3 The module characterization

The strict requirements imposed to the SSD performances by the ALICE physics programme forced to keep the quality of the modules close to the full efficiency. In order to provide the required spatial resolution and to measure the specific ionization with an acceptable signal-to-noise ratio over the full azimuthal coverage and over the two central units of pseudorapidity, the quality of the components before and after each single assembly operation was evaluated and monitored: the goal was to produce devices with at least 98% properly working channels out of the 1536 channels of a module.

A complex and at the same time very general test was designed to help achieve this challenging objective: such a test is expected both to completely characterize each single SSD channel and to measure the global properties of the produced devices; in addition, it should be comprehensive enough to spot and identify also unexpected and exotic defects, possibly suggesting their origin. The test applied during the construction operations is based on the measurement of some basic parameters and on the processing of the acquired data, which results in a quite fine defect identification.

In the following paragraphs the parameters which have been the object of the tests are described in detail and the procedure is explained. In addition the specific tests that have been carried out in case of particular problems and defects are presented.

3.3.1 Monitored parameters and test procedure

Measuring a set of simple parameters, the test system is capable to evaluate the general behaviour and the single channel functionalities of an SSD module; through the interpretation of these measurements, it identifies eventual construction defects. The stages of the test procedure are described hereafter [42].

- **The digital tests and settings.** A first phase of the test is devoted to check the JTAG registers, the connection chain and the internal components of the chips. In this phase, the chips are recognized and their serial number is read-out; the voltage and current parameters of the chip are set at the desired values; the analogue read-out is enabled.

- **Single channels response.** The output response of each channel is evaluated for the unbiased sensor. Through a sample of acquisitions triggered at a fixed frequency, the test system evaluates for each channel the characteristic offset (fig. 3.10), i.e. the pedestal, and noise (fig. 3.11), as the mean and the variance of the signal distribution; this distribution is typically Gaussian, as verified on a large sub-sample of channels. The coherent oscillations of the baseline of groups of adjacent channels, the so called *common mode noise*, is calculated as well by the test software, and corrected; for a detailed description of the algorithm used to calculate noise, pedestal and *common mode*, see 4.3.1. Afterwards, injecting an adjustable charge quantity into the channel input through the internal HAL25 pulser, the test system measures the output response (fig. 3.12). These measurements, which are repeated also while applying the bias voltage, will be later used to identify possible defects.

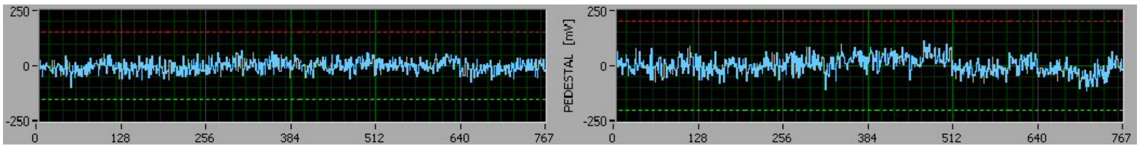

Figure 3.10: The pedestal of the P-side (*left*) and N-side (*right*) channels.

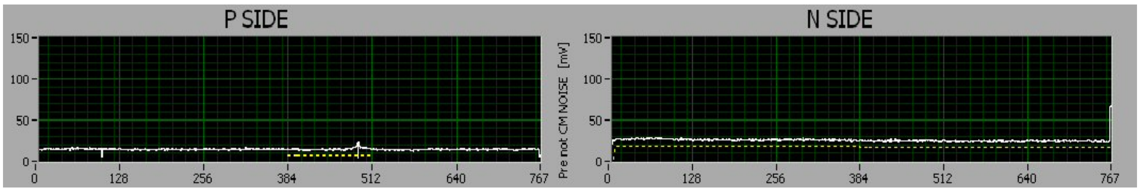

Figure 3.11: Noise measurement without applying any bias voltage. The noise is shown as a function of the P-side (*left*) and N-side (*right*) channel number.

- **The I-V curve.** The leakage current is measured as a function of the applied bias voltage, both polarizing the sensor in reverse bias for defining the depletion voltage, and in direct bias, to spot eventual problems in the bias circuits of the electronics and of the sensor. The depletion voltage is defined observing the behaviour of the N-side noise as a function of the increasing applied bias voltage: the value where the noise reaches the stability is taken as the depletion voltage.

- **Defect identification.** The resulting depletion voltage is applied to the sensor. The response of the channels is evaluated without (fig. 3.13) and with (fig. 3.14) injected signals at the inputs and the results are cross checked to detect and classify the defects in the following categories:

  1. *Dead channels:* the channels presenting very low response ($<$ 10% of the mean response of the module side) to injected charges, and with low noise ($<$ 50% of the mean noise of the module side) are tagged as *dead*; these effect are probably caused by broken components in the signal processing chain.

  2. *Open channels:* the connection between the sensor and the electronics is interrupted somewhere; when no bias voltage is applied, this results in a lower noise with respect to the mean noise level, since the contribution to the noise of the input load capacitance is absent for such channels; moreover they present an enhanced response to the charge injection since no charge is lost in the sensor, which is disconnected in this case.

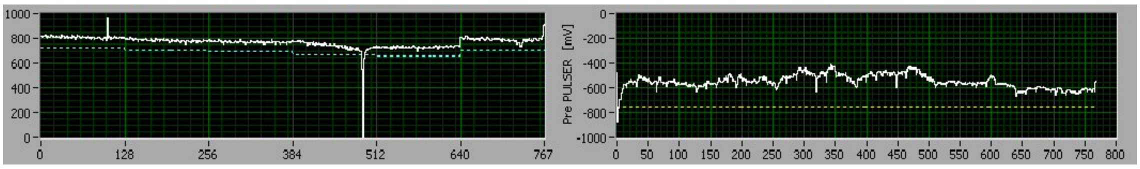

Figure 3.12: Undepleted sensor response to a charge injected in the channel inputs by the HAL25 internal pulser. On the P-side (*left plot*) one channel with zero-response is visible close to channel 512.

3. *Noisy channels:* the channels are tagged as *noisy* if they have measured noise larger than a fixed threshold defined on the basis of the required signal-to-noise ratio.

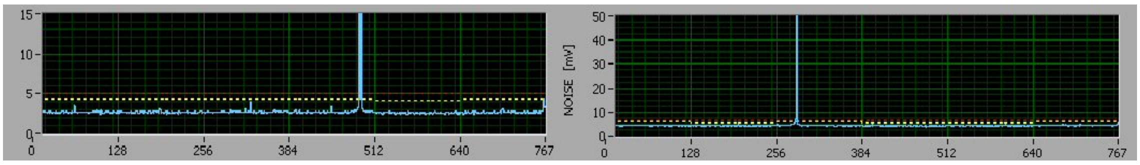

Figure 3.13: The noise measured at the depletion voltage. The peaks show the presence of *high noise* channels both on P-side (*left*) and N-side (*right*).

4. *Low-gain channels:* some channels present a response to an injected charge different from the behaviour of the rest of the module side; the preamplifying electronics of the channels with such a *problematic gain* is not properly working.

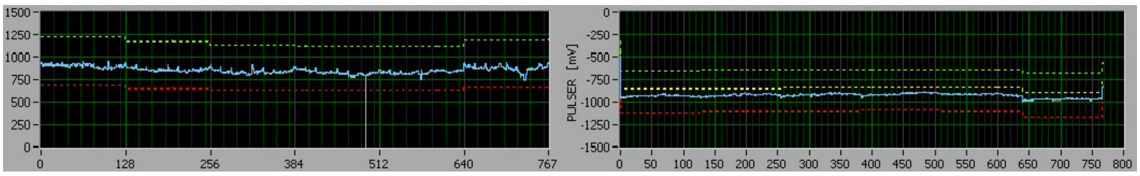

Figure 3.14: The response to the injected charge at the depletion voltage is measured; through a system of thresholds (*coloured dashed lines* in the plot) the functionalities of the pre-amplifying electronics is evaluated. The P-side channel with zero-response, already detected without applying any bias voltage, is visible on the left panel.

5. *Broken AC:* a damage in the silicon-oxide-metal system can cause a modification in the capacitive network of a channel, e.g. shorting the aluminum pad to the underneath implant. This defect weighs on the noise measured in direct and reverse bias and on the response: it is spotted by the test system taking into account all these measured effects.

6. *Short-circuited channels:* the internal pulser injects a charge in one input at a time and the neighbouring channels is read-out; if a not negligible response is recorded, the channels are tagged as *shorted*.

- **Global quality assessment.** The overall quality of the detector has to be univocally and homogeneously defined, regardless of the different types of defects, in order to allow a direct comparison with a quality standard or between different modules. The quality mark is obtained counting the single channel defects and subtracting this computed number from 100: a module without defects has quality Q = 100; the maximum acceptable number of defects is equal to the 2% of the total amount of channels, i.e. $\sim$ 30 channels out of 1536, that corresponds to a minimum required quality of Q=(100-30)=70. In presence of serious global defects like high bias current or an interruption in the digital chain, the assessed quality is Q=0.
- **Transparent test.** At the end of the test procedure, in order to monitor the shape of the output signals, the first defect-free channel is considered: its response to an injected pulse is sampled and plotted as a function of the time.

The final output of the test system is showed by the screenshot in fig. 3.15 in the case of 100% quality module, i.e. in absence of defects. The results of the measurements and the defects are also saved in a textual report and stored in an on-line database.

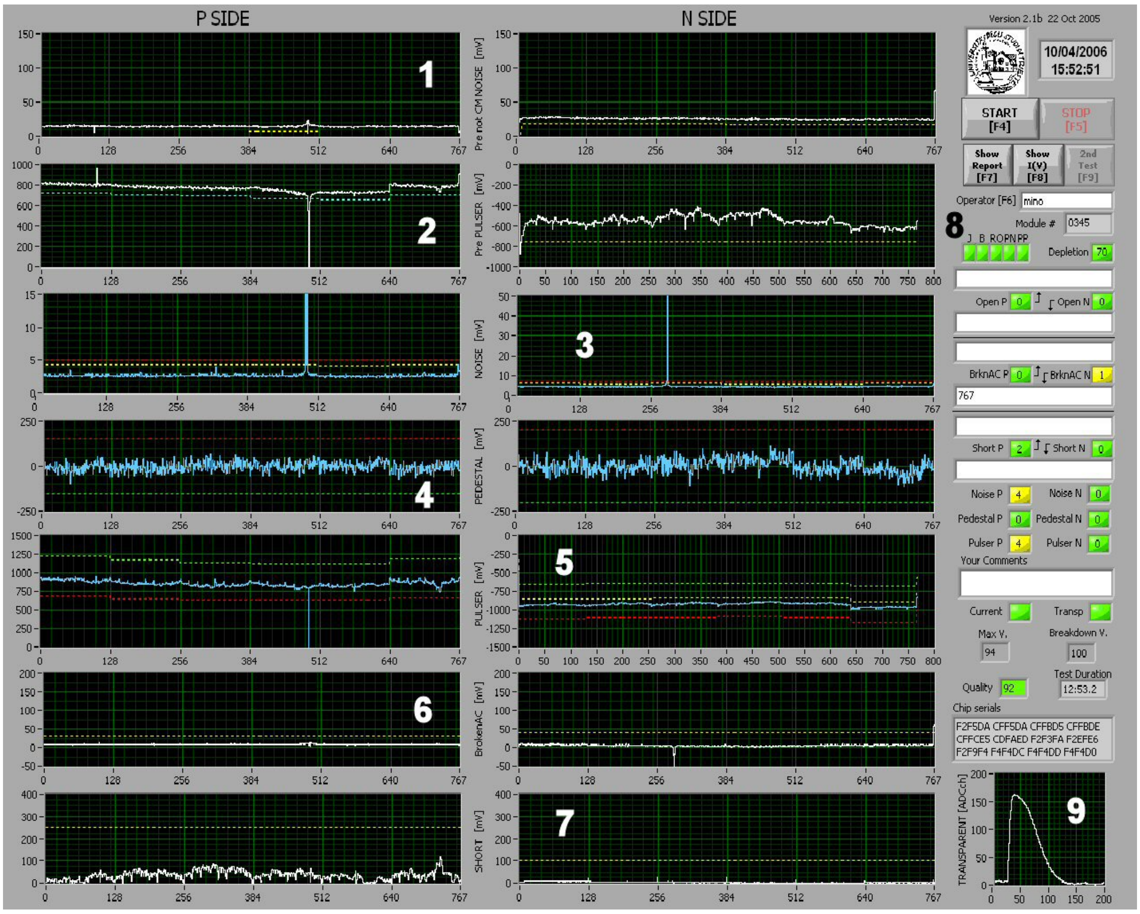

Figure 3.15: Screenshot of the test system output showing the test results for a good quality object, i.e. a module with more than 98% properly working channels. The plots show on two columns corresponding to the p-side (*left*) and the n-side (*right*) the results of the measurements of the following quantities as a function of the channel number: the noise before the depletion (*1*), the response to an injected pulse signal before the depletion (*2*), the noise after the depletion (*3*), the pedestal (*4*), the response after the depletion (*5*), the computed parameter used for the definition of the *broken ACs* (*6*) and the *shorted* channels (*7*). On the right section of the screenshot, a summary of the defects, divided by defect class, is presented; moreover, the digital test results (*8*), the depletion and breakdown voltages are shown. The last *bottom right* plot (*9*) shows the typical shape of a read-out. The global quality is finally computed and shown.

3.4 Constructing problems and defects

The detection of the defects, which was performed simultaneously with the assembly operations, allowed to give a feedback to the production, resulting in a continuous tuning of the bonding parameters, in the choice of the most suitable materials and tools for the different operations and in the improvement of the procedures. In this way, a large number of defect typologies was solved during the mass production and mainly regarded very localized problems.

3.4.1 Defects caused by TAB bonding operations

One of the most critical operation performed on the SSD components is the TAB bonding: in spite of the high efficiency reached over the global production, this procedure needed a close and constant monitoring to overcome any failure and to prevent damages on the products. Slight differences in the shape and in the pitch of the microcables traces with respect to the nominal values, even if compatible with the production tolerance limits and the optical test requirements, can cause a misalignment between traces and contacting pads, resulting in defective contacts; moreover, sometimes the force applied by the bonding tool could be insufficient to settle a stable contact. In these cases, immediate tests performed on the produced devices, like the framed chips and the hybrids, promptly show these defects, tagging as *open* the failed bonds. A further processing of the examined products solved the majority of these defects.

Open contacts can happen also while connecting the hybrid traces with the sensor aluminum pads, during the module assembly, again caused by microcable patterns not fitting the pad; in some cases, it can be also due to some sensor surface contamination that prevents the contacting material from adhering on the pads, making the TAB technique ineffective. A further processing often solves the problem, even if the suitability of this solution is carefully evaluated in each case, since it can cause more serious problems, such as the one considered in the following paragraph.

3.4.2 *High current* problem

Among the various types of defects found on the assembled modules, an unexpected behaviour of the leakage current of the sensor as a function of the applied bias voltage was detected by the test system on tens of produced devices. In this section, the defect investigation and the specific measurements performed to understand its origin and find out a solution are described; data refer in particular to one of the first modules produced in Trieste that presented this sort of problem. First of all, the standard test shows for these modules a sharp increase of leakage current (see fig. 3.16) at a voltage value that is in the vicinity of the nominal depletion (i.e. the N-side insulation) voltage, which is known from the sensor tests performed before the assembly [34]. The slope of the curve suggested an unexpected path followed by the current.

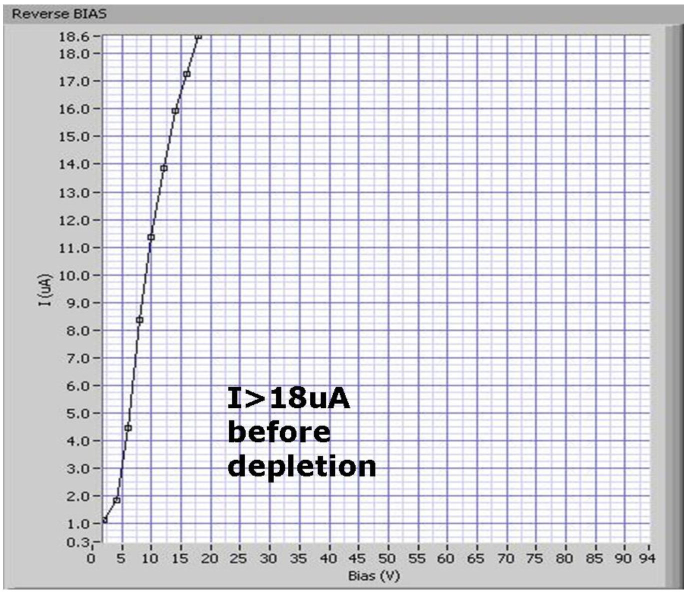

Figure 3.16: Screenshot of the test system output showing an unexpected high leakage current, measured as a function of the applied reverse bias voltage. The current increases rapidly overpassing 18μA at 20 V (while the typical SSD sensor current at depletion is $\sim$1÷2 μA). Due to the voltage drop through the 1MΩ resistance, the sensor can not be depleted.

Actually, the real depletion of the sensor assembled in the module cannot be reached, since the voltage drops through the 1MΩ bias resistor in series to the sensor, simulating the resistors embedded in the end-cap electronics of the SSD final configuration. Thus the considered module can not be properly operated. The SSD module bias circuit is schematically shown in fig. 3.17. The red arrows indicate the unexpected path followed by the current in the modules with the problem here discussed.

Moreover, a group of channels presenting very high noise is spotted in these modules somewhere on the N-side at the nominal depletion voltage; at the first analysis

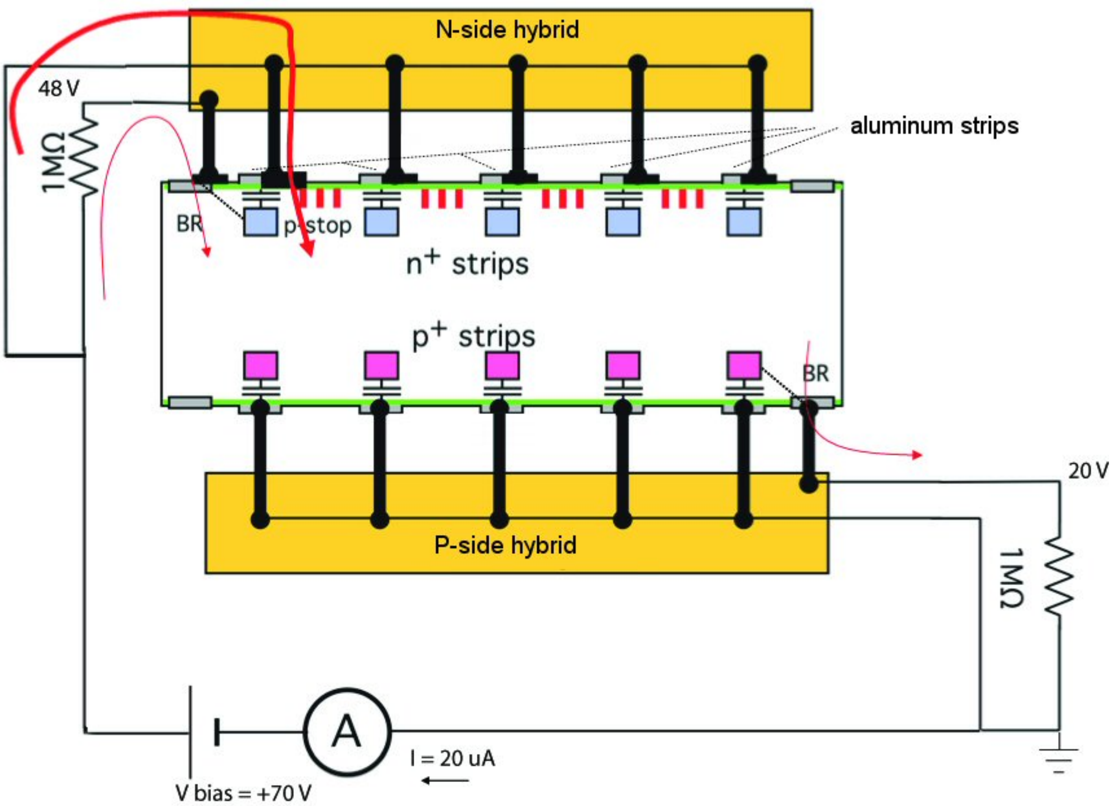

Figure 3.17: Connection scheme used for I-V measurements on modules. The measured leakage current follows an unexpected path in case of the damage of the surface described in the text: this path is shown in the figure by the red arrows. Exemplifying values are indicated in the schemes.

of the test data, the two defects cannot be associated since groups of noisy channels frequently appear, without any correlation with the I-V regime. A screenshot of the test system output for a module presenting this defect is shown in fig. 3.18; the detail of the N-side noise is spotted in fig. 3.19.

A possible connection between the two defects can be hypothesized approaching the problem from two different points of view: on the one hand some specific read-outs at different bias voltages spot a large increase in noise proportional to the bias current; on the other hand, inspecting at the microscope the surface of the module in the region corresponding to the noisy channels, it's possible to notice a misalignment of the aluminum trace with respect to the bonding pad (see fig. 3.20 for a visual comparison between aligned and displaced traces), which caused the bonding tool to contact directly the sensor surface, presumably damaging the oxide above the p^+stops (see the detail picture in fig. 3.21).

This suggests the possibility of a short between a metal strip on N-side and

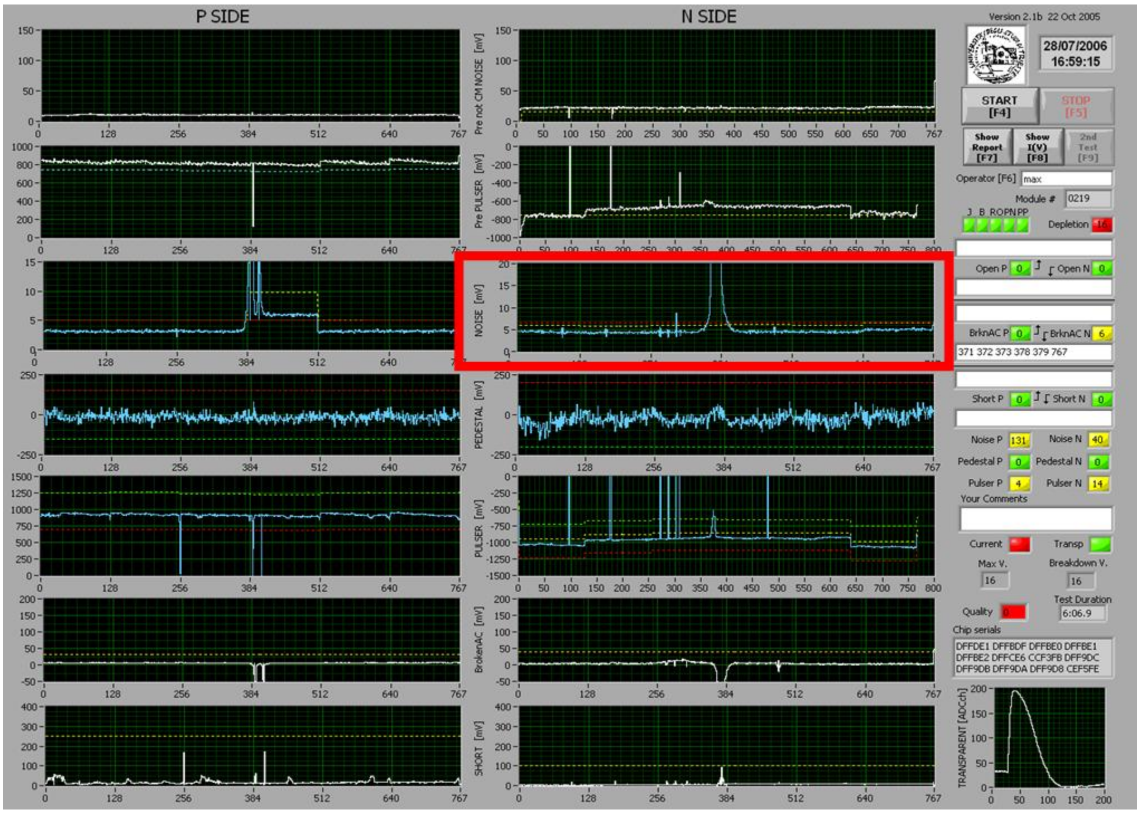

Figure 3.18: Screenshot of the test system output in case of a problematic module: the noise measurement spots a group of very noisy channels (up to ∼100 rms ADC units, out of scale in the figure) on the central region of the N-side (noise is better shown in fig. 3.19). This defect, added to the instability caused on the opposite side and to the high leakage current measured while biasing the sensor, results in a *zero quality* assessment for this module.

a p^+stop implant [43]. Normally, the p^+stops charge up to a negative voltage with respect to the n^+strips (a few Volts, increasing with bias) when the sensor is depleted. If this is prevented by the accidental connection to a metal strip that keeps the p^+stop voltage at the N-side electronics level, a large current of holes is injected from the p^+stop and is collected by the P-side strips. The flow of the current in the case of the described short is shown by the red arrows in fig. 3.17.

In order to confirm this interpretation and to clearly spot the link between high current and noise, specific measurements of the *I*-*V* curve can be performed: for this purpose, the bias circuit was modified separating the sensor bias voltage and electronics voltage (see 3.22) for the circuit description), an I-V curve is made leaving the N-side hybrid completely floating (green curve in fig. 3.23, green curve). Even if the p^+stops are connected to the metal strips as a consequence of the damage, they

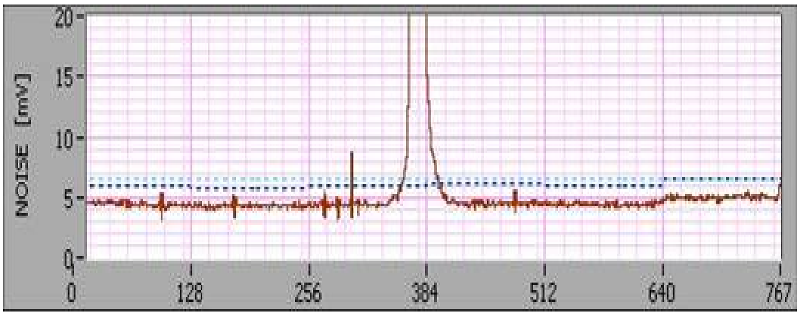

Figure 3.19: Example of the high noise region detected on the N-side of the modules with high current. The plot shows the measured noise as a function of the N-side channel number, spotting a group of channels with up to σ = ~100 rms ADC units (over-range in this figure), very high if compared to the ~5 rms ADC units measured on average on the same module side.

are free to settle at the appropriate voltage, and the I-V curve returns to normal values.

In fig. 3.23 the other I-V curves are taken with an additional voltage (4V for the red curve, 7V for the yellow one) applied to the N-side bias ring with respect to the hybrid floating ground (see fig. 3.24 for the connections). Considering for example the case of a 7V extra-voltage, the N-side hybrid, and thus also the $p^{+}stop$ that is shorted to the metal strip, sits at -7V with respect to the N-side bias ring, and at V= -7V + $V_{punch-through}$ with respect to the n^+ strips. The bias voltage reported in the x-axis keeps into account the additional 7V applied to the N-side bias ring and it is corrected for the voltage drop through the P-side bias resistor. This additional voltage keeps the p^+stop sufficiently negative to prevent the hole injection, until the effective bias applied reaches about 100V. At this point the punch-through voltage is large enough to offset most of the 7V difference, and hole injection begins. Cutting the connection between the shorted p^+stop and the electronics is therefore supposed to solve the problem. In order to minimize the loss of operating channels, an extensive campaign of dedicated measurements has to be carried out: at the probe station, the surface of the detector is locally illuminated and the induced current flowing through the sensor is measured contacting the pad corresponding to the suspected damaged implant. Anyway, the traces identified as the source of the current are cut out on the microcable close to the bonding pad, by using a micro-manipulator with a tungsten needle. Therefore, the module is recovered in this way in spite of just one channel lost. This procedure was applied extensively to all the high current defective modules, allowing the recovering of almost all them.

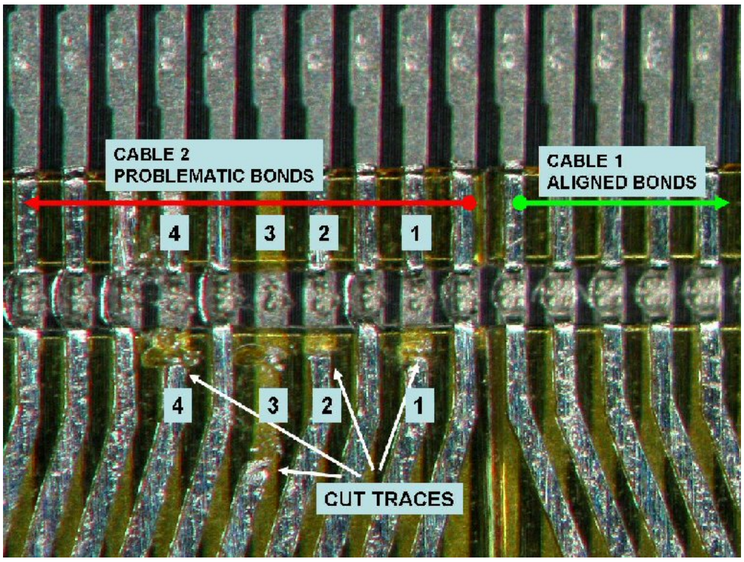

Figure 3.20: Detail of the sensor surface in the bonding pads region. The microcables (yellow bottom part) is connected to the sensor via TAB bonding of its traces on the sensor pads. The traces belonging to the microcable on the right (green arrow) are well aligned with the sensor aluminum strips. Instead, the left microcable (red arrow), badly aligned with the sensor strips, shows an evident displacement of the aluminum traces at the bonding point: the bonding tool, not being well aligned with the trace axis, hits the pad only partially, displacing the aluminum strip and directly hitting the sensor surface in the p^+stop region (the bonding pad detail is shown in fig. 3.21). This resulted in a damage of the sensor and probably short-circuited the p^+stop implants with the read-out electronics. The numbered traces have been cut out in order to exclude shorts and to solve the problem.

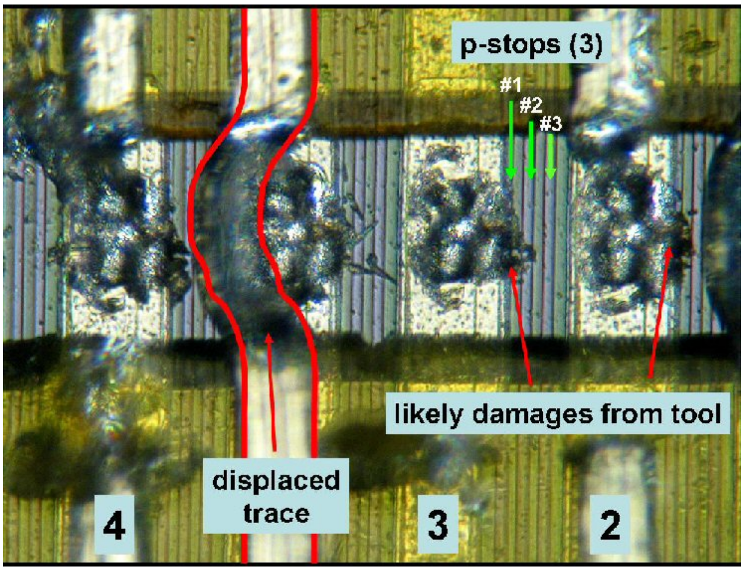

Figure 3.21: Zoom on the bonding pads region. The bonding tool print on the oxide covering the p$^+$stops is clearly visible. The damage probably created a short-circuit between the electronics and the p$^+$stops. An aluminum trace displaced by the bonding tool is highlighted; the other aluminum traces have been already cut out.

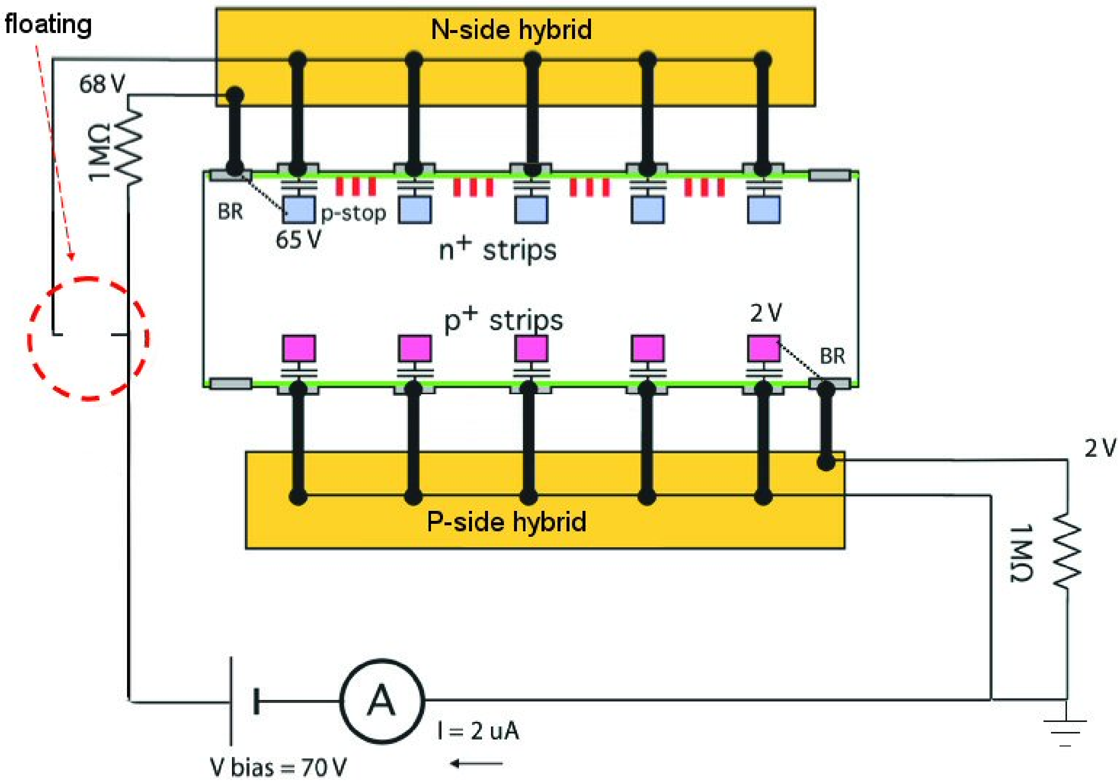

Figure 3.22: Connection scheme used for I-V measurements on modules. The sensor bias voltage and the electronics voltage lines are now separated. The I-V curve is thus made leaving the N-side hybrid completely floating.

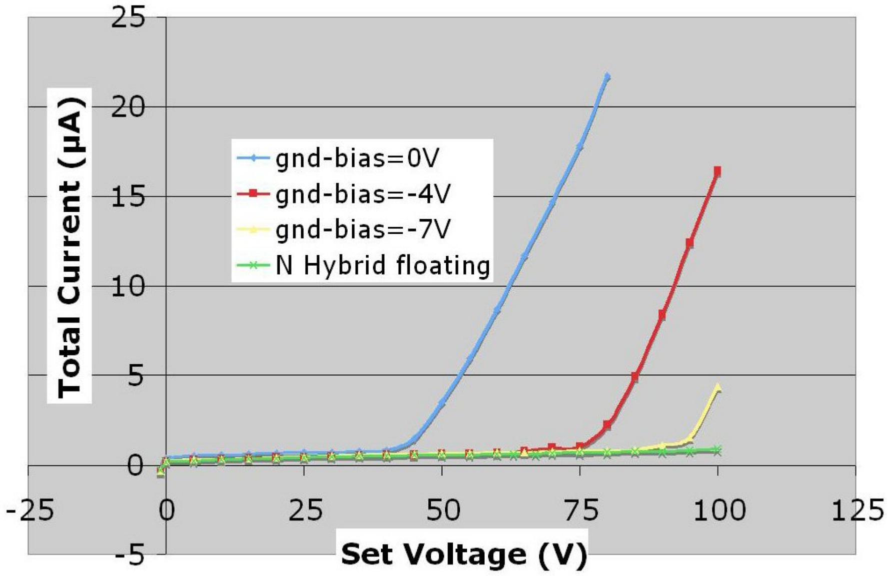

Figure 3.23: Reverse bias I-V curves of the investigated problematic module. The bias voltage is applied to the P-side electronics and (through a 1 MΩ resistor) to the P-side Bias Ring. The blue curve represents the measurement in the standard working configuration (ΔV=0 between the N-side bias ring with respect to the hybrid floating ground, neglecting the voltage drop on the resistance): it shows a rapid increase of the current before the depletion. The other curves show the measurement in the specific test configuration: an additional voltage ΔV of 4V and 7V (*red* and *yellow curve* respectively) is now applied through a 1 MΩ resistor to the N-side bias ring with respect to the hybrid floating ground. Now the rapid increase of current takes place at a higher voltage in case of 4V extra-voltage, while the current is below 5μA for the full bias-scan range when 7V are applied. The green curve represents the measurement performed leaving the N-side hybrid completely floating; the I-V curve is brought to the typical behaviour.

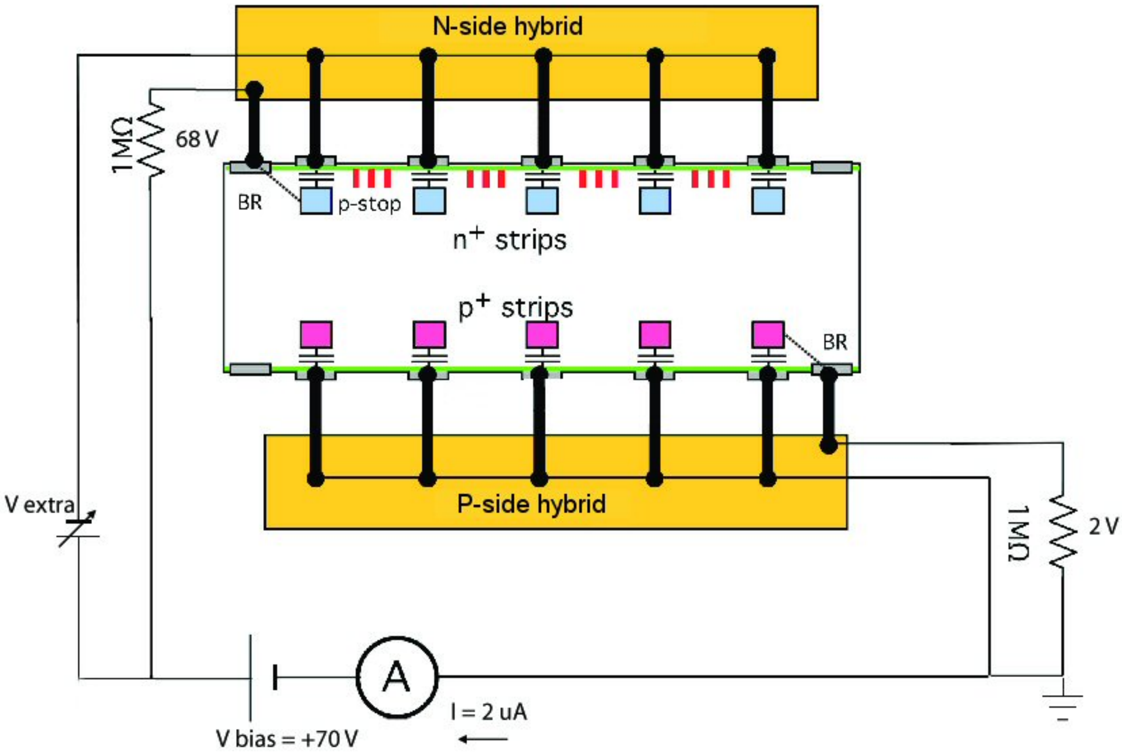

Figure 3.24: Connection scheme used for specific I-V measurements on problematic modules: it allows the separate control of the N-side hybrid and the sensor bias voltages. The voltage source added to the circuit for this particular test is shown on the left part of the figure. It provides a tunable ΔV between the N-side bias ring and hybrid keeping the p^+stop sufficiently negative to prevent hole injection.

3.4.3 High noise in *Sintef* modules

A particular behaviour was noticed on the modules which use Sintef sensors. While biasing the module, with the N-side strips still not insulated, the noise on the P-side increases; this effect firstly interests the lateral strips of the P-side, later extending to the whole side at higher voltages: the noise eventually measured at the depletion voltage is up to 5 times larger than the typical P-side noise measured on ITC and Canberra sensors. Previous tests performed on the sensors before the assembly, suggest to associate this behaviour to the intrinsic characteristics of the silicon sensor used, which play a crucial role in the depletion phase [33, 34, 44].

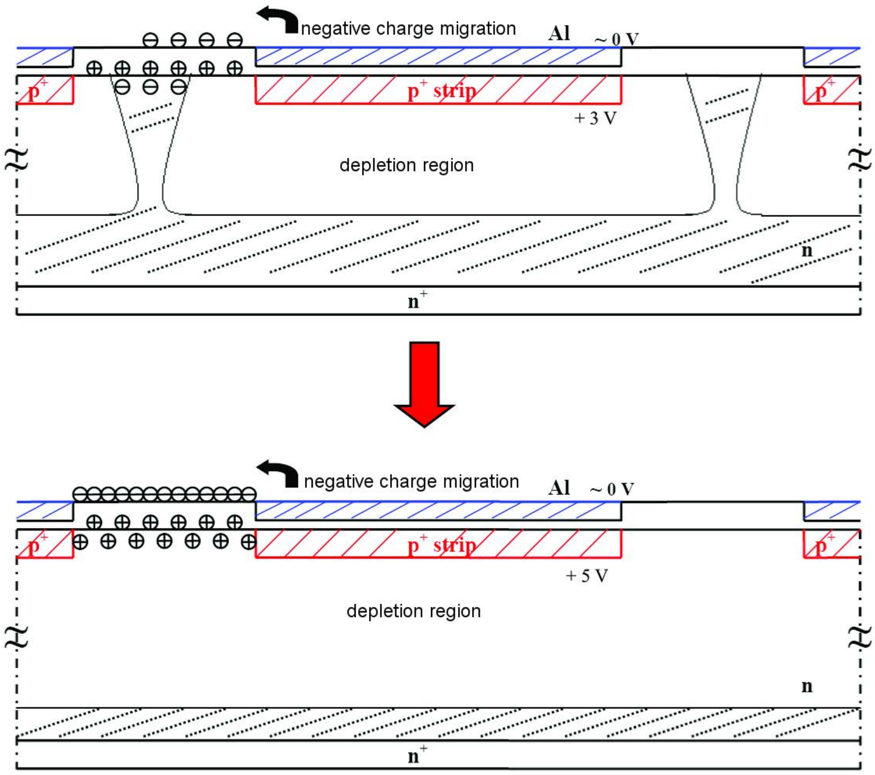

Figure 3.25: The type inversion mechanism at the surface of the Sintef sensors. In the *top panel*, with the increasing reverse bias voltage, while the bulk starts to deplete, negative charges start to migrate from the traces towards the oxide bringing the surface at the same potential; the p-strips are still insulated by the negative charges of the n-bulk. Once completely depleted (*bottom panel*), the negative charges start to accumulate in the oxide and attract positive charges at the surface from the bulk: the surface is thus driven into inversion and shorts together the p-strips.

The above mentioned measurements showed the mechanism here described: grounding the P-side bias ring, the strips, biased by *punch-through*, sit at a few Volts above the bias ring level, equipotential to the aluminum traces on the surface. While increasing the reverse bias voltage, negative charges start to migrate from the traces towards the oxide bringing the surface at the same potential. Since the Sintef sensor are fabricated with a process yielding low oxide charges ($\sim 10^{10} cm^{-2}$) with respect to the $2 \div 4 \cdot 10^{11} cm^{-2}$ of the ITC sensors [33, 34], the oxide charge are easily neutralized, thus the negative charges begin to accumulate in the oxide starting, starting to attract positive charges at the surface from the bulk: the surface is thus driven into inversion and shorts together the p-strips. The described inversion mechanism is schematically shown in fig. 3.25.

In order to confirm this picture, specific tests were carried out on the Sintef modules. The circuit used in this measurement is shown in fig. 3.26. In order to decrease the potential difference between the p-strips and the aluminum traces to avoid the accumulation of negative charges in the oxide, the surface potential is kept low applying an opposite voltage (V *extra* in the figure) to the P-side electronics with respect to the bias ring. The threshold voltage for the bulk inversion mechanism is thus increased and the p-strips maintain their insulation.

Measuring the noise in this condition demonstrates that the extra-voltage applied to the P-side electronics with respect to the bias ring solves the problem. Fig. 3.27 shows the effect of the application of an opposite extra voltage: the high noise measured on the module biased in the standard configuration (*top panel*) disappears applying a 2.5 V extra-voltage (*bottom panel*).

The problematic Sintef I-V curve shows a quite peculiar behaviour: as shown in fig. 3.28, the curve does not reach the typical depletion plateau of a reverse biased diode. After reaching the maximum value, the current starts to slowly decrease with the increasing applied voltage when the bulk inversion mechanism takes place: the bulk inversion suppresses the hole-electron pair generation and therefore the generation current. The necessary modifications to the power supply circuits in the experimental site needed for the application of this additional voltage were implemented in the detector electronics.

3.4.4 Mechanical damages of the hybrids

The last steps of the modules production, namely the assembly of sensors with the hybrids, faced also problems originated by mechanical damages, like broken, pulled out or cut traces at the hybrid level. These defects occurred in correspondence to

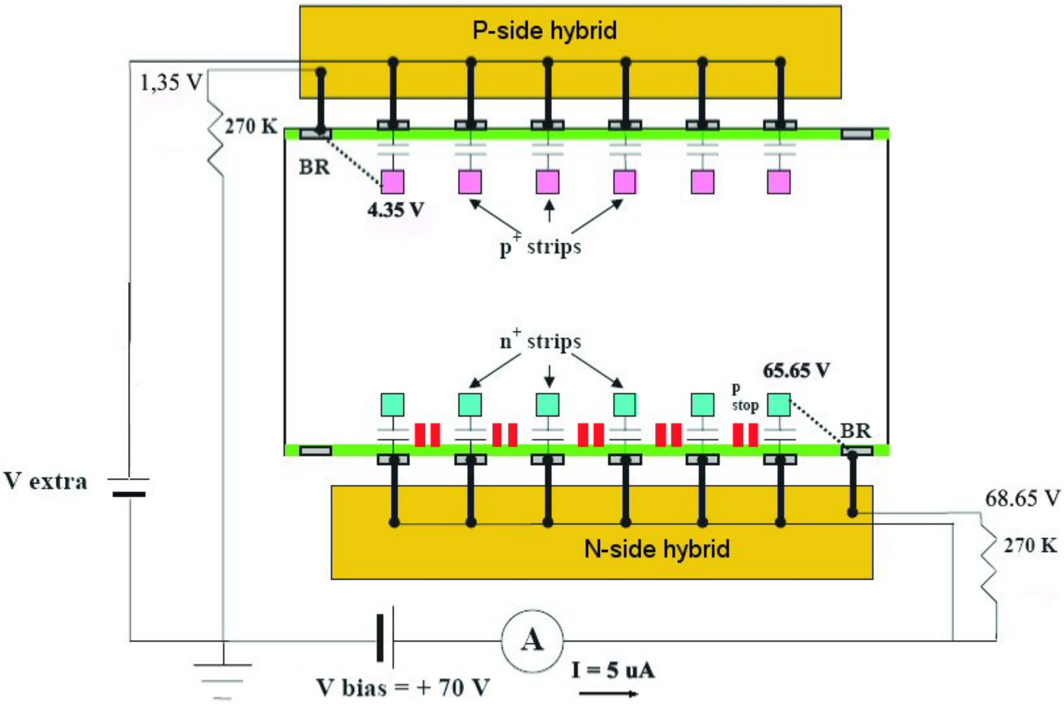

Figure 3.26: Connection scheme used for to bias problematic Sintef modules during the I-V curve measurements: thorugh an additional voltage source, it is possible to decrease the potential difference between the p-strips and the aluminum traces in order to avoid the accumulation of negative charges in the oxide. The voltage and the current values in the various points of the circuit are indicated in the scheme.

the lines devoted to the digital signals, to the supply lines and also to the serialized read-out analogue signals: only a deep analysis of the test results and an accurate visual inspection at the microscope allowed to localize the damage and to exclude any other defect in the electronics. Where possible, this type of defect was solved with the substitution of the damaged components and requested a further processing and assembly.

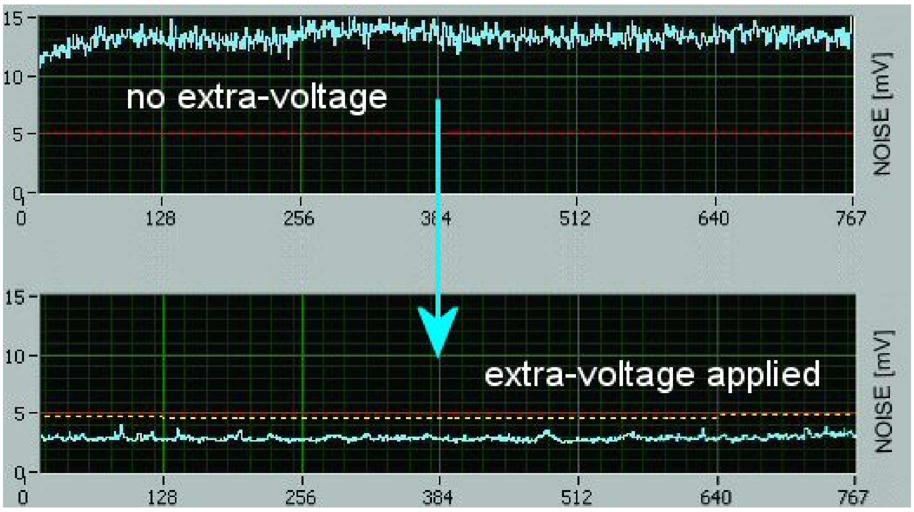

Figure 3.27: P-side noise in a Sintef module: in the top panel the noise is measured biasing the module through the standard circuit; the surface inversion shorts the p-strips increasing the noise; applying 2.5 V extra voltage to the P-side hybrid with respect to the bias ring the inversion does not take place and the noise goes back to an acceptable level (bottom panel).

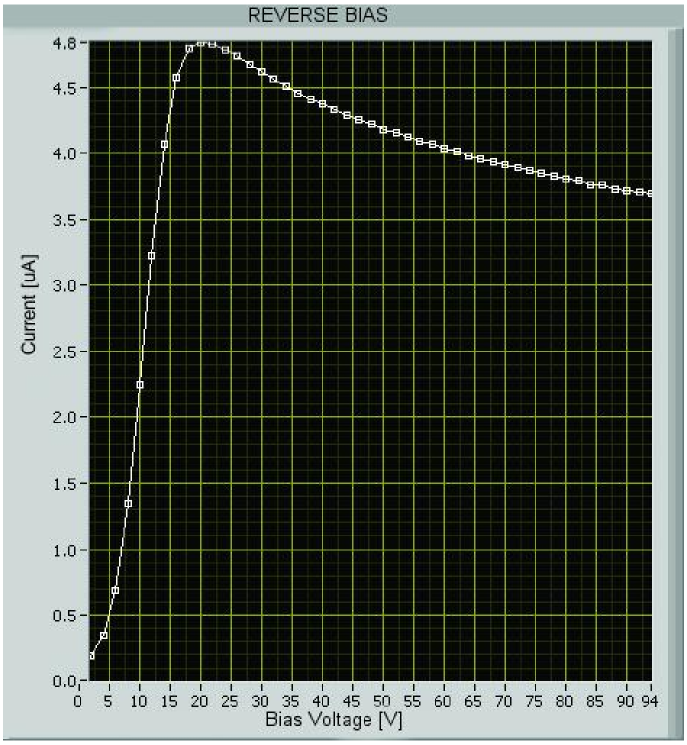

Figure 3.28: Peculiar I-V curve in a problematic Sintef module. The curve reaches the maximum value and starts to decrease with the increasing applied voltage, suggesting that the bulk inversion phenomenon has taken place, suppressing the generation current.

3.5 The SSD ladders

The produced modules, after the quality validation, have been mounted together on the carbon-fiber supports in groups of 10, 12 or 13 units, forming 144 *half-ladder*, disposed in turn to form the 72 SSD *ladders* (see fig. 3.29 and 3.30). This phase of the SSD assembly was carried out in Amsterdam (Netherlands) and Nantes (France).

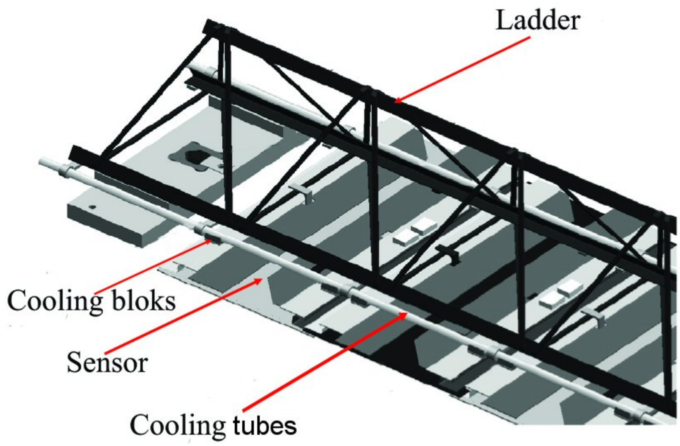

Figure 3.29: Scheme of the SSD ladder (*detail*). The *sensor* is mounted under the carbon fiber support (*ladder*); the tubes providing the cooling distribution are fixed on the module hybrids through the *cooling blocks*.

Afterwards the *ladders* were installed on carbon fiber support cones in two concentric cylinders in Utrecht (Netherlands), composing the two layers of the SSD (see fig. 3.31 and 3.32). For each layer the ladders are mounted in two slightly different radii such that their sensors partially overlap and the full azimuthal coverage is obtained. The modules are cooled by water running through two thin (40 μm wall thickness) tubes along each ladder.

The ladders are controlled and read-out through the ECMs (EndCap Modules). Each half-ladder end has an ECM which provides the interconnection between the outside world and its 10, 12 or 13 SSD-modules. Layer 5 ladders have 22 SSD modules, where 10 modules are connected to the ECM on one side and 12 modules to the ECM on the opposite side. For layer 6 (25 modules), the number of modules per side is 12 and 13 respectively. The analogue to digital conversion of the signals is performed in the Front-End ReadOut Modules (FEROM) located outside the ALICE magnet. The EndCaps and the FEROM are described in the following paragraph.

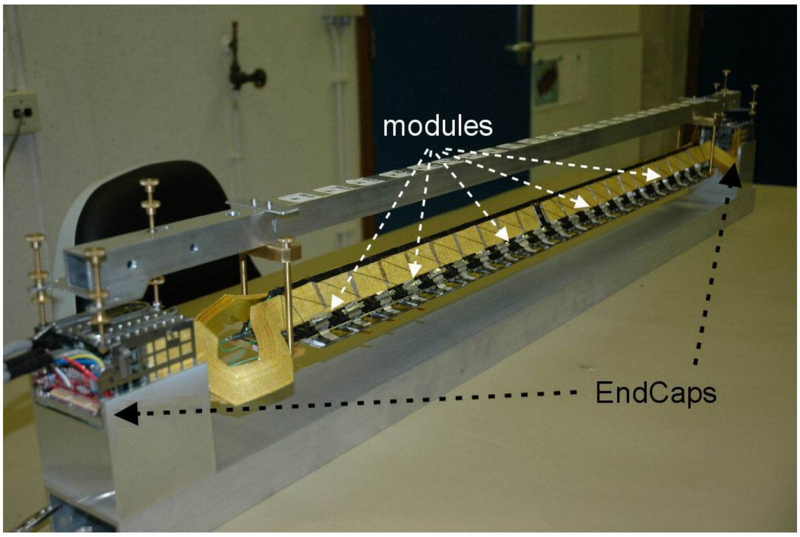

Figure 3.30: A ladder during the assembly operations. 22 modules are installed on the carbon fiber support and electrically connected to the EndCap modules placed on both sides. See the text for the description of the different components and their functions.

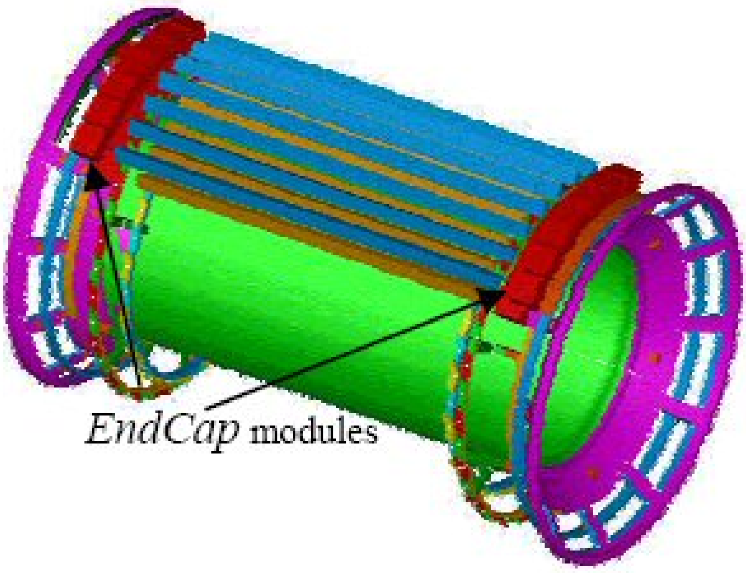

Figure 3.31: Scheme of the SSD cone. The ladders are progressively installed on the carbon fiber cones with the corresponding EndCap modules, forming the two SSD cylindrical layers.

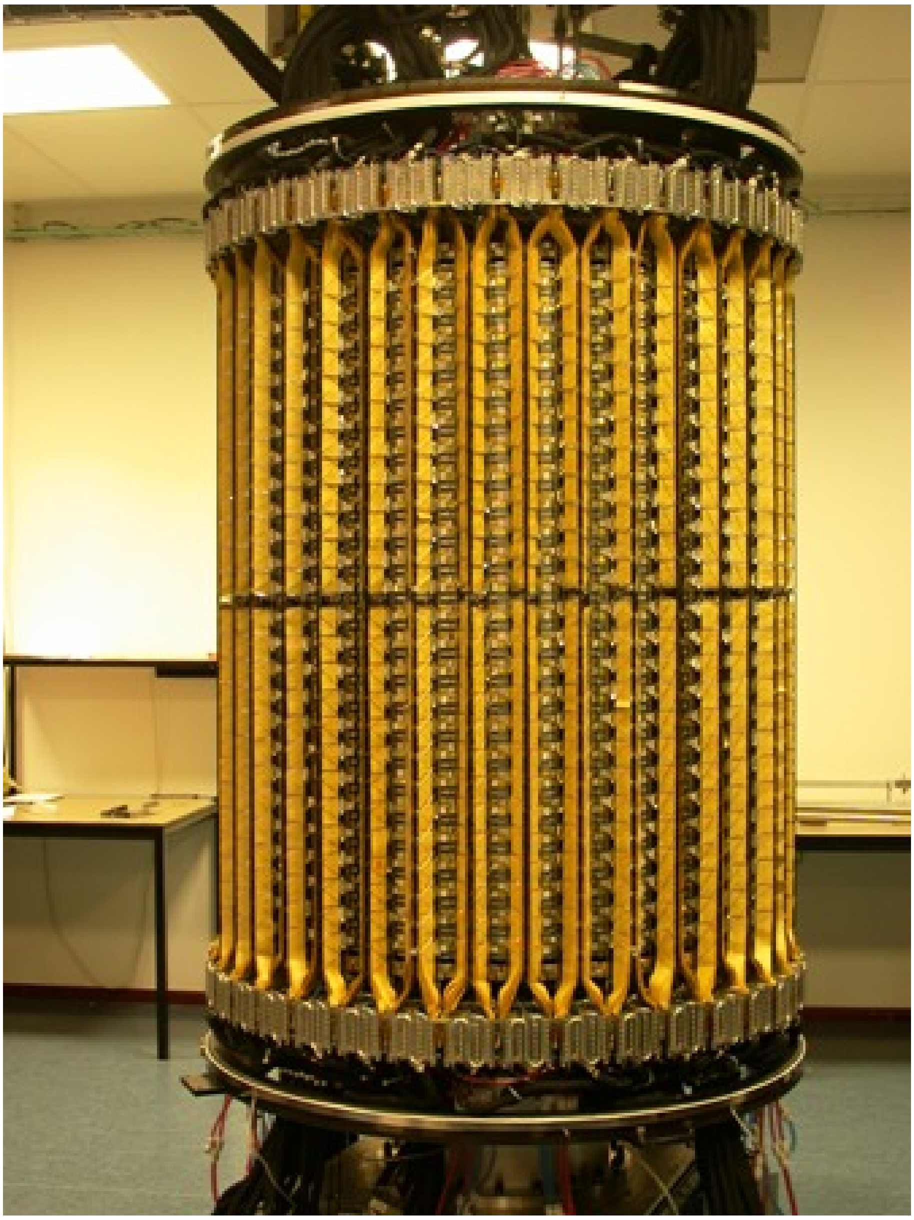

Figure 3.32: Photograph of the SSD in the final configuration, taken at the Utrecht laboratories just after the end of the assembly operations. The cables connecting the Layer 6 modules to the corresponding EndCaps are visible, while the sensors are facing the cylinder axis. The Layer 6 is built around the Layer 5 ladders.

3.5.1 Endcaps

The EndCap is the interface for and distributor of the control and data signals between the detector modules and the data acquisition, placed at a distance of 25 m away. Each EndCap module is composed out of (see fig. 3.33):

- 1 *Interface-Card*, which interfaces the module hybrids with the read-out FEROM;

- 1 to 7 *SupplyCards* (usually 7), each connected to 2 module hybrids; they manage the analogue signals and their transfer to the FEROM; in addition, they provide a measurement of the bias current and the temperature of the modules;

- a *BasePlate* or PCB, which hosts and connects together the other EndCap components;

- a *CableCard* which has all cables for the connections to the data acquisition and the control system.

.

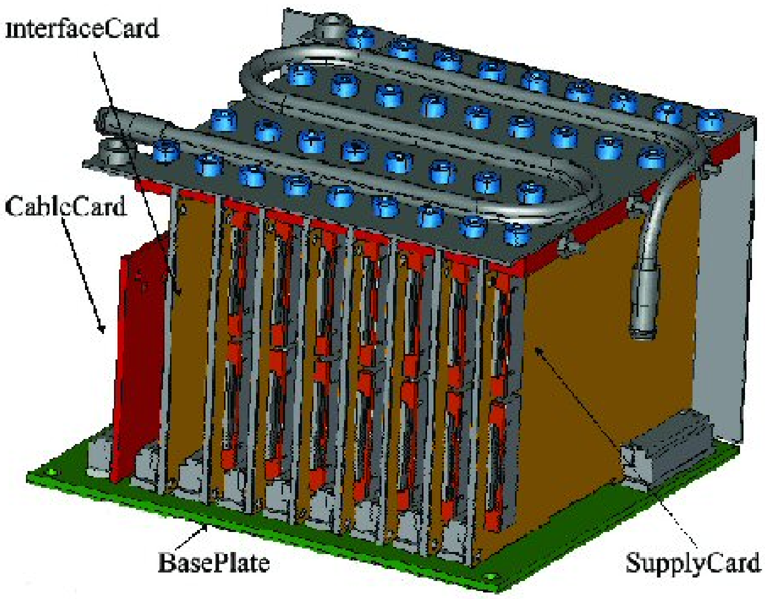

Figure 3.33: The EndCap modules. The main components are indicated in the scheme, hosted by the PCB backplane: the Interface between front-end hybrids and read-out modules, the Supply Cards managing the analogue signals and measuring the bias current and the temperature of the modules, the Cable Card connecting the EndCap with the data acquisition and the control system.

The EndCap tasks can be summarized into four main functions [45, 46]:

- **Power control and protection.** The power supplies for the detectors, for the EndCap ground level electronics and the bias level electronics are all floating supplies with sense wires up to the EndCap. The connections between the experiment ground and the floating grounds, like P-side ground and N-Side ground are made inside the EndCap. The mechanics is at experiment ground level, and forms a shield around each EndCap. In this way the analogue buffer is very close to the signals source and ground reference, and it is shielded. This approach should prevent electromagnetic interference. Taking into account the ALICE environment, the EndCap electronics are protected against malfunctions deriving from the expected 50krad total ionizing dose expected during the experiment life time. Radiation tolerant design techniques allow the devices to survive Single Event Effects (SEE), i.e. damages in the electroncis caused by single ionizing particles, and to avoid any Single Event Upset (SEU), i.e. a change of state caused in a register by ions or electro-magnetic radiation.

- **Signal buffering and coupling.** The analogue signals from the front-end are buffered. For the readout of the two detector sides an analogue multiplexer is required. These two functions are integrated in an integrated circuit, the ALABUF. Since the double-sided detectors use front-end read-out electronics operating at different potentials for the different sides, all signals are AC coupled to the corresponding voltage level to avoid the data acquisition and control electronics to operate at the front-end bias potentials.

- **Readout Control.** The HAL25 serial read-out mechanism allows the ECM to have one analog output for each SSD-module, which consists of 1536 signals, one for each strip. The ECM also has an error output signal to indicate token errors and power supply problems. To start the readout, the front-end chip requires a token and a clock signal. These signals are distributed by the ALCAPONE chips, which also controls the token delay and the analogue multiplexer, the power supply control, the status monitoring and the error handling.

- **JTAG detector control and monitoring.** The front-end electronics is controlled via the serial JTAG bus. This bus is also used to monitor and control the

EndCap functions: errors like latch-up and high detector current can be monitored, and appropriate action can then be taken; through the JTAG protocol, moreover, disabled or broken front-end chips, hybrids and EndCap PCB's can be bypassed and this information is available for the data acquisition system.

3.5.2 The FEROM modules

The read-out signals are sent by the EndCaps to the FEROM system, located in the cavern just outside the ALICE magnet. The FEROM is in charge for the digitization of the signals from each of the SSD 1698 detection modules in parallel, namely 2.6 million analogue samples per event at the trigger rate of ALICE. It is also connected to the data acquisition system, the detector control system and the central trigger processor. An overview of the SSD read-out system is schematically shown in fig. 3.34. The FEROM and its functionalities will be described more in detail in chapter 4.

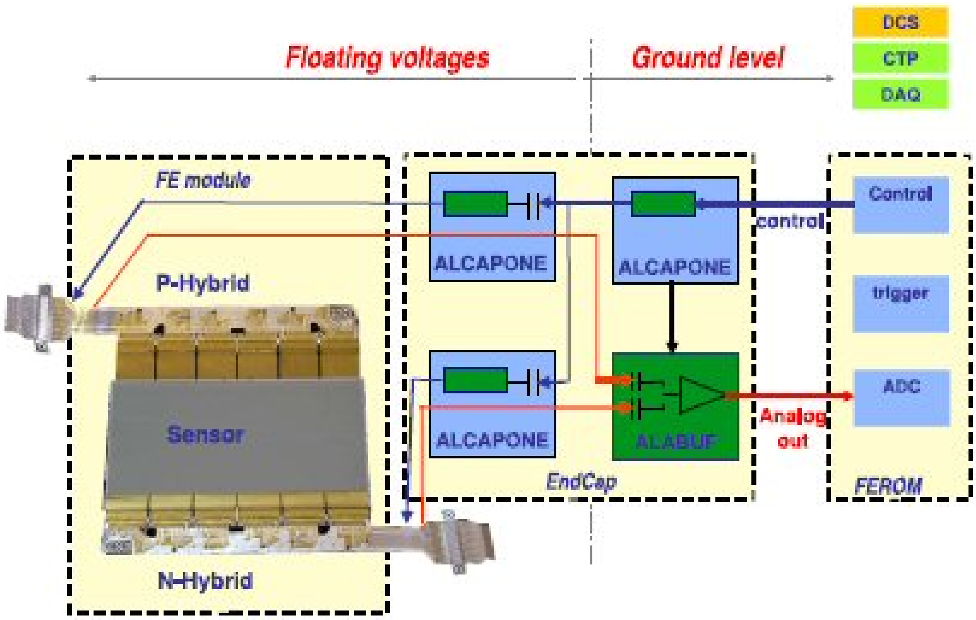

Figure 3.34: The SSD read-out scheme. Notice that the double-sided detectors and their electronics operate at floating voltage levels: the AC coupling connections between the real ground and local module P-side and N-side 'grounds' are performed by the EndCaps. The Endcap interfaces with the FEROM providing the read-out, the control and the trigger.

3.5.3 The ladder characterization

Even these stages of the SSD assembly were monitored with continuous tests in order to detect every possible damage originated during the manipulation of the devices and to spot new problems deriving from the new configuration. All the sensors mounted on a ladder, namely groups of 10, 12 or 13 units depending on which layer and side of the detector they are istalled on, are indeed biased through the same line. Therefore it's necessary to define a voltage value capable to deplete all the sensors, remaining at the same time lower than the breakdown voltage. The measured current, in this case, does not bring information about the single modules and their depletion. The evaluation of the most convenient bias voltage value is carried out scanning the whole range 0÷80 Volts and measuring at each step the noise: the voltage level allowing the insulation of the strips is determined with the same procedure followed by the test system, described in 3.3.1.

Moreover, a complete characterization of the almost 20000 channels composing each ladder was performed: pedestal, noise and common mode noise were measured at the various stages of the construction of the layers and after the transport to the ALICE location at CERN before being lifted down into the cavern and installed in the final experimental site. A system of thresholds based on the common mode subtracted noise measurements allowed to detect, classify and count the defects present on the detector at this stage. The noise as a function of the strip number is shown in the following figures, where the defective channels are highlighted by the red lines. The defects can be summarized in the following typologies:

- single channel defects:
  - Dead channels: channels presenting very low noise (σ <0.5 rms ADC units) whose front-end electronics is inactive (see an example in fig. 3.35); they cannot read-out the signals collected by the corresponding silicon strip.
  - Noisy channels: channels presenting high noise with respect to the average noise level measured in the module side they belong to; a channel is anyway classified as noisy if σ >12 rms ADC units (see fig. 3.36), in order to assure a signal-to-noise ratio S/N $\gtrsim$ 10 for MIP signals (1 MIP $\gtrsim$ 120 ADC units).

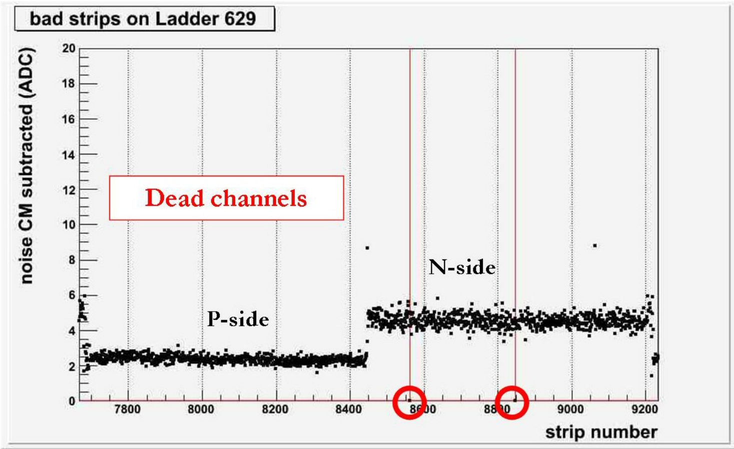

Figure 3.35: The noise is plotted as a function of the channel number, for a module belonging to the Ladder 629. Two N-side channels with $\sigma \sim 0$ rms ADC units are tagged as *dead channels*.

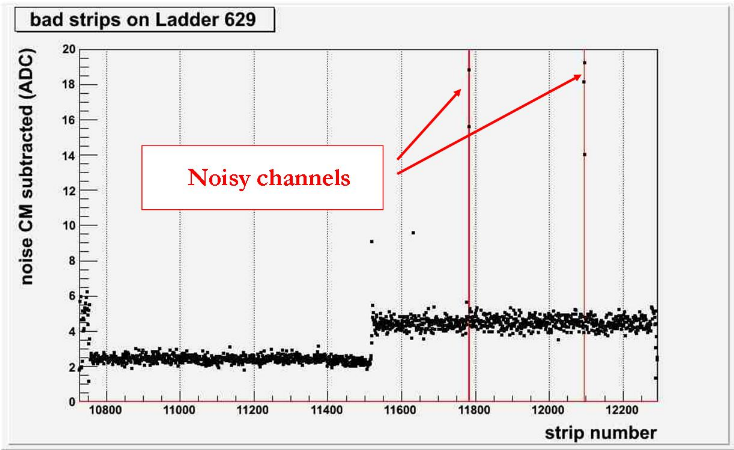

Figure 3.36: Noise vs. channel number for another module installed on the Ladder 629. Several channels presenting $\sigma > 12$ rms ADC units are tagged as *noisy*.

- module or half-module defects:
  - Damaged front-end electronics: a whole hybrid is inactive, showing a noise $\sigma \lesssim 1$ rms ADC unit (again 3.37, right red-filled zone); signals collected on these module sides cannot be read-out.
  - Undepleted sensor: both module sides, or at least their central regions, appear very noisy (see the left red-filled zone in fig. 3.38); an unsuitable bias voltage is applied to the sensor.
  - Sintef problem: P-side noise higher than normal and increasing with time; the detector uses a SINTEF sensor and showed the same problem in the

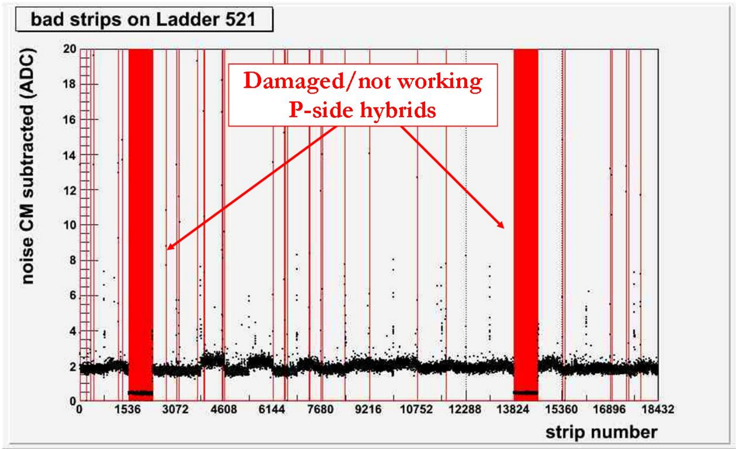

Figure 3.37: For the whole Ladder 502 the noise is plotted as a function of the channel number. The red-filled areas correspond to module sides whose electronic is inactive: they present low noise and cannot read-out any physical signal.

laboratory tests.

- half-ladder defects:
  - High bias current on a half-ladder: the half ladder can not be operated since it shows a very high bias current even applying a few volts; the voltage drops through the bias resistor avoiding the sensor depletion does not allow the sensor to deplete. After electrical tests on the components, this defect turned out to be caused to a short in the electronics power lines; its repair appears difficult since it should be located inside the SSD cone already installed.

The defects detected by this extensive analysis were then counted and classified before the final installation of the detector in the experimental site. They are summarized in table 3.2. The results certified the global quality of the SSD: the detector finally presents only 2% defective channels out of about 2.6 million SSD channels.

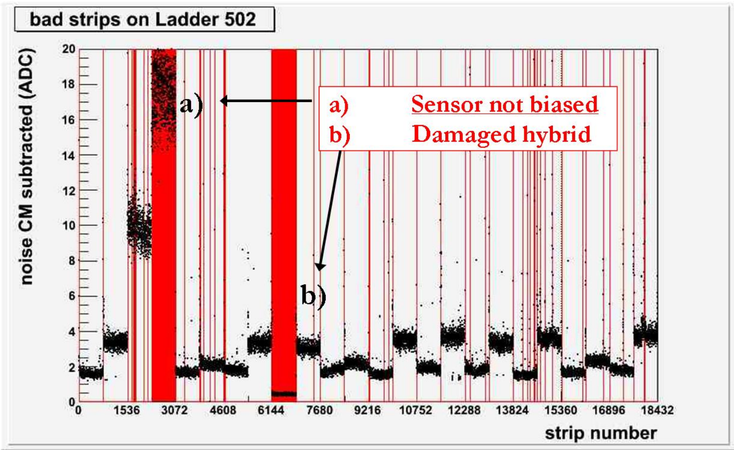

Figure 3.38: The noise of Ladder 521 is plotted as a function of the channel number. The *a)* red area spots an undepleted sensor: all the channels belonging to that module present a high noise level. The *b)* red area indicates a hybrid whose electronic is inactive: its channels present low noise and cannot read-out any physical signal.

Sector	# bad modules	% bad channels
Layer5 C-Side	5	1.20%
Layer5 A-Side	12	2.03%
Layer6 C-Side	4	0.87%
Layer6 A-Side	6	3.79%
SSD	27	**2.01%**

Table 3.2: Percentage of defective channels out of the total number of channels belonging to the considered SSD sector. The last line resumes the overall defects percentage with respect to the ∼2.6 million channels of the SSD. Each layer is divided into two sectors: the C-side, towards the Muon Arm side, and the A-side, on the opposite side. The two sectors have different numbers of channels, thus they weigh differently in the computation of the total percentage of defects.

3.6 The SSD commissioning phase

After a complete test of the 144 half-ladders composing the SSD and the integration with the Silicon Drift Detector, during the fall of 2007 the detector was lift down in the ALICE cavern and installed inside the TPC in the final experimental site (see fig. 3.39). Each ladder was connected via approximately 40 m long twisted pair

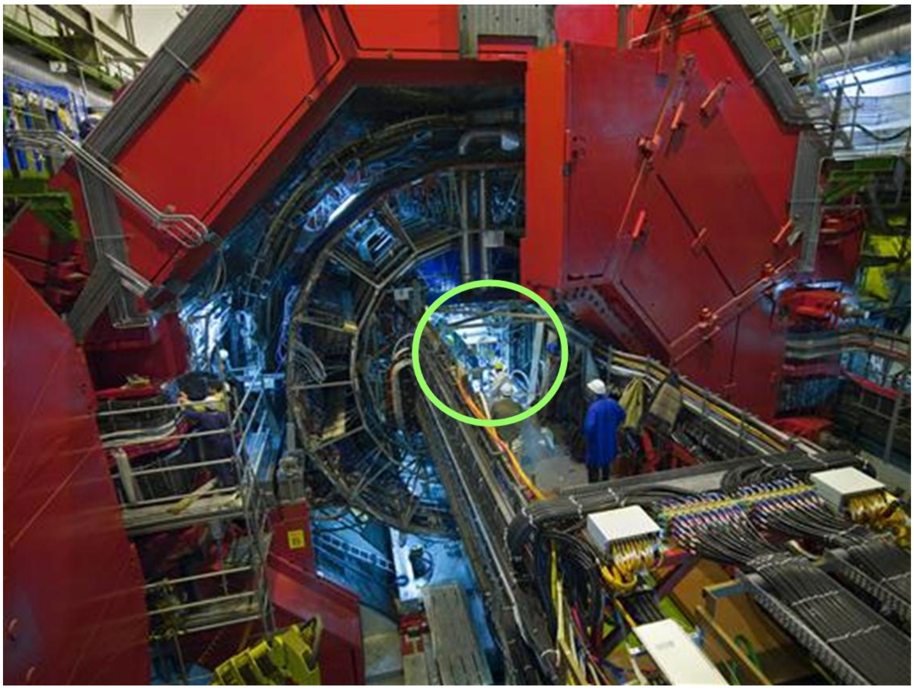

Figure 3.39: The SSD installation inside the L3 magnet, down in the ALICE cavern.

cables to the power supplies and to the FEROM modules, which provide in turn the connection with the system Data AcQuisition system (DAQ), the Detector Control System (DCS) and the Trigger System .

During this preliminary phase, the corresponding functionalities of each ladder were individually verified with the locally controlled test system. Once connected and tested the cooling system, the SSD was globally powered and controlled as a part of the ALICE apparatus for the first time. The ALICE experiment is controlled by several independent 'on-line systems'. Each system carries out different types of operations belonging to a different domain of activities: Detector Control System (DCS), Data Acquisition (DAQ), Trigger system (TRG) and High-Level Trigger (HLT). These systems are independent, may interact with all the single particle detectors and allow groups of them to operate concurrently, within the so-called *partitions* of detectors. In the final setup the detectors will work all together to collect physics data.

In the commissioning phase, however, detectors can run as independent objects for testing and debugging purpose. While this mode, called 'standalone mode', is absolutely vital in the commissioning and testing phase, it will also be required during the data-taking phase to perform calibration procedures on individual detectors. It will therefore remain essential during the whole life of ALICE.

The functionalities of the detector are mainly controlled by the Detector Control System; responsible for the control and the integration of all the ALICE subdetectors in a single framework, the DCS provides a constant and complete monitoring of the status of the SSD ladders, for what concerns the sensor bias HV and the electronics LV power supplies, the sensor bias current and the temperature of the modules [47]. The screenshot in fig. 3.40 gives an example of the on-line overview of the detector conditions, as captured during one of the commissioning tests: each triangle represents a half-ladder; the different colors indicate the operating status of the corresponding power supplies and of the front-end electronics.

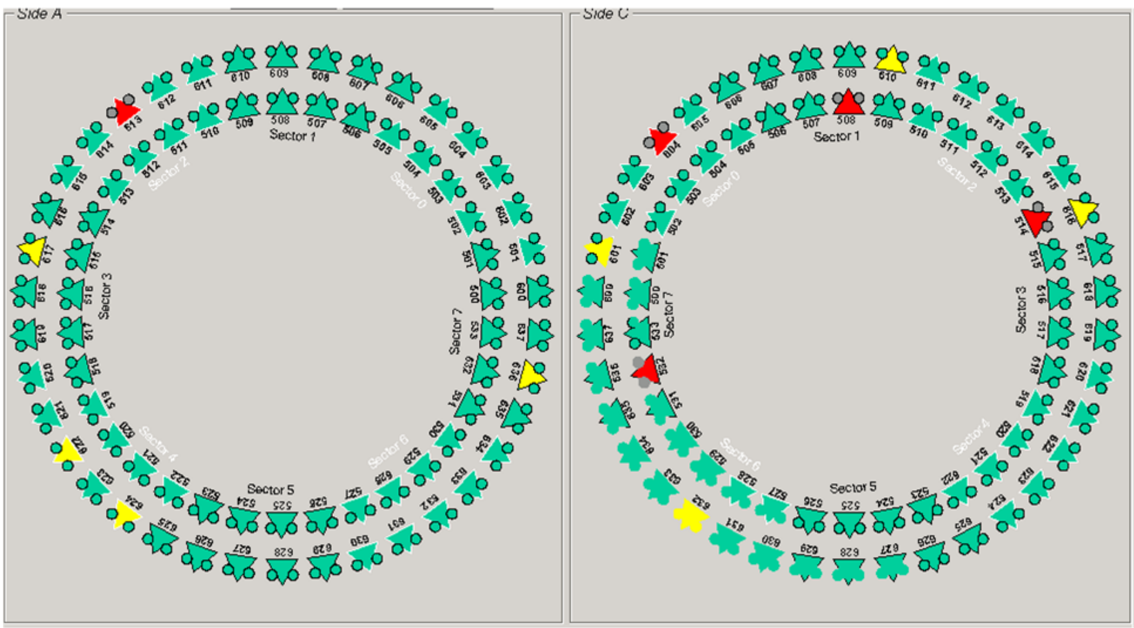

Figure 3.40: The DCS software output page showing the status of HV, LV and current of the SSD ladders. The triangles indicate the ladder bias voltage status, the side circles refer to the electronics.

3.6.1 ***Stand-alone*** **runs and** ***global*** **runs**

The integration of the SSD detector with the mentioned control systems was tested through a large set of acquisition runs during the 2008 commissioning sessions. The SSD acquired data both as a stand-alone detector and as a part of a more complex *partition* of sub-detectors remotely controlled. The work was mainly devoted on one side to optimize the operating parameters, to test, to debug and to calibrate the detector, on the other side to check the compatibility of its operations with the rest of ALICE. The SSD can operate three different configurations, corresponding to three run categories, i.e. the *stand-alone run*, the *pedestal run* and the *global run*:

- The *stand-alone runs* are used for debug, test and calibration purposes: the sub-detector functionality and acquisition control, released by the ALICE global control, is taken by the SSD operator; a set of data is acquired by the desired SSD portion with an adjustable trigger rate. The data are corrected for the *pedestal* and the *common mode oscillations*; then they are *zero-suppressed*. The acquired data can be on-line monitored through the dedicated frameworks, both interactively with the MOOD (Monitor Of Online Data, [48]) and automatically with the AMORE (Automatic MOnitoRing Environment, [49]). Among the various aspects of the acquisition studied in this phase, a deep investigation was in particular carried out by taking data in *stand-alone* mode:

    - at the default rate (40Hz) to test the synchronization between the read-out operations and the signal digitization;
    - at different trigger rates to test the general behaviour of the systems and in particular the noise behaviour;
    - at the default rate as a benchmark to check the output data quality of the *pedestal runs*.

- The *pedestal run* is a particular kind of stand-alone run used to acquire not filtered data and calculate for each SSD channel the pedestal, the noise and the thresholds for the zero-suppression; it also spots the not properly working channels: the *offset correction* and the *zero suppression* are in this case disabled; the acquired sample of a few hundreds of events is processed by a specific algorithm (the *Detector Algorithm*, DA) in order to calculate the pedestal and the noise of each single SSD channel; the algorithm produces the formatted calibration data for the FEROM system, used for the hardware zero suppression, and for the off-line reconstruction and analysis. A *bad channel list* including the problematic channels is generated and stored on the calibration database.

- The ALICE *global runs* can include the SSD in a *partition* with a set of other sub-detectors under the central ALICE control and are aimed at testing the global operating procedures and at acquiring particle data. In the entire commissioning phase, the SSD took part in a large set of global data acquisition runs, resulting as one of the most stable sub-detector of the ALICE apparatus: during the last 6 months of the *2008 Commissioning Run*, i.e. from May '08 to October '08, it collected about 10^8 *events* during 1400 *runs* for a total acquisition time of almost 1000 *h*. The statistics regarding runs, duration and collected events for the SSD and the other ALICE sub-detector is shown in fig. 3.41.

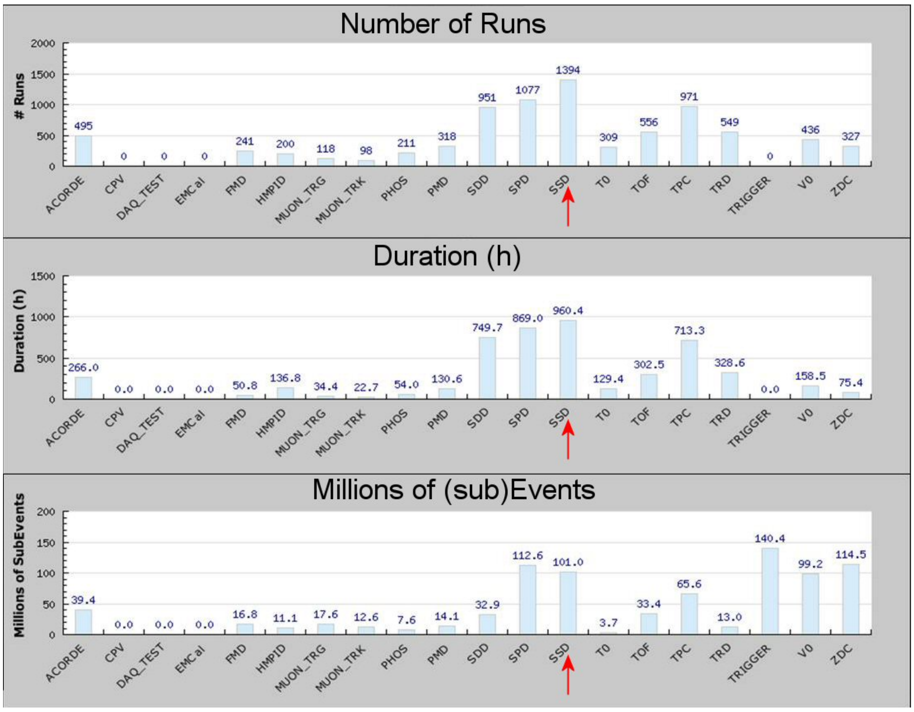

Figure 3.41: Statistics regarding runs, duration and collected events for the SSD and the other ALICE sub-detector, during the last six months of the *2008 Commissioning Run*. The SSD results as one of the most stable sub-detector.

The data have been reconstructed within *AliRoot*, the ALICE off-line framework. This software, as will be described in detail in chapter 4, contains the simulation of the response of the SSD detector, the corresponding algorithms developed for the local reconstruction and the tools to analyze the SSD data. The output of the reconstruction concerning two different acquisition configurations is shown and discussed in the following paragraphs.

3.6.2 Noise tests

During the commissioning, some runs have been periodically devoted to a fixed frequency triggered acquisition: this conditions give the opportunity to evaluate the influence of the noise on the local SSD reconstruction. The signals acquired with fixed frequency trigger are generally not generated by any hitting particle but consist only in random oscillations of the read-out channel inputs.

As it will be discussed more in detail in section 5.3.2, on the basis of the pedestal and noise measurements performed during the pedestal runs, a threshold is calculated and applied to each SSD channel in order to zero suppress the data at hardware level. In addition, the reconstruction exploits the double-sided nature of the SSD modules to reject noise signals: it requires the charge and the position of the hits detected on opposite sides to match, in order to assure the passage of a particle. If these conditions are satisfied, an SSD point is reconstructed. In absence of particles, the SSD reconstructed points are therefore *fake hits*.

The number of fake hits per event has been estimated during the noise run acquisition at the default trigger rate of 40Hz. Hereafter the results of the corresponding data reconstruction are shown: the rate of reconstructed hits per module is plotted in fig. 3.42, respectively for Layer 5 on the *left* side and for Layer 6 on the *right* side.

In addition, the dependence of the number of fake points on the trigger frequencies has been investigated taking noise data at 400Hz and 4kHz, keeping the same SSD settings and calibration as in the previously considered. The results of the reconstruction are summarized in table 3.3. At 4MHz trigger frequency, the number of fake points is sensibly larger; further investigations indicate that the worsening appears to be related to a subset of channel not properly working at such rates that can be zero suppressed.

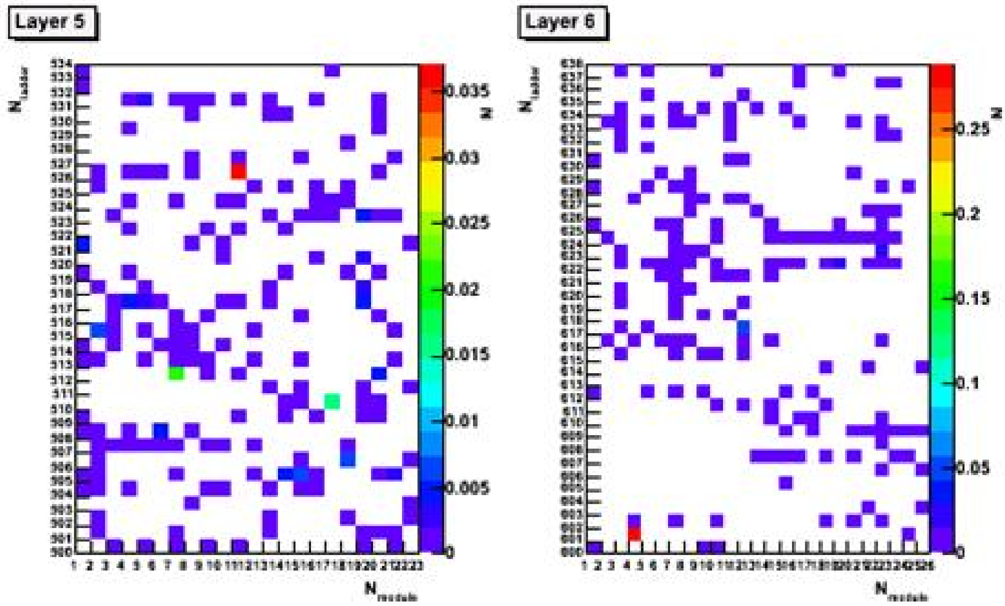

Figure 3.42: Noise run acquisition: rate of reconstructed hits per module, for Layer 5 (*left*) and for Layer 6(*right*).

Run number	Trigger frequency	# of events	hits on Layer 5		hits on Layer 6	
			tot. #	per event	tot. #	per event
55633	40 Hz	1177	283	0.24	637	0.54
55634	400 Hz	3317	756	0.23	1728	0.52
55635	4000 Hz	1800	10252	5.70	2381	1.32

Table 3.3: Rate of reconstructed hits during three noise runs taken at different trigger frequencies. The number of fake points sensibly increases at 4kHz.

3.6.3 Cosmic rays acquisition

The acquisition of cosmic rays data with the ALICE detector provided firstly a test for the global operating procedures. In addition, the collected particle data gave the opportunity to carry out the first studies on various aspects of the ALICE experimental activity like the detector alignment, the efficiency of the off-line data reconstruction and the effects of the magnetic field on it.

As an example, the results of the local SSD reconstruction of the data acquired in one of the last cosmic rays acquisition taken in September '08 are shown in the following figures. In fig. 3.43, on the left, the hits distribution per module spots the regions of the SSD Layer 5 mainly interested by the cosmic rays interaction, namely the top and the bottom sectors of the barrel, since the cosmic acquisition is triggered by the ACORDE modules (see 2.8), placed on top of the L3 magnet. The module position within a ladder is plotted on the x-axis, while the ladder number on the y-axis. The right panel shows the cluster size correlation through a density plot, indicating on the x- and y-axis the number of channels fired on a module on the P- and N-side respectively, during a cosmic ray interaction; it can be used as a further indication on the particle angle of incidence on the detector.

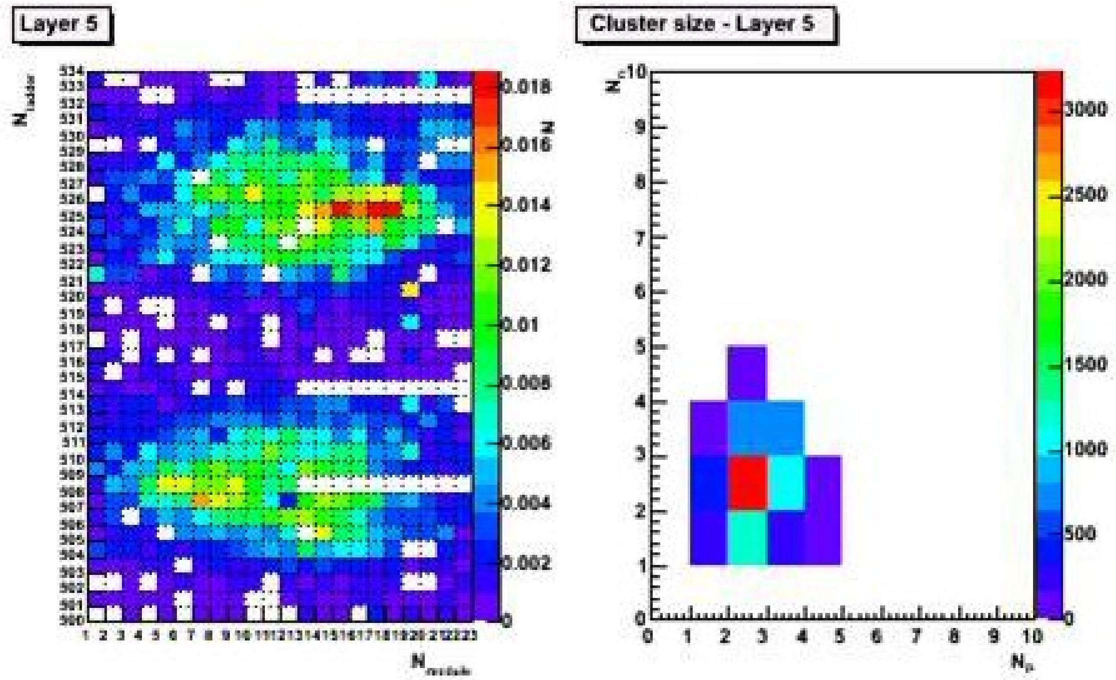

Figure 3.43: Cosmic run reconstruction: the hits distribution per module is shown on the left; on the right, the cluster size correlation.

Starting from the informations about the position and the collected charge of the hits detected on both sides of an SSD module, the reconstruction framework computes the total charge deposited in the sensor by the cosmic ray. In fig. 3.44, the left panel shows the reconstructed hit charge distribution for the hits detected on Layer 5; the P- and N-side charge correlation is plotted in the right panel.

The off-line analysis, through the tracking procedure, provides then to associate the SSD reconstructed points with the hits detected by the rest of the tracker, reconstructing the trajectory of the cosmic rays traversing ALICE. The good compatibility of the SSD points in the tracking procedure gives a further confirmation of the

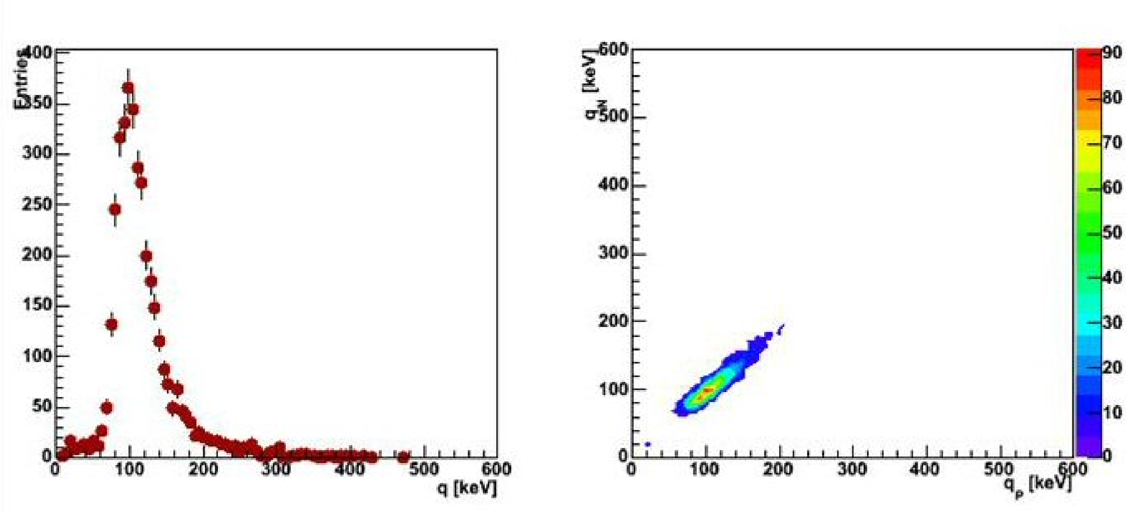

Figure 3.44: The left panel shows the reconstructed hit charge distribution for the hits detected on Layer 5. The P- and N-side charge correlation is plotted in the right panel.

SSD data reliability. One of the first cosmic ray traces reconstructed by the off-line analysis is displayed in fig. 3.45, as shown by the emphAliRoot event displayer.

For what concerns the work presented in this thesis, the cosmic rays data collected during the commissioning phase were in particular used to test the SSD local reconstruction algorithms. A detailed description of the reconstruction framework, the algorithms and the activities carried out to develop and improve them are described in detail in 4.4.1. On of the most relevant aspects of the acquisition influencing the quality of the collected data, namely the hardware correction of the *common mode* signal oscillations, is instead profusely treated in the next chapter.

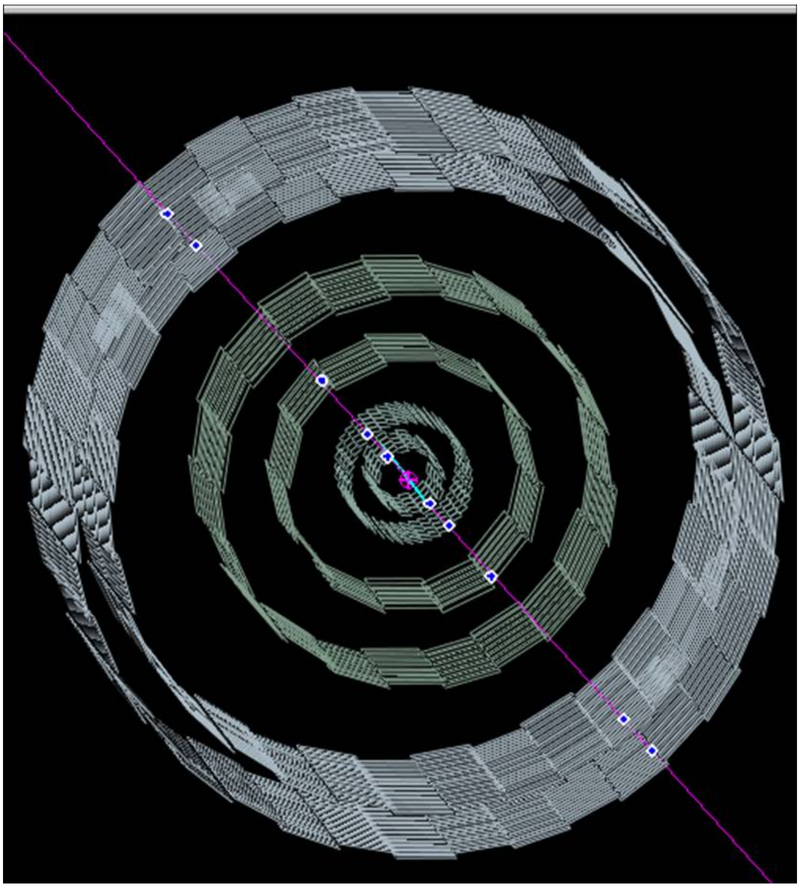

Figure 3.45: One of the first cosmic ray traces reconstructed by the off-line analysis from the whole ITS data as shown by the emphAliRoot event displayer. The reconstructed trajectory matches six ITS points.

Chapter 4

Algorithms for the common mode noise subtraction.

The common mode oscillation is one of the most important sources of the noise affecting the silicon strip detectors. Thanks to the particular nature of its effect, the contribution to the acquired data can be subtracted, allowing an efficient discrimination of the particle signals. Moreover, in a detector with such a large number of read-out channels like the ALICE Silicon Strip Detector, the huge amount of data produced in each event needs to be reduced during the acquisition phase: this fact implies a common mode correction performed by an efficient and simple algorithm implemented in the read-out electronics.

A description of the currently implemented algorithm is presented in this chapter; its performances are analyzed under various acquisition conditions.The proposals of two new algorithms are successively presented, discussing their features and their efficiency in presence of particle signals.

4.1 The Front End Read Out Module *FEROM*.

The 2.6 million channels of the SSD produce a total amount of data of $\sim 10MB/event$. The requirements of the ALICE Data Acquisition System force to strongly reduce this large quantity: the constraint limiting the data rate are mainly the bandwidth of the link from the ADC modules to the DAQ and the computing and storage resources needed to manage the data; moreover, the expected particle signal occupancy for the most central events in Pb-Pb collisions is below 3% [28].

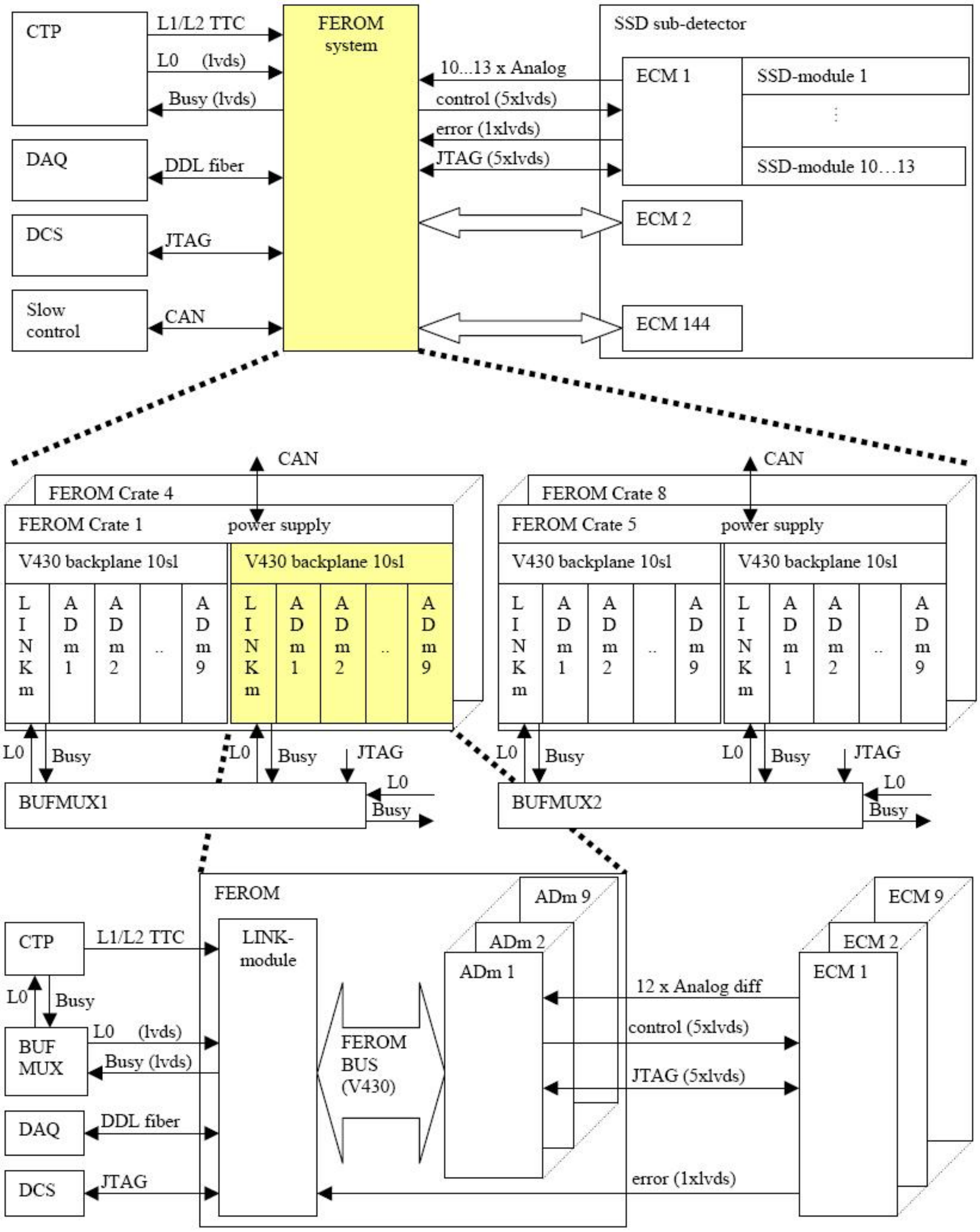

Figure 4.1: The embedding of the FEROM between the ALICE data acquisition and control system (left) and the SSD detector system (right) is shown in the top part of this figure. The central part shows the configuration of 8 FEROM crates, each equipped with AD modules and LINK modules. The bottom section shows the internal communication between the 9 AD modules and the single LINK module in each crate.

Thus the $\lesssim 3\%$ interesting data should be selected at the hardware level while the rest, likely generated by the noise, should be suppressed. These operations are performed by the *FEROMs*, i.e. the Front End Read Out Modules, that receive the analogue data from the detector electronics [50]. The main FEROM task is the digitization of the 2.6 million SSD strip values in 160 μs. This is achieved by digitizing in parallel the 1698 double-sided SSD module signals (each containing 1536 strip values). The FEROM also performs the offset correction (pedestal) and the zero-suppression, the event-data sorting using Multiple Event Buffers and the event data transfer to the DAQ.

The FEROM system consists of 8 crates, each containing 216 analogue-to-digital converters and the interfaces connected to the data acquisition system, the detector control system and the central trigger processor. The scheme in fig. 4.1 describes the complete acquisition chain, with the FEROM modules connecting the front-end electronics with the data acquisition system. The digitized data are corrected for pedestals and zero-suppressed for each event individually; the remaining data are stored in a buffer and sent to the data acquisition system. In order to properly correct the data, i.e. achieving the occupancy reduction without losing interesting physical signals, the FEROM applies an additional algorithm to suppress the base-line distortions. These distortions are mainly generated by the so-called *common mode noise* that is discussed in the next paragraph. The FPGA based design allows easy upgrading of the algorithm for the correction of this particular effect.

4.2 The common mode noise.

Besides the noise sources intrinsically related to the sensor and to the front-end electronics, the oscillation at a channel input can be enhanced by environmental origins, like by the pick-up effect of the sensor and by the instability of the reference grounds induced by the power supplies; this component of the oscillation is called *common mode* shift. While the intrinsic noise is characteristic of the single channel and the event-by-event oscillation of its output does not depend on the other channels, the common mode noise influences coherently a group of neighboring channels. Due to this fact, it's possible to estimate the common mode component in each event and correct it.

Normally, it is *common* to the smallest group of channels read by the same front-end chip, even if sometimes some substructures can appear in its distribution. In the ALICE SSD case, the common mode noise causes a coherent mostly Gaussian distributed oscillation of the baseline of the pedestals of 128 channels read by the same HAL25 chip. In the following paragraph the sources of this noise component are discussed.

4.2.1 Sources of common mode noise.

The common mode noise can be originated both from internal and external electromagnetic sources. It derives from ground loops in the power supplies used for the detector and the ADC; another contribution comes from the silicon strips and the cable lines acting like antennas in a radio frequency field. As experienced analyzing the noise data, the common mode noise is the sum of different oscillations with different amplitudes and frequencies.

An extensive optimization work was led in order to minimize the contribution introduced by the power supplies specifically developed by CAEN for the ALICE SSD. The optimization of the electronic components and of the electrical characteristics allowed to reduce the common mode σ down to 5 ADC rms units.

In the experimental site, the environmental conditions make the common mode noise grow up to a typical value of 7 ADC rms units, as it has been measured during a large number of noise runs involving all the sub-detectors. This is probably due to the presence of many active electronic devices close to the SSD modules and to the induced antenna-effect.

In fig. 4.2, the typical noise as measured on an SSD module installed in the experimental site: the plots show the total noise (*left panel*), the intrinsic noise calculated after the common mode subtraction (*central panel*), and the common mode noise for all the channels of the module (*right panel*) as a function of the strip number.

4.3 The Common Mode correction.

4.3.1 The common mode shift calculation.

In high energy physics experiments, various methods have been applied to correct the common mode noise contribution to the signals read by a group of neighboring

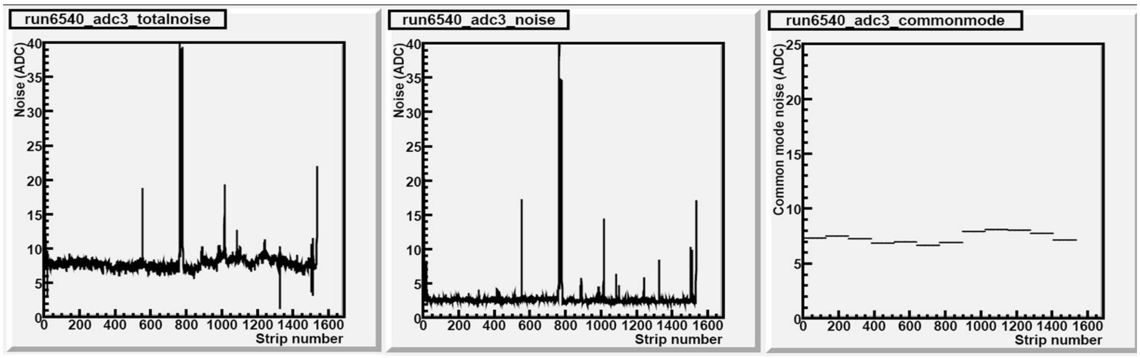

Figure 4.2: The noise affecting an SSD module in the final location. The various component of the noise measured on the 1536 channels of an SSD module are showed in the plots: the total noise (left), the common mode corrected noise (center) and the common mode noise (right). All the channels belonging to the same chip are characterized by the same common mode noise; it oscillates from chip to chip around the value of 7 rms units.

channels of a detector. Since it is a coherent displacement of the pedestals of all the channels belonging to the same chip, this baseline shift can be calculated averaging the signal amplitude of the 128 channels of a chip. Hereafter the simplest definitions of the pedestal, the noise and the common mode shift are briefly summarized.

Pedestal, noise and common mode determination.

The *pedestal* represents the read-out value of a channel in absence of both particle signals and noise. Normally it doesn't correspond to the origin of the ADC scale and can vary from channel to channel. It is mainly related to the presence of a DC offset at the output of the read-out chips and it has to be subtracted to properly evaluate the signal amplitude. In order to compute the pedestal and the noise for the i-th channel, a sample of M read-out data without particle signals at the input is needed. The pedestal is a simple mean of the digitized data:

$$P_i = \frac{1}{M} \sum_{j=1}^{M} ADC_{ij} \tag{4.1}$$

where ADC_{ij} represents the j-th read-out value of the i-th channels. The read-out data have gaussian distribution with standard deviation:

$$R_i^{tot} = \sqrt{\frac{1}{M-1} \sum_{j=1}^{M} (ADC_{ij} - P_i)^2} \tag{4.2}$$

that is the i-th channels total noise.

The simplest common mode calculation algorithm is described by the equation 4.3

$$CM_{(l)j} = \frac{1}{N_{spy(l)}} \sum_{i_{spy(l)}=1}^{N_{spy(l)}} (ADC_{i_{spy(l)}j} - P_{i_{spy(l)}}) \tag{4.3}$$

where:

- $CM_{(l)j}$ is the *common mode* of the l-th chip in the j-th event
- $N_{spy(l)}$ is the total number of spy channel (i.e. the channels considered in the calculation) of the l-th chip
- $ADC_{i_{spy(l)}j}$ and $P_{i_{spy(l)}}$ are respectively the j-th read-out value and the pedestal of the i-th spy channel belonging to the l-th chip.

This basic algorithm is very efficient when applied to data in absence of particle signals and to channels showing a homogeneous gaussian intrinsic noise σ.

Channels presenting high pulses due to an abnormal noise fluctuation or to a particle detection, can indeed introduce a significant error in the comon mode calculation. Thus, the simple average is not safe when applied to physics event acquisition runs.

4.3.2 Benchmark algorithm for the CM correction

In order to test the performances of the common mode corrections algorithms presented in this chapter, a benchmark algorithm has been designed: all the common mode calculations presented in the this chapter are compared with the results obtained with this *BestCM* algorithm.

Supposing not to have time and computing resources limitations, contrary to the real case, this algorithm analyzes the same data more than once, applies selections and calculate averages and standard deviations. Due to the complexity of the operations performed, these calculation are in fact not allowed in the acquisition hardware, but give a result that aims at being considered a good approximation of the real common mode shift.

The *BestCM* algorithm acts in two steps over the signals collected in an event by the 128 channels of a chip. The channels corresponding to the first and to the last 16 strips of the SSD module are excluded from the calculations, because of their different behaviour in terms of common mode noise, as will be explained in the

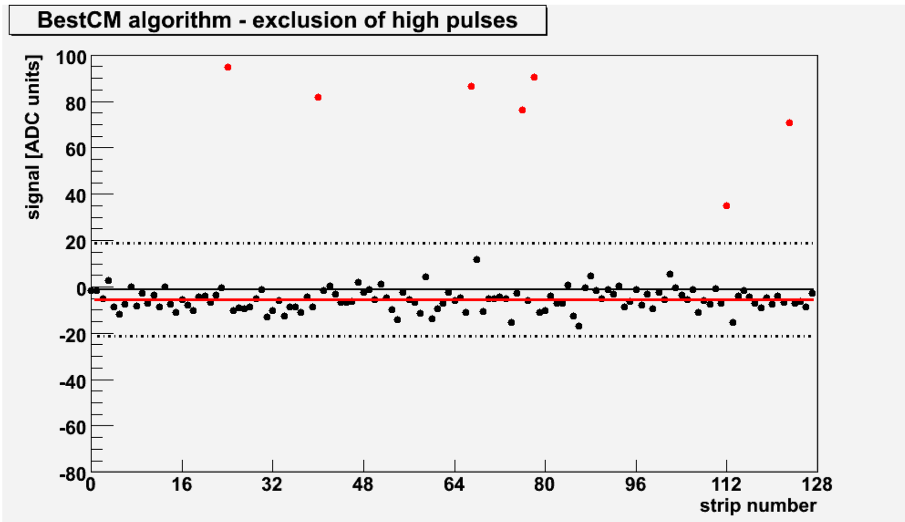

Figure 4.3: The plot reports the signals measured by the 128 channels of a chip. A first average of all the 128 read values gives the mean shown by the black solid line. The RMS of their distribution is used to define a range centered on this mean and extending between the dotted lines. The points falling outside this range (red points) are excluded and the mean of the remaining signals is successively calculated (red line). The resulting value defines the *BestCM* common mode shift.

following paragraph. In the first step the algorithm calculates the average and the σ of the signals distribution. The channels presenting a signal far from the average by more than 2σ are rejected and not used in any further calculation.

In this way, in the second step, strips hit by a particle or channels presenting a large oscillation due to noise are excluded. The unrejected signals are averaged again: the result is the *'true'* common mode correction (*BestCM*). The procedure is visualized by the scheme in fig. 4.3 for a central chip of a module.

These operations guarantee the independence of the result from unexpected single channels noise oscillations and from particle signals, even in case of high occupancy of the chip.

4.3.3 CM correction for the first and last strips.

Analyzing in detail the common mode oscillations, a particular behaviour has been noticed on the first and the last strips of each module side. These strips differ from the central strips for geometrical and electric characteristics: due to their position in the sensor, they are coupled to a capacitive network which is different with respect to the central strips; moreover, they partially face a region of the sensor backplane that is not connected to the front-end electronics and that therefore presents different properties; some of these strips are also shorter because of their inclination with respect to the module edge. The sum of these factors induces on the corresponding channels a different response to the common mode noise.

The correlation between the single channel readout with the common mode shift decreases moving toward the edges of the module, as clearly visible in fig. 4.4: for each of the first 12 strips of a module P-side, the signal read in 500 events is plotted as a function of the calculated common mode (*BestCM*) in such events. Therefore these channels should not be taken into account by a proper common mode calculation with the same weight of the central strips. The possibility to correct

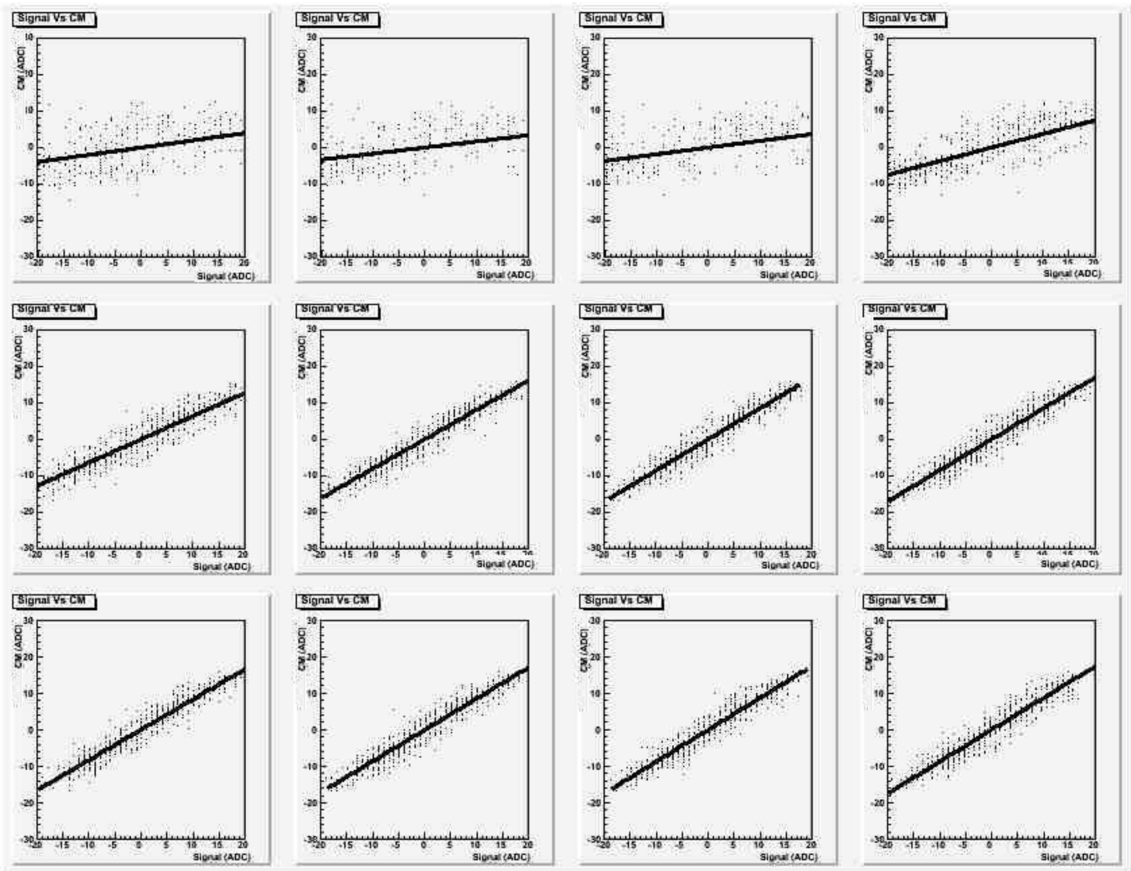

Figure 4.4: The correlation between the common mode shift and the signal measured by the single channel, plotted for the first 12 channels of an SSD module. The correlation increases while moving toward the central strips.

properly the common mode shift in the first and last channels was explored. Since the common mode correction is aimed at the reduction of the read-out oscillations, i.e. of the noise, the dependence between the common mode subtracted noise and the correction applied in each event was studied for each channel.

The most efficient method to estimate the right correction turned out to be the minimization of the noise as a function of the readout signal, the *BestCM* and a scale factor between the common mode and the read-out signals of each channel. Supposing the common mode to have normal distribution with $\mu = 0$, the noise after the common mode correction for the i-th channel can be expressed by the equation 4.4:

$$R_i = \sqrt{\sum_{j=1}^{M} \frac{(ADC_{ij} - \alpha_i \cdot CM_{(l)j} - P_i)^2}{M-1}} \tag{4.4}$$

where

- R_i is the common mode corrected noise for the i-th channel
- ADC_{ij} is the j-th value read-out by the i-th channel
- $CM_{(l)j}$ is the *common mode* of the l-th chip in the j-th event
- P_i is the i-th channel pedestal
- α_i is the scale factor.

The common mode value has to be multiplied for this α coefficient, which is plotted as a function of the strip number of a module in fig. 4.5, in order to be properly corrected even for the lateral strips. It is ~ 1 for the central strips and for the properly working channels, the ones used for the common mode calculation, while it grows up to ~ 10 in the lateral strips. The plot in fig. 4.6 shows the value of the coefficient for the strips lying close to the module edges (last P-side channels and first N-side channels).

Correcting with these factors the common mode in each event and for each strip, its subtraction can be improved in order to obtain a better estimate of the intrinsic noise: as experienced by applying this method to a sample of modules, for the strips placed on the edges it is possible to obtain a reduction of about 5-10 rms ADC-units for the noise after the subtraction, if compared with the unweighted correction, bringing them back to an acceptable noise level. The stability of the scale factors, which have been calculated on a large event statistics, was tested with good results on different data samples: therefore they can be calculated just once and then implemented in the FPGA in order to perform the improved correction at the hardware level.

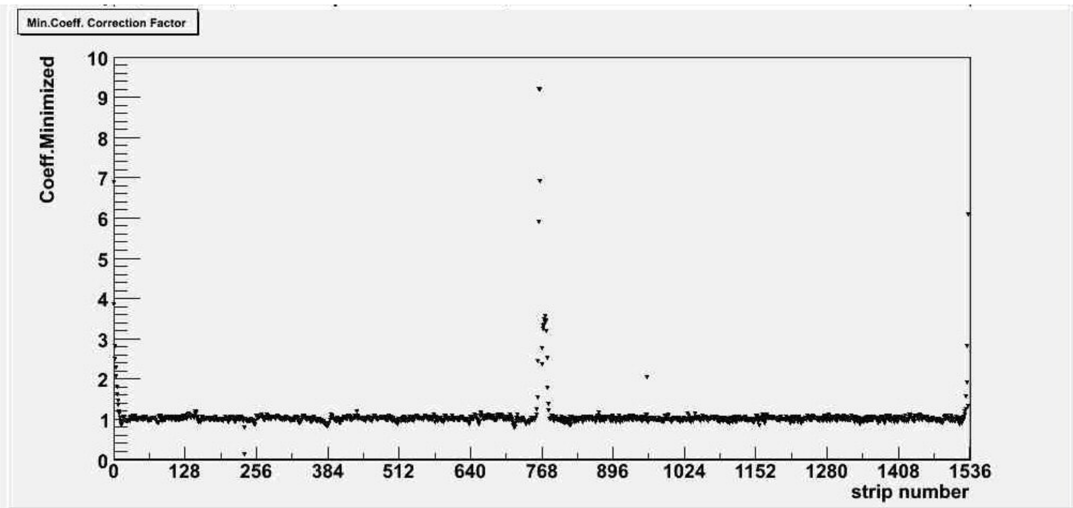

Figure 4.5: The common mode correction factor: the scale factor is plotted as a function of the 1536 channels of a module; multiplying this factor, that has been calculated for this specific module using the equation 4.4, by the common mode shift value, it's possible to correct better the signals and minimizes the intrinsic noise as regards these channels. Note that the 767 is the last channel of a module P-side, while 769 is the first of the N-side.

4.4 The current FEROM algorithm.

The algorithm implemented in the acquisition hardware during the commissioning phase, called *FastCM* algorithm, differs from the simple average over the chip channels belonging to the same chip only for a particular: it excludes the first and last 16 channels of each chip and applies a mask based on a static map in order to reject the channels classified as *bad*. This map contains all the channels presenting high noise, namely $\sigma > 20$ *ADC units* (*noisy*), whose front-end electronics is inactive (*dead*) or whose connection to the read-out is broken (*open*), as results from the analysis previously performed to calibrate the detector. Only 64 *good* channels belonging to the central region are used for the common mode calculation.

This algorithm filters the signals taking into account the well known defects, but it is unsafe for what regards unexpected high-noise events and particle events, whose position is unpredictable.

In order to test its performances, the residuals with respect to the 'true' common mode shift have been calculated for 500 real noise events and used to fill an histogram. The resulting distribution measures the goodness of the algorithm in the specific case. The performance test has been carried out on a large number of modules belonging to different ladders.

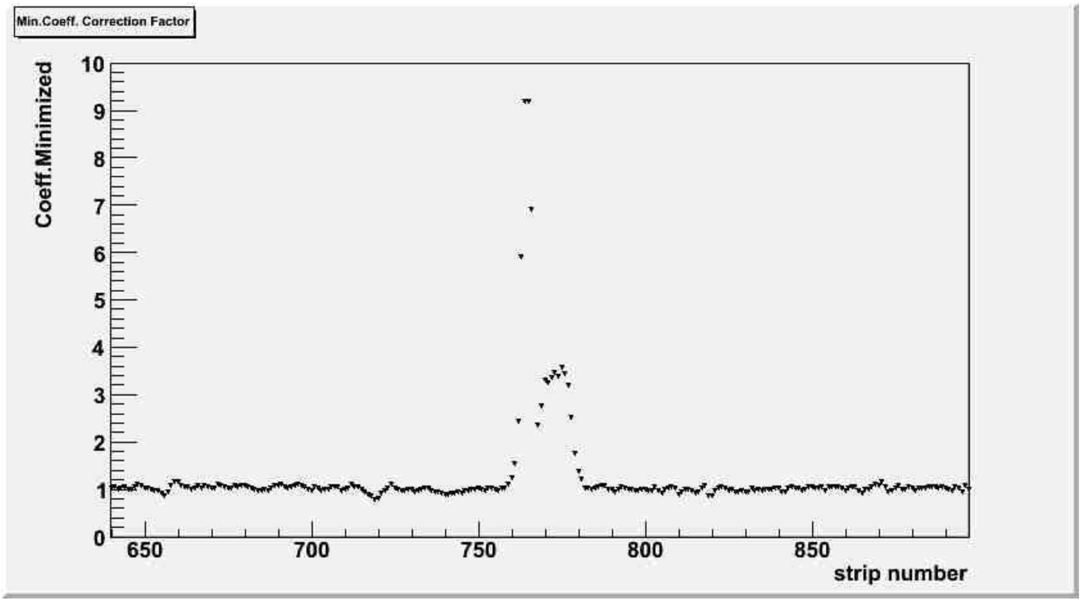

Figure 4.6: The scale factor for the common mode correction for the channels lying near the module border. It reaches the value of 10, while for the channels corresponding to the central region of the sensor is about 1.

4.4.1 The algorithm performances.

For chips presenting a homogeneous noise σ not larger than 7 rms units, the algorithm shows very good results: the differences are distributed around zero with a $\sigma < 1$ (left histogram in fig. 4.8).

In the case of a chip hosting some channels with a very large noise (up to 100 rms units in the histogram shown in the left panel of fig. 4.7), the simple average would miscalculate the common mode shift by a quantity that depends on the signals from these noisy channels while the implemented algorithm calculates properly the shift. The large distribution of the errors made with a simple average is shown in the left histogram. On the right the results of the actual algorithm: the mask applied to the bad channels is very efficient and the errors are negligible (smaller than 2 ADC units in the 98% events).

Finally, the presence of particle signals has been simulated adding on the same 500 noise real events some pulses randomly distributed over the 64 central channels. The simulation of 5 MIPs equivalent signals (5×140 ADC units) produces the effect shown in the right histogram in fig. 4.8, i.e. a mean residual of about 11 ADC units. Therefore, the presence of particle signals introduces a systematic error, related to the number of particles detected by the strips considered for the *FastCM* calculation.

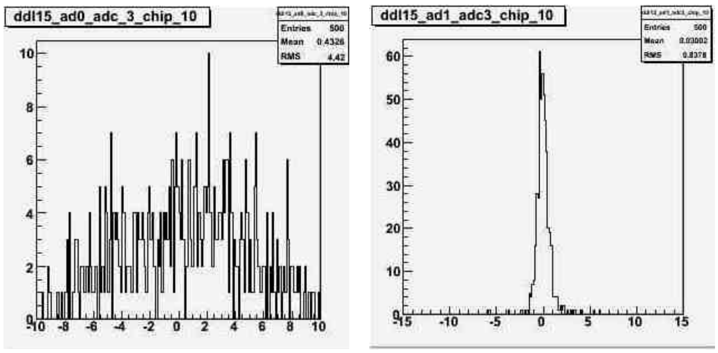

Figure 4.7: Residuals between the *true* common mode and the calculated one in presence of several noisy channels (with σ up to 100 ADC rms units) with *left panel* or without *right panel* the use of a mask to reject the *bad* channels.

The result is mostly independent of the clusters shape.

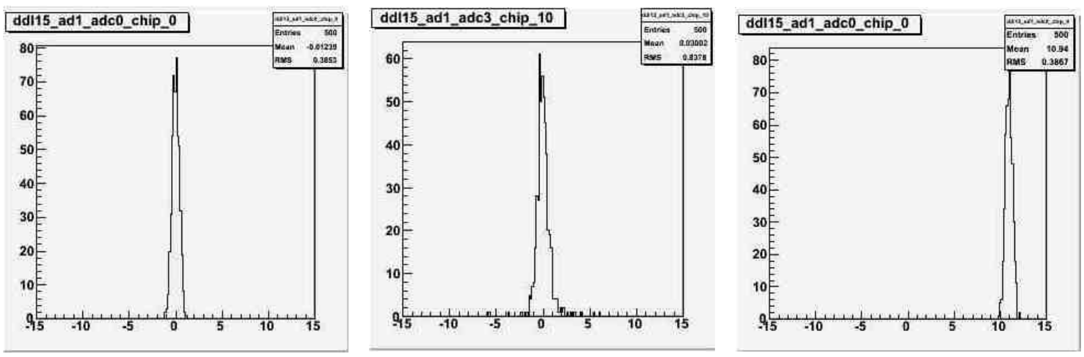

Figure 4.8: Performances of the common mode algorithm currently implemented in the SSD acquisition system: residuals with respect to the *true* common mode for: a chip with typical noise (uniform $\sigma \sim 4\,adc\ units$) and without particle signals *(a)*, very noisy chip (some channels with $\sigma > 15\,adc\ units$) without particle signals *(b)*; a chip in presence of particle signals *(c)* corresponding to 5 MIP. In the last case a systematic displacement can be noticed.

4.5 Proposals of two algorithms for the common mode correction.

In order to improve the algorithm efficiency in presence of particle signals, some other algorithms have been considered. They were evaluated in terms of performances, time consumption and simplicity of the executed operations.

The *multi step* algorithm, used in this work as benchmark algorithm in the *two steps* version, needs the data to be processed more than once to select the proper channels for the common mode calculation. This request can not be granted due to the architecture of the FPGA firmware that allows to process the data only once.

The *fast ascending* method, used e.g. for the readout chain of the CMS silicon Preshower detector, is based on simple operations and assured good results under different conditions (common mode shift calculated for groups of 16 channels). It can perform an on-line sorting of channels by pulse height and reject signals from particles [51]. This algorithm was considered not compliant with the hardware constraints by the FEROM firmware developers because of the large amount of channels to treat in the SSD case.

Eventually, two algorithms have been considered: the first is quite simple and consists in the introduction of a fixed threshold to exclude those channels hit by particles or simply presenting a high pulse. A possible more complex evolution of this method allows to solve most of the drawbacks of the *fixed threshold* algorithm: it is based on a *self tuning* procedure.

4.5.1 The *fixed threshold* algorithm.

A simple improvement of the *FastCM* algorithm implemented in the data acquisition system during the detector commissioning phase consists in the introduction of a fixed threshol, which rejects the high pulses from the channels not yet masked. The value chosen as threshold takes into account the typical common mode noise distribution in the SSD and minimizing the effects of the particle signals.

- **Algorithm description.** It considers only the central channels (from the 17th to the 112th strip) excluding the bad channels; among the unrejected, it accepts the signals below the threshold and averages them.

- **Performances.** The histogram in fig. 4.9 shows the distribution of the errors made by the algorithm, when a fixed 40 ADC units threshold is applied; i.e. rejecting all signals whose values are larger then 40 ADC units; the results are encouraging for all considered cases: in absence of particle signals, it reproduces the performances of the *FastCM* algorithm: the error is negligible both with and without the presence of noisy channels.

In presence of particle signals, the 40 ADC units threshold cuts most of the simulated particle signals: in case of a MIP, it is completely rejected when collected by one single strip, while in case of a multistrip cluster, only the tails can survive, if smaller than 40 ADC units. Also in case of high local particle multiplicity, i.e. with one particle per cm^2, the simulations show a residual smaller than 3 ADC units.

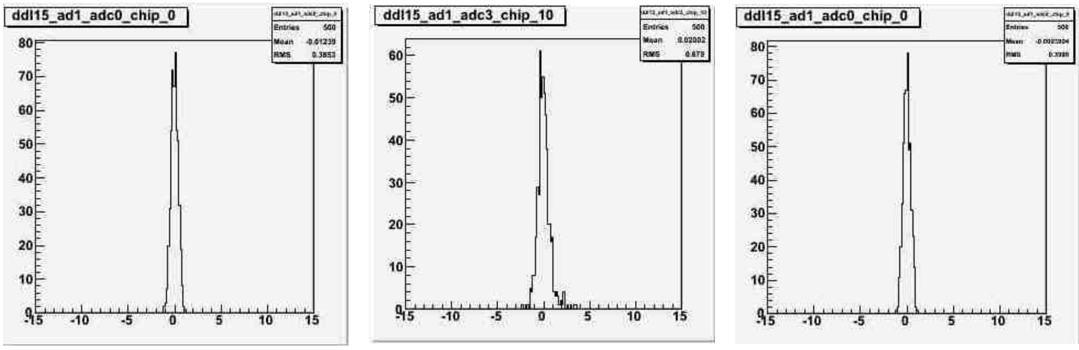

Figure 4.9: Peformances of the *fixed threshold* algorithm. The histograms show the residuals with respect to the *true* common mode for: a chip with typical noise (uniform $\sigma \sim 4$ *adc units*) and without particle signals *(a)*, very noisy chip (some channels with $\sigma > 15$ *adc units*) without particle signals *(b)*; a chip in presence of particle signals *(c)* corresponding to 5 MIP. In all these cases, the residuals are tightly distributed around zero.

- **Advantages and drawbacks.** The simplicity of the algorithm is preserved, since the comparison with the threshold is the only additional operation introduced by this algorithm. On the other side, the *fixed threshold* algorithm has some drawbacks: the threshold is not very tight, so that at least the tails of the multistrip clusters can influence the calculation; moreover, this algorithm rejects completely the events with a common mode larger than 40 ADC units. During noise tests, such a large shift of the baseline was rarely observed, since the typical common mode σ is equal to 7 rms units for the SSD modules.

  Moreover, the algorithm efficiency in discarding the particle signals strongly depends on the common mode magnitude and sign: while the threshold is fixed, the common mode oscillates so that the threshold effectiveness changes event by event.

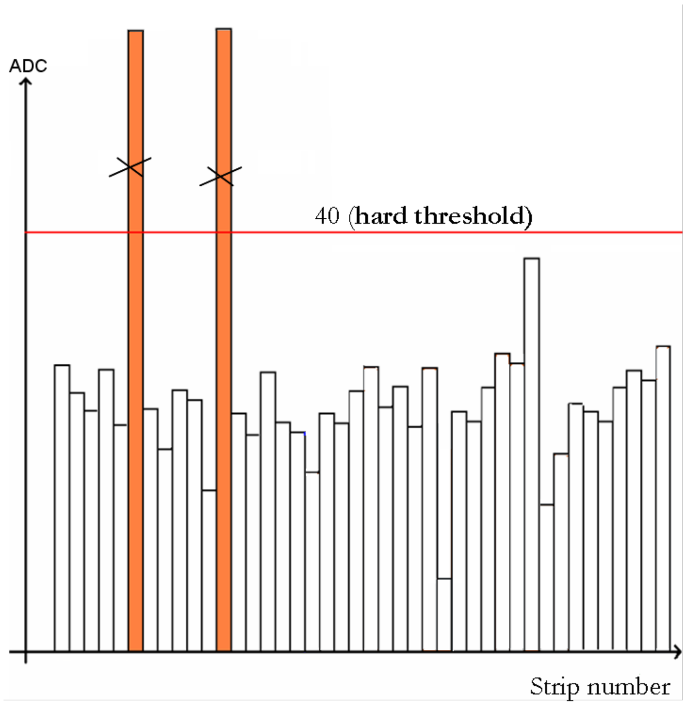

Figure 4.10: The *fixed threshold* algorithm: the signals above the 40 ADC units threshold (*red line*) are rejected and the common mode shift is calculated as the average of the remaining channels.

4.5.2 The *self tuning* algorithm.

In order to reduce further the errors and to avoid the loss of data in case of events with a very large common mode displacement of the channel baseline, another algorithm was designed and tested. It is structured into two phases, even if it processes the data just once. The *self tuning* procedure is described in the scheme reported in fig. 4.11.

- **Algorithm description.** The first and last 16 channels of the chip are excluded from the calculation. In the first part it calculates the common mode as a simple average (m) of the signals coming from 16 out of 32 strips (from the 17th to the 48th strips) and smaller than a threshold $T = 50\,ADC\ units$; this threshold has a quite large value, in order to exclude only the biggest signals and to include data with a large CM, reducing the risk to completely lose an event. In the second part it considers only the strips from the 49th to the 112th and takes into account only the first 32 signals whose amplitude S falls within a tight range around the previously calculated m, namely if it satisfies the condition $m - r < S < m + r$, with $r = 10\,ADC\ units$; the common mode

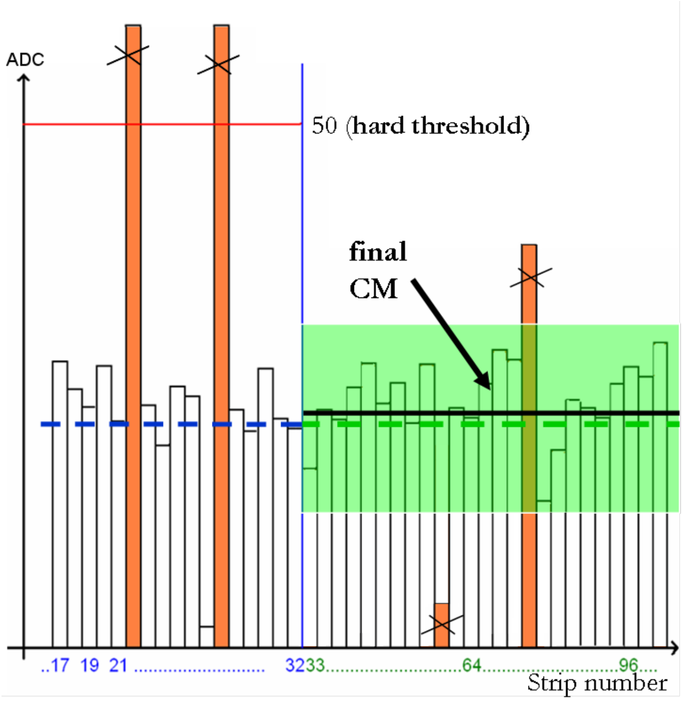

Figure 4.11: The *self tuning* algorithm operations: *a)* a fixed 50 units threshold (*red line*) applied on a first set of channels rejects very high signals; *b)* the other signals are averaged (*dashed blue line*); *c)* among the second channel set, only the signals within a certain tight window around the previously calculated mean are accepted (*green range*); *d)* finally, the average of the accepted signals determines the common mode shift of the event (*black solid line*).

shift is calculated as the average of the accepted signals.

- **Parameters tuning.** A study was carried out in order to optimize the parameters used by this algorithm:

  - The particles signals are simulated on the hypothesis of high particle multiplicity foreseen in heavy ion collisions: a further optimization will be possible after first measurements of this multiplicity on the basis of real data.

  - The number of strips included in the first and in the second group depends on the multiplicity of hits and of noisy strips on that zone of the detector and it has been tuned in order to minimize the error in the common mode evaluation and to maximize the number of strips used in every calculation. With the considered multiplicity, we obtained always at least 16 good strips in the first step and 32 in the second step, so that we always managed to calculate the common mode over a large sample.

- As already explained, the 50 ADC units threshold was chosen to accept events with large baseline displacements.
- The range defined by the parameter $r = 10$ *units* has been tuned according to the typical dispersion of the signal amplitudes in absence of physical events.

- **Performances**: the *self tuning* algorithm gives good results in presence of noisy channels and physical signals, accepting common mode shifts as high as 50 units; it should be noted, anyway, that such a large common mode shift appears to be rare in the SSD environment and it mostly affects chips presenting also an uncommon intrinsic noise behaviour; therefore it can be hardly corrected. As shown in the left and central histograms of fig. 4.12, it gives very good results without particle signals. It is also very robust in presence of particle signals, even in case of very high multiplicity: even in presence of multistrip clusters, the tails accepted by the window can introduce an error smaller than 1 ADC unit. The *self tuning* algorithm is compatible with the mask for bad channels. But can give good results also without that mask. Contrary to the *fixed threshold* case, the present algorithm effectiveness is rather stable and independent of the common mode magnitude. Moreover, it preserves the characteristic of simplicity, since it adds only an average calculation and comparison operations to the algorithm.

4.5.3 Common mode correlation between neighboring chips.

The case of a failure of the common mode correction performed at the hardware level is here considered.

The algorithm class discussed before bases the common mode calculation on the channels selected through a system of thresholds: in some particular cases, such an algorithm can fail to reach the minimum required number of channels to calculate the oscillation. This type of failure can happen for example:

- in the events with a very large displacement of the baseline, which turns out to bring the signals above the threshold;

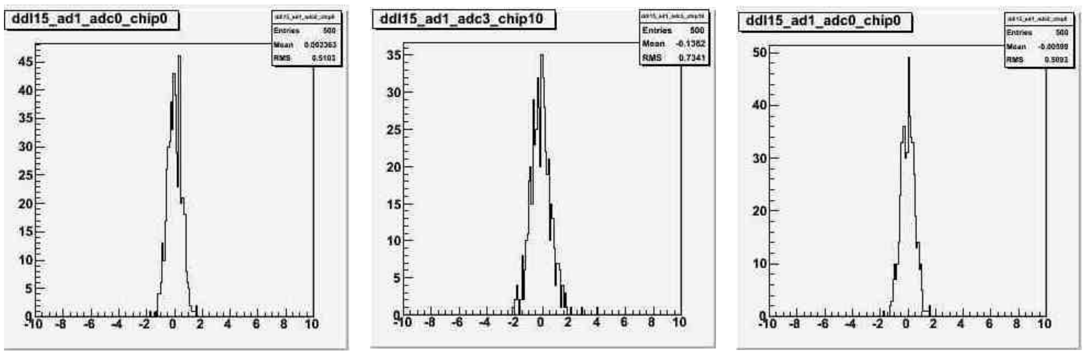

Figure 4.12: Peformances of the *self tuning* algorithm. The histograms show the residuals with respect to the *true* common mode for a chip with typical noise (uniform $\sigma \sim 4$ *adc units*) and without particle signals *(a)*, very noisy chip (some channels with $\sigma > 15$ *adc units*) without particle signals *b*; a chip in presence of particle signals *(c)*. In all these cases, the residuals are distributed around zero with a $\sigma < 1$.

- for chips presenting a high local particle hit multiplicity, where many channels are then rejected;
- in drastically disturbed events.

In these cases, it is fundamental to switch off the usual common mode correction and to try to recover an estimate of the common oscillation basing the calculation on a larger group of channels: with this purpose, the common mode oscillations of a chip has been studied as a function of the oscillation of the other chips belonging to the same module.

In order to take into account the possible influence of the constructive characteristics of the SSD sensor on the common mode oscillations, the behaviour of modules of all the three different manufacturers has been observed. All the considered samples show a linear dependence between the oscillations of different chips, with a linear coefficient close to ~ 1 for first-neighboring chips. Therefore a calculation failure in a chip can be solved extrapolating the common mode value from a neighboring chip.

In case of loss of informations about neighboring chips, it is even possible to take the common mode corresponding to a chip from the opposite module-side, with a maximum statistical σ of 2 ADC rms units. In the table (fig. 4.13) we can read the RMS of the distribution of the difference between common mode oscillations of different chips, over a statistics of 500 events for a module. We found a similar behaviour in all the modules we analyzed, including all manufacturer-types and the noisy modules. Moreover, the RMS of the difference between j-th and *(j+1)*-

th chips is always smaller than 1 unit (see along the diagonal). The coefficient of

	chip0	chip1	chip2	chip3	chip4	chip5	chip6	chip7	chip8	chip9	chip10
chip0		0.6241	0.7075	0.7644	0.8123	0.7952	1.0640	1.4860	1.8390	2.5440	2.3910
chip1	0.6241		0.3762	0.4674	0.5251	0.5131	0.9096	1.4000	1.7840	2.1040	2.3620
chip2	0.7075	0.3762		0.2327	0.3235	0.3468	0.7580	1.2750	1.6640	1.9850	2.2480
chip3	0.7644	0.4674	0.2327		0.2119	0.2656	0.7219	1.2430	1.6330	1.9580	2.2240
chip4	0.8123	0.5251	0.3235	0.2119		0.2104	0.5368	1.2120	1.6030	1.9360	2.2020
chip5	0.7952	0.5131	0.3468	0.2656	0.2104		0.5830	1.1290	1.5300	1.8610	2.1280
chip6	1.0640	0.9096	0.7580	0.7219	0.5368	0.5830		0.5504	0.9529	1.2840	1.5520
chip7	1.4860	1.4000	1.2750	1.2430	1.2120	1.1290	0.5504		0.4039	0.7417	1.0030
chip8	1.8390	1.7840	1.6640	1.6330	1.6030	1.5300	0.9529	0.4039		0.3387	0.6054
chip9	2.5440	2.1040	1.9850	1.9580	1.9360	1.8610	1.2840	0.7417	0.3387		0.2738
chip10	2.3910	2.3620	2.2480	2.2240	2.2020	2.1280	1.5520	1.0030	0.6054	0.2738	
chip11	2.5440	2.5240	2.4120	2.3890	2.3680	2.2950	1.7180	1.1750	0.7726	0.4419	0.1770

Figure 4.13: The RMS of the distribution of the difference between the common mode oscillations of different chips belonging to the same module (500 events sample).

linear dependence between the common mode of different chips can be considered to calculate the possible error also in case of larger noise: taking the neighboring chip common mode it can generate a maximum relative error of about 15% (see fig. 4.14).

	chip0	chip1	chip2	chip3	chip4	chip5	chip6	chip7	chip8	chip9	chip10
chip0		0.9602	0.9017	0.8448	0.8434	0.8354	0.7089	0.5877	0.4942	0.4218	0.3242
chip1	1.0220		0.9390	0.8807	0.8797	0.8707	0.7405	0.6149	0.5178	0.4425	0.3417
chip2	1.0810	1.0570		0.9394	0.9385	0.9289	0.7912	0.6583	0.5556	0.4762	0.3688
chip3	1.1420	1.1180	1.0590		0.9989	0.9890	0.8450	0.7058	0.5984	0.5149	0.4022
chip4	1.1400	1.1160	1.0580	0.9987		0.9900	0.8452	0.7055	0.5975	0.5135	0.4000
chip5	1.1490	1.1250	1.0660	1.0070	1.0080		0.8550	0.7151	0.6068	0.5225	0.4090
chip6	1.1340	1.2890	1.2240	1.1590	1.1600	1.1520		0.8507	0.7344	0.6437	0.5220
chip7	1.4740	1.4490	1.3770	1.3100	1.3100	1.3040	1.1510		0.8807	0.7873	0.6627
chip8	1.5670	1.5420	1.4700	1.4040	1.4020	1.3990	1.2560	1.1130		0.9100	0.7890
chip9	1.5880	1.5650	1.4950	1.4350	1.4310	1.4300	1.3070	1.1820	1.0800		0.9357
chip10	1.5450	1.5260	1.4620	1.4080	1.4030	1.4050	1.3080	1.2060	1.1210	1.0540	
chip11	1.4590	1.4430	1.3850	1.3390	1.3330	1.3380	1.2670	1.1890	1.1220	1.0680	1.0250

Figure 4.14: The coefficients of linear dependence between the common mode values of different chips belonging to the same module.

Chapter 5

The charged particles multiplicity measurement with the SSD.

As already discussed while introducing the physics of the heavy-ion collisions, one of the first and most fundamental observables characterizing these interactions is the multiplicity of produced particles. From the experimental point of view, it provides detailed information about the detector performances and therefore the accuracy of the measurement of many observables. Moreover, by counting the points and tracks reconstructed in the experiment, many properties of the interaction can be derived [52].

The multiplicity of the charged particles and the pseudorapidity distribution $dN/d\eta$ will constitute the first basic observable in ALICE, in both p-p and Pb-Pb interactions at LHC energies. The full pseudorapidity η range covered by the experiment extends over about 8 units. The best measurement in the central region is expected to be obtained with the first two layers of the Inner Tracking System, the Silicon Pixel Detector (SPD, see 2.3.4), thanks to its characteristics in terms of granularity and coverage. The measurement of the charged particle multiplicity in the forward and backward regions of η will be performed by a dedicated detector, the Forward Multiplicity Detector (FMD) [53]. Another multiplicity measurement in ALICE is expected to be performed with a full tracking, that is mainly based on information from the Time Projection Chamber (TPC) [54].

This chapter describes the feasibility study of the charged particle multiplicity measurement in p-p collisions to be performed by the ALICE Silicon Strip Detector (see chapter 3 for a detailed description). This measurement will be aimed both at the evaluation of the SSD efficiency and at the characterization of the observed events at the SSD position, resulting to be complementary with the measurements performed by the SPD, the FMD and the TPC.

This study was conducted within the software framework especially developed for the ALICE experiment, called *AliRoot*, which is briefly introduced in the first section of this chapter. A general description of the simulation and reconstruction chain is given, each one followed by the custom settings used for this particular work. The strategy and the results of the analysis are then presented, followed by a discussion on the feasibility of the measurement.

5.1 The ALICE offline framework: AliRoot

The ALICE offline framework is designed to manage the huge quantity of data produced by the experiment. This framework is called AliRoot and it is based on ROOT, an Object-Oriented framework written in C++ language [55].

ROOT is commonly used in high energy physics experiments thanks to its particular features: as shown in fig. 5.1, it is suitable to simulate, reconstruct and analyse the data coming from high energy physics experiments, since it contains the tools needed to simulate the event generation, the interaction between the particles and the detectors, to carry out the event reconstruction, the acquisition and the analysis of data. AliRoot extends the ROOT framework introducing the simulation of the

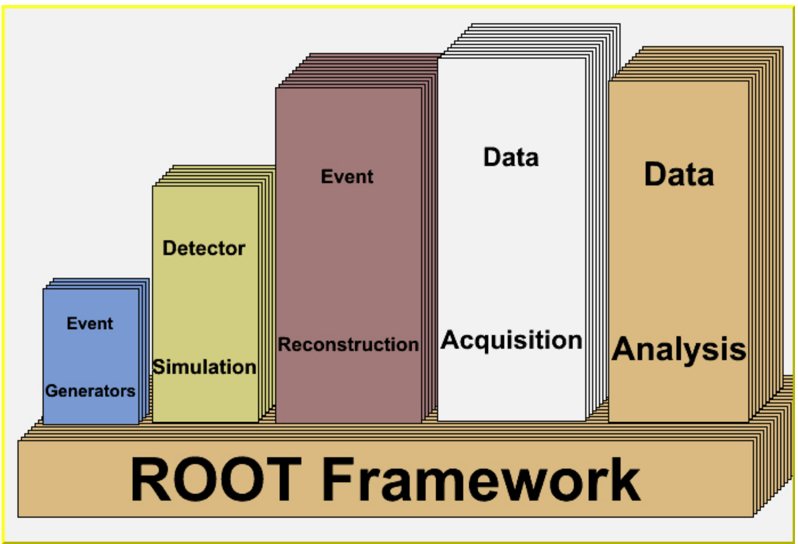

Figure 5.1: The ROOT framework: tools for high energy physics experiments.

detectors and the apparatus of ALICE, the algorithms developed for the specific reconstruction of each detector data, the tools for the specific analysis of the ALICE events.

The framework has been devised in order to leave the possibility of comparing step by step real data with simulated data. Both the simulation and the reconstruction chains are divided into intermediate steps: during each one of them, a set of specific algorithms is processed and produces an output. These output objects, available to the user, are taken by the framework as the input for the successive step.

This strategy allows to monitor each passage as an independent process and to tune it, considering all the possible contributions to the physical evolution that can take place in the real event. As indicated by the arrows in the processing data scheme, in fig. 5.2, it's also possible to skip some steps in order to speed up the reconstruction, losing, on the other hand, many features and informations. The study here presented demonstrates how the user can manage all the software components in order to perform the desired study.

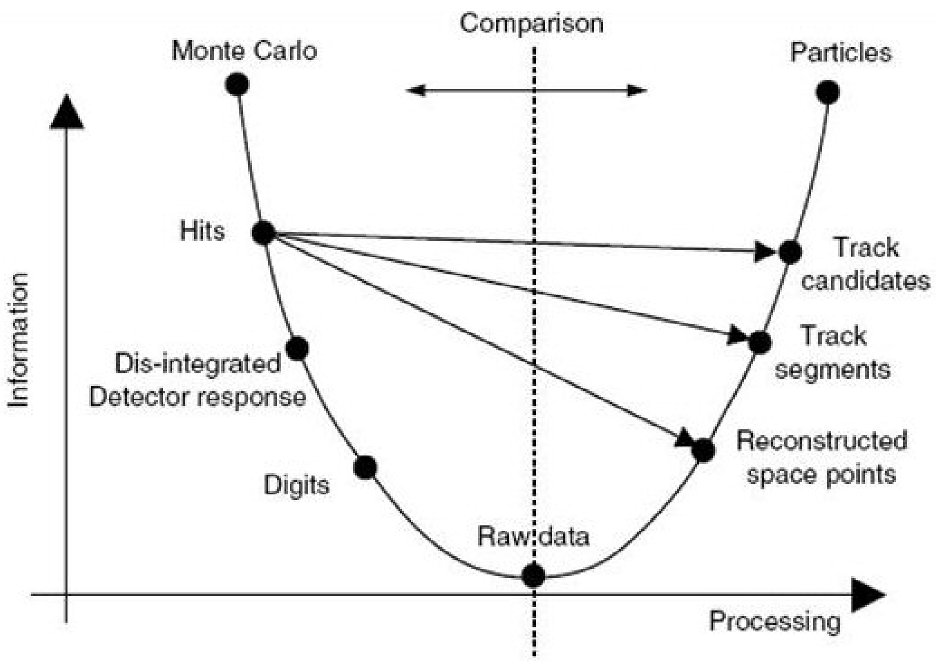

Figure 5.2: The AliRoot data processing framework: the simulation and reconstruction chains with their intermediate steps. The arrows show the possibility to skip some steps to speed up the reconstruction.

The most important characteristics of the framework, from the developer point of view, are the **Modularity** and the **Reusability**. Modularity allows the different developers to change and evolve their code without notable effects on the rest: for example, contribution regarding different detectors are independent and they can be developed in parallel; tools like the event generator or the Monte Carlo transport have to be changed without modifications in the user code. Reusability uses this modular structure and the backward compatibility to preserve the scientific knowledge included in the code and to make it available for future and different purposes.

5.2 Simulation

5.2.1 General description

The AliRoot simulation framework is designed to produce a complete simulation of the ALICE events, from the initial collision to the detectors response, optionally providing an output file in raw format, identical to the files produced by the real ALICE acquisition system. The procedure covers all the simulation steps and allows to control the parameters of each of them: the primary interaction, the emerging particles generation and their decays, the transport of particles through the detectors, the energy depositions in the detectors, the detector response merged with the simulated noise and the creation of output raw data.

All these steps can be configured by the user, storing the corresponding options in the *Config.C* file. Before the simulation starts, this file is processed. Through the configuration file, the user has also the possibility to set the initial conditions of the interaction, like the number of nucleons of the colliding particles, their c.m.s. energy, the vertex coordinates distributions; he can set up the particle generation, defining the pseudorapidity and the emission angle ranges for the emerging particles and their kinematic properties, like momentum and transverse momentum ranges; he can tune the event evolution forcing or excluding particular decay channels.

Starting from the generation step, it's possible to choose among the following set of event generators to simulate the collision according to the study requirements:

- HIGJING: based on a QCD model of jet production and fragmentation, it is used to generate heavy-ion interactions; it includes important features like jet quenching and nuclear shadowing, which are expected in lead-lead collision;

- parametrized HIJGING: based on parametrized pseudorapidity density and transverse momentum distributions of charged and neutral pions ad kaons, it can produce final states avoiding the dependences on a specific model; it is suitable to estimate the track reconstruction efficiency;

- PYTHIA6: it can simulate proton-proton interactions taking into account all the known dynamical aspects; it can be used also for jets generation in case of events merging;

- additional universal generators (Herwig, Isajet, DPMjet) used to study specific interactions and to test particular models;

- cocktail generators: combination of different generators that add their own generated particles to the event stack.

The emerging particles are produced with their momenta; the information about the vertex and the mother-daughter relationship are maintained.

The next step, i.e. the transport of the particles within the ALICE volume, can be simulated with three Monte Carlo software packages: GEANT3, FLUKA or GEANT4. They create the detectors geometry on the base of the detectors description provided by the user and they propagate the particles. The energy lost by Coulomb interaction while traversing the sensible elements is transformed in signals, according to the specific response of the various detector types. The signals are finally converted to a digital format.

Performing the operations described before, AliRoot generates a set of files including all the information related to the event kinematics and to the objects created by each step of the simulation chain. In particular, these objects can be defined as follows:

- **Hits**: the energy deposited in a given position by the particles traversing a sensitive volume unit in the detectors is called hit; they maintain also the information about the particles that generated them;

- **SDigits**: when the detector response is taken into account, hits are transformed in summable digits; these objects have an additive format: they are used, for example, to merge signal events with underlying signal-free events; this step can be optionally skipped to transform directly hits into digits;

- **Digits**: hits are eventually transformed into digits, taking into account the detector response; each digit can be considered as the simulated response of a single channel of the ALICE detector; it is not related anymore to the Monte Carlo track that originated it, except for the label, which carries this information.

Digits are normally produced in the ROOT tree format, but can be optionally converted into raw data, according to the real front-end electronics and the Data Acquisition System output.

5.2.2 Custom settings

In order to explore the possibility of a multiplicity measurement with the SSD, a simulation was performed to produce p-p events data, comparable with expected first real data.

For the first period of activity, the LHC physics program foresees to collide protons at 900 GeV. ALICE is supposed to characterize the events with a multiplicity measurement, which can be performed with high precision by its detectors. For this purpose in the configuration file some fundamental reaction parameters have been set as follows:

- **event type**: p-p events;

- **c.m.s. energy** $\sqrt{s}$ = 900 GeV: during the first physics production, protons collide at a center of mass energy equal to 900 GeV;

- $V_z = 0$: the vertex position along the beam axis (z) is fixed at the origin of the ALICE reference frame; it allows to perform a preliminary measurement not biased by the vertex position distribution;

- 0 GeV/c < P_t <1000 GeV/c: the transverse momentum range for the generated particles;

- $0° < \vartheta < 180°$: the emission angle range with respect to the beam axis for the generated particles;

- $-12 < y < 12$: the rapidity range for the generated particles;

The PYTHIA generator has been selected; as previously mentioned, PYTHIA provides a generation of high energy physics events, namely hard interactions between elementary particles such as protons, like in this case, but also between electrons, positrons and antiprotons in various combinations. A detailed treatment of the physics of the interaction is performed by the generators: hard and soft interactions, parton distributions, initial and final state parton showers, multiple interactions, fragmentation and decay.

The detector geometry and the particle propagation have been simulated via the AliRoot interface to GEANT3: the interactions between the charged particles and the sensible elements of the SSD detector create the mentioned *hits*, which have been studied and taken as the benchmark for the subsequent analysis.

For the final production of the simulated data, the ROOT tree format has been selected, in order to have complete access to the information related to the production vertex and to the mother-daughter relationship of the particles that generated the data.

5.3 Reconstruction

5.3.1 General description

The reconstruction starts from digits, which can either be in ROOT tree format or in raw data format. The first step consists in the *local reconstruction* performed by each single detector module: the data corresponding to each detector are elaborated by specific algorithms in order to *clusterize* the signals and to define the space points (see next paragraph for a complete description of the SSD clusterization algorithm). Once these operations have been performed by all the selected detectors for which the local reconstruction feature is available, the *tracking* is carried on. It consists of fitting the space points, reconstructing vertices and tracks and identifying the particles. At the end, the output of the reconstruction is stored in the ESD (*Event Summary Data*).

The following objects appear in the reconstruction processes:

- **Digit**: a signal read out by a channel of the detector at a certain time; if produced by the simulation, its ROOT tree can contain the label of the particle that generated it;

- **Cluster**: a group of adjacent digits that were presumably generated by the same particle crossing the sensitive element of the detector.
- **Recpoint** or *reconstructed space point*: the reconstructed position where the particle crossed the sensitive element of the detector; this object can contain also the information about the interaction, like the energy lost by the particle, or about its reconstruction, like the number of digits that originated it.
- Reconstructed **Track**: the trajectory of the particle, expressed by a set of parameters, like the curvature, the angles with respect to the coordinate axes and covariance matrix.

For the purpose of the present study, only the products of the ITS local reconstruction are considered: the SSD Recpoints are the object of the analysis while the SPD and SDD data were used to cross check the SSD results.

5.3.2 The *cluster finder* algorithm

The local SSD reconstruction is performed by an algorithm called *cluster finder* and consists in three main operations: the clusterization of the signals, the association of two clusters lying on the opposite sides of a module, the definition of the Recpoints and their properties.

It is useful to briefly describe the processes performed by the cluster finder in the specific SSD case:

- **clusterization**: as mentioned, a cluster is a group of signals originated by a particle traversing a portion of the detector. A signal has to pass a threshold to be taken into account, otherwise it's rejected. In the SSD case, for each channel this threshold is proportional to its intrinsic noise. The accepted signals coming from adjacent strips of a module side are grouped together in a cluster. The total charge is defined as the sum of the single strip signals; the cluster position is defined as the centre of gravity and it is defined weighting the digit positions by the charge of each digit;
- **geometrical matching**: since the crossing point between two opposite clusters must take place within the sensor, a geometrical condition is imposed to the pair of clusters.

- **charge matching**: two opposite clusters that satisfy the geometrical matching condition can be associated only if their total charges q_P and q_N, for the P side and N side cluster respectively, meet the condition $|\frac{q_P-q_N}{q_P+q_N}| < 0.2$; this value has been optimized taking into account the differences in the response of the two sides.

- **Recpoint definition**: if the 1-D clusters satisfy both conditions, they can be associated to create a Recpoint, with position and charge inherited from the clusters. The local coordinates on the module are derived from the center of gravity of the 1-D clusters through trigonometric calculations based on the strip inclinations; the point charge is defined as the mean of the two 1-D cluster charges. Also the number of digits composing the clusters is stored.

- **Recpoint classification**: the Recpoints are classified accordingly to the number of possible ambiguities encountered in their definition process. A Recpoint is tagged as *golden* if each one-dimensional cluster that contributed to the point reconstruction has only one possible partner on the opposite module side satisfying the geometrical condition; the other Recpoints are saved anyway, even if they are marked as lower quality points.

This algorithm was already present in the code in a preliminary version. In view of this study, that can be considered the starting point of the SSD physics commissioning, this algorithm has been debugged and modified in order to improve its performances in terms of reconstruction efficiency and purity. In particular, two features were added: the *5 σ seed* request and the unification of the reconstruction algorithms used for both the data formats, *raw* and *ROOT tree*.

As previously explained, the first step of the point reconstruction is the identification of that one-dimensional clusters, composed by signals coming from adjacent strips of a module side.

The discrimination of particle signals is usually done comparing the signal acquired by a channel with the typical RMS noise of the same channel. The multiplicity of fake clusters composed of two or more strips was found to be higher than expected, probably because of some local coherent oscillation in presence of microscopic defects in the sensor. Therefore, once selected all the adjacent strips presenting signals larger than 3 noise σ, to avoid this kind of problems it is necessary to apply a tighter threshold to at least one signal of the cluster. After some efficiency tests the threshold was fixed to a value of 5 σ. In Table 5.1 the results of a noise data set reconstructed with and without the 5 σ seed request are compared.

The cluster finder code was then revised in order to unify the elaboration of data in the various formats. Since raw data coming from the read-out electronics are sorted in different orders with respect to the ROOT tree format generated by the simulation, the reconstruction initially follows two different procedures to extract data from the files and to find the one-dimensional clusters. In both of them, the same criteria and selection rules have been implemented, so that created objects are homogeneous. This feature will allow to compare data coming both from the real acquisition and from the simulation.

RUN	Events	clust. Layer 5 (No 5σ seed)	clust. Layer 6 (No 5σ seed)	clust. Layer 5 (with 5σ seed)	clust. Layer 6 (with 5σ seed)
60437	8191	471	71	400	29
60438	8322	535	75	459	41

Table 5.1: The reconstructed cluster multiplicity in a noise run: the reconstruction performed with the old cluster finder, requesting the signals to pass only the 3σ threshold, is compared with the reconstruction performed requesting at least one signal to pass the 5σ threshold. In the table the total number of clusters per layer in two *noise runs* (random trigger, no particle signals) is shown, comparing the results of the old algorithm reconstruction with the new algorithm ones. The comparison concerned run 60437 and run 60438, in which more than 8000 noise events per run have been collected.

5.4 The calibration framework

The information finally obtained from the simulation and the reconstruction is function of both the response of the detector and the cluster finder algorithm. It is possible to control the detector response tuning some parameters like the gain factor, the single channel noise and the single channel functionality.

To get these parameters, a series of brief *calibration runs* is periodically scheduled during the experimental data taking of ALICE: the noise data collected through a random triggered acquisition and without any data filtering are used to calculate and periodically update the calibration objects.

The calibration data are stored in ROOT files, which can be accessed through the *Offline Conditions Database (OCDB).* The OCDB is a file catalog that points to the physical calibration files stored in the storage elements of Grid[1]. The user can put and retrieve these files from Grid to the local database and viceversa. The files are read-only accessible and the system unambiguously identifies them by a logical path name, a run range, the Grid and local version numbers. Therefore, it's possible to retrieve the desired files and reproduce the particular conditions of the detector at a certain moment. Moreover, such type of objects can be also created with arbitrary characteristics, for example with the aim to simulate a specific detector configuration and to study its effects.

For this work, the detector has been simulated in two different configurations for the simulation and reconstruction of the data sample: in the first one, the ideal case of an SSD without any defective strip has been considered in order to have a benchmark sample. In the second sample, the calibration files corresponding to the run 60281 was chosen as a realistic configuration for the SSD. 2000 events have been generated for each sample. The details of the chosen configurations are illustrated in the following paragraphs.

5.4.1 The ideal SSD

One can define the "ideal" SSD as a detector with a 100% quality: abiding by the definition described in par. 2.3, in such a perfect detector all the channels are supposed to be properly operating and to present an acceptable signal-to-noise ratio. To simulate these conditions, a custom empty *bad channels* list has been prepared and a flat noise pattern has been generated, assigning a 3 ADC units value to the P-side channels and 4 ADC units to the N-side channels. This choice allows to achieve a signal-to-noise ratio larger than 50 and 30, respectively, as measured in laboratory tests. Accordingly to the AliRoot procedure, these parameters have been stored in the local calibration database and used in the simulation and reconstruction chains. In fig. 5.3 the flat noise pattern is plotted as it can be read from the OCDB file.

5.4.2 The realistic SSD

Another amount of 2000 *p-p* events have been produced in the second sample: the real detector response as captured before *run 60281* was introduced in the simulation

[1]Grid is the data storage and analysis infrastructure designed to handle the massive amounts of data produced by high energy physics experiments taking place at the LHC.

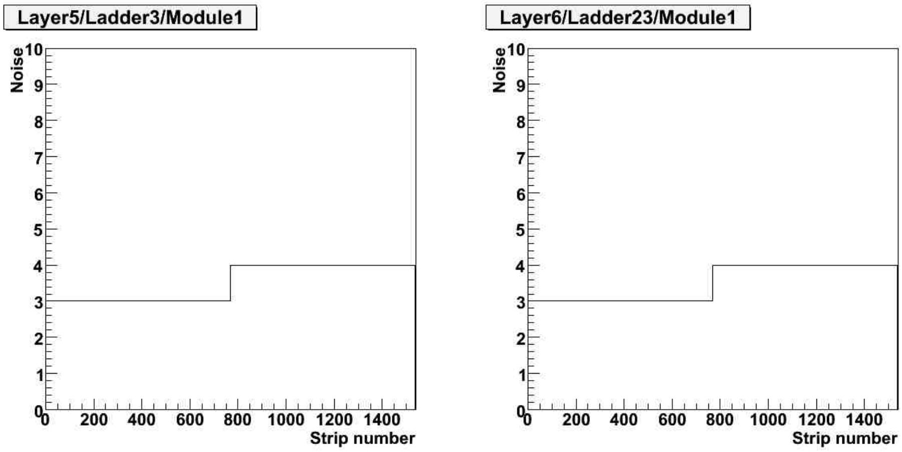

Figure 5.3: The flat noise pattern simulates a perfect response of the detector, as shown for two modules randomly chosen from both SSD layers. All the channels corresponding to the P side strips (from strip 0 to strip 767 in the plot) have a noise of 3 ADC units, the N side channels have a noise of 4 ADC units.

and reconstruction through the calibration files retrieved from the OCDB.

A visualization of the information stored in those files is shown in the figures: the distribution of inactive channels over the two different layers, distinguished by module side (P and N), is plotted in fig. 5.4. In addition, the noise corresponding to the channels of 8 modules randomly chosen from both the SSD layers is shown in fig. 5.5.

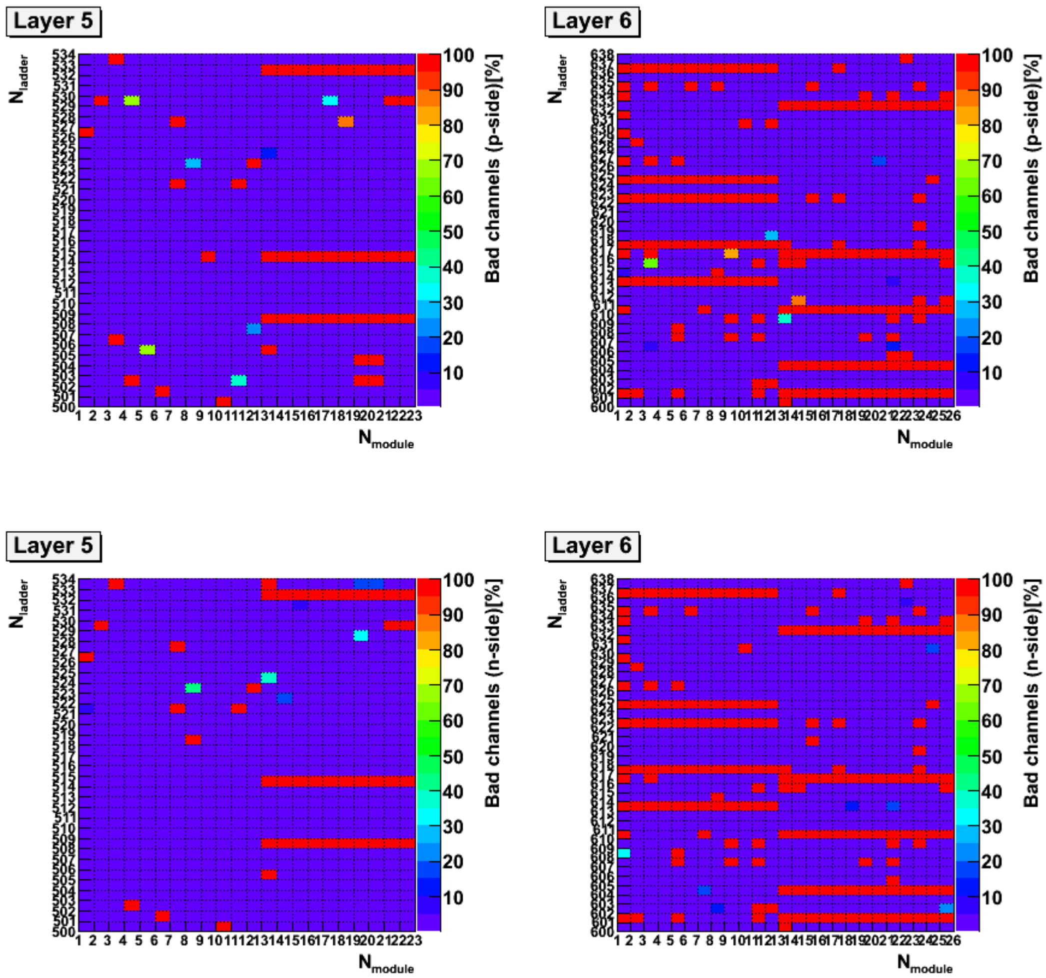

Figure 5.4: The distribution of the *bad channels* over the SSD modules, in percentage. The modules are identified by the ladder number (y-axis) and the position in the ladder (x-axis). The left panels show the Layer 5 situation, for P side *(upper panel)* and N side *(lower panel)*; the same for Layer 6 in the right panels. As indicated by the color scale, the red modules are switched off modules (100% *bad channels*). 13 half-ladders are disabled.

This particular example simulates a case where three half-ladders on Layer 5 and ten on Layer 6 had been switched off, due to functionality problems mostly related to biasing problems. The total percentage of *bad channels*, which were excluded by the acquisition, is summarized in Table 5.2, and it includes also the defective modules and the problematic single channels relative to run 60281.

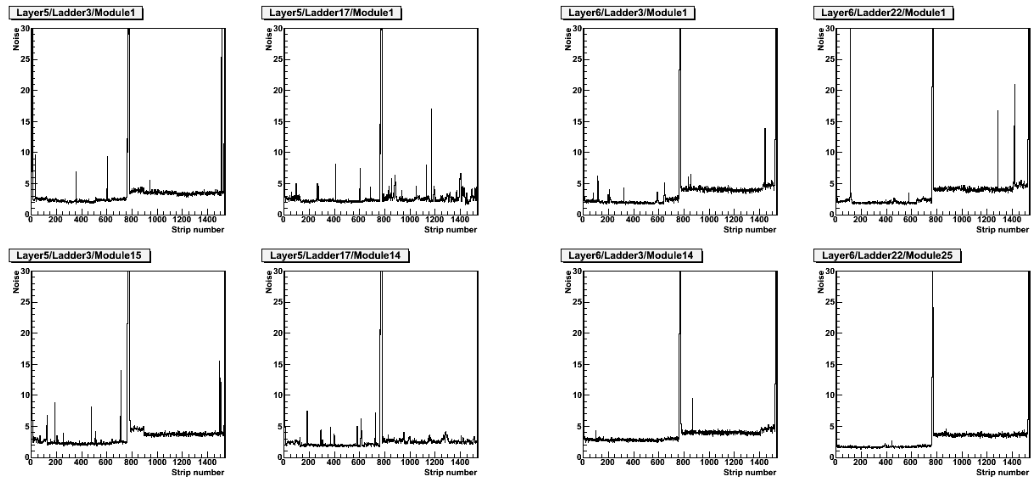

Figure 5.5: The real noise pattern of the SSD as it was recorded before run 60281 and used for its calibration. Four modules belonging to Layer 5 are shown in the left four panels; Layer 6 modules are shown in the right panels. The spikes indicate high noise strips, and are mostly concentrated on the module borders; a typical value for a good strip is 3 ADC units for P side and 4 ADC units for N side.

Run 60281	Layer 5	Layer 6
Bad p-side channels	6.2582%	15.1562%
Bad n-side channels	5.9254%	14.9177%

Table 5.2: Bad channels percentage over the total number of SSD channels during run 60281, divided by module side and by layer.

5.5 The analysis

The study presented in this chapter is aimed at the characterization of the observed events with a measurement performed by the SSD in stand-alone mode. For this research, a preliminary investigation was carried out to check the coherence of the various simulation and reconstruction processes that involve the SSD. With this purpose, the particle set produced by the generator with its momenta, direction and pseudorapidity distributions was compared with the results of the Monte Carlo transport through the tracking silicon detectors, i.e. with the hits produced on the SPD and SDD detector, checking their consistency step by step. On the other hand, to verify the coherence of the SSD Recpoints and the results of the full tracking procedure, the *Event Summary Data* were queried. The study was then focused on the comparison between simulated hits and reconstructed points in the SSD layers: the efficiency of the detector and its reconstruction algorithm, which are the main objects of this study, play an important role in the digitization of the hits and in the definition of the reconstructed space points. Therefore the attention has been addressed at first to the differences between Hits and Recpoints with a perfect detector response; then, the variations of these differences as a function of the detector conditions were considered.

With regard to the cuts applied during the analysis:

- **Hits**: a hit is counted each time a charged particle traversed a sensible element of the detector in the Monte Carlo simulation; no further selection was applied to the simulation.
- **Recpoints**: only *golden* Recpoints are considered in the analysis (see 5.3.2 for the definition); this selection avoids the ambiguities and suppresses the number of fake Recpoints.

5.6 The results

As already explained, the capabilities to infer an estimation of the charged particles multiplicity from an SSD measurement has been explored. To this aim, the simulated hits distribution has been compared with the Recpoints one. This comparison gives an estimation of the overall efficiency of the detector, including the detection efficiency and the reconstruction algorithm efficiency. Once this efficiency map is determined, it will be possible to characterize the primary interaction starting from the charged particles measurement.

5.6.1 Z-phi distribution

In order to understand the evolution of the observed events, the hits distribution in the z-φ plane was observed, where z [2] coincides with the beam axis and φ [3] is the

[2] The mentioned global ALICE coordinate system is defined in the following way: it is a righthanded coordinate system with the z-axis coinciding with the beam pipe and pointing in the direction opposite to the muon arm; the y-axis goes upward; the system origin is defined by the intersection point of the z axis with the central membrane plane of the TPC.

[3] The rotation coordinate around the beam axis, namely φ, can be calculated from the global coordinates of the point with the simple trigonometrical formula

$$\varphi = \arctan(\frac{y}{x}) \tag{5.1}$$

.

rotation angle around the beam axis. As expected, the hits multiplicity is higher in the central sector of the barrel and decreases towards the edges of the SSD, as the Monte Carlo kinematic model foresees.

In the ideal SSD case (fig. 5.6), the comparison between Hits and Recpoints distribution highlights the reconstruction efficiency. The same analysis performed in the realistic case spotlights the effect of the disabled half-ladders. The z-φ plane sectors occupied by those half-ladders appear like holes in the detector (blue sectors in fig. 5.7).

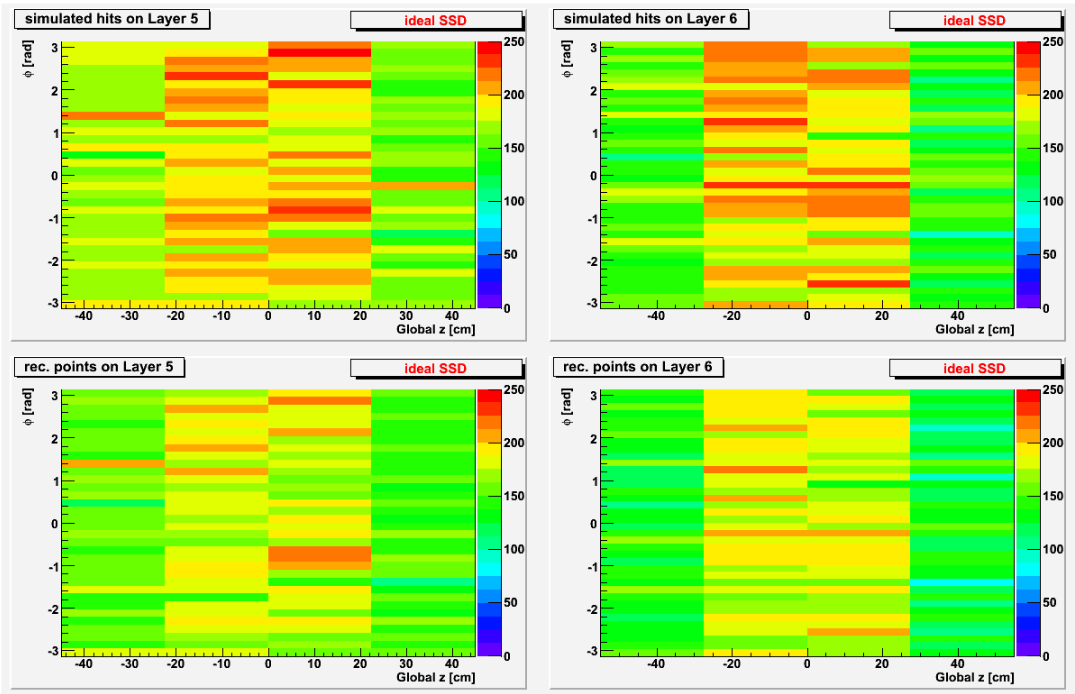

Figure 5.6: Ideal SSD: Hits and Recpoints distribution in the z-φ plane for the 100% efficient detector, integrated over 2000 events. The upper panels show the hits generated in Layer 5 (left) and in Layer 6 (right). The plane is divided into sectors corresponding to a quarter of a ladder approximately. The hits concentrate mainly in the central sectors, corresponding to the central part of the SSD cylinders. In the lower panels the Recpoints distribution is shown; it follows the same distribution, apart from a uniform decrease (10%) due to the reconstruction efficiency.

5.6.2 The integrated multiplicity

It is possible to reconstruct the position of the simulated and reconstructed points relatively to the vertex, which is fixed at $V_z = 0$ by the simulation. In particular it is possible to define ϑ as the angle between the beam axis and the line connecting

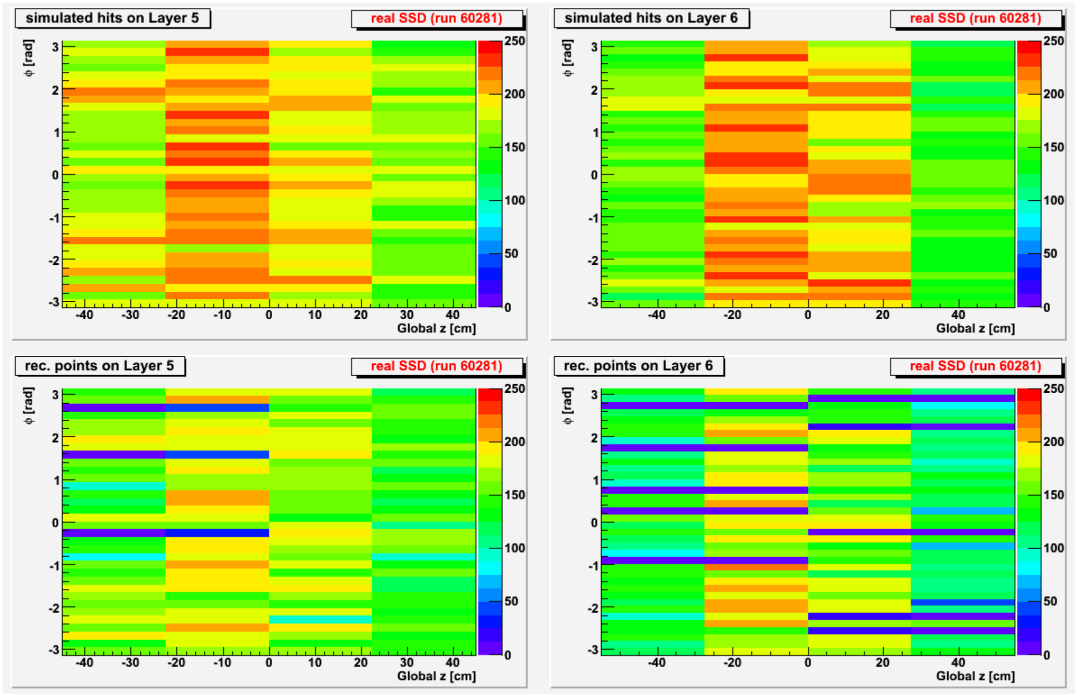

Figure 5.7: Realistic SSD *(run 60281 calibration)*: Hits and Recpoints in the z-φ plane using the real channel noise and functionality map, integrated over 2000 events. The holes in the Recpoints distribution (blue sectors in the lower panels) correspond to the disabled half-ladders.

the point to the vertex. [4]

From the detector point of view, ϑ represents the emission angle, with respect to the z axis, of the particle that generated the point. Therefore, one can define the function

$$\eta = -\ln(\tan(\frac{\vartheta}{2})) \tag{5.2}$$

and interpret it as the reconstructed pseudorapidity of the particle that generated the point.

It is therefore possible to evaluate and compare the total multiplicity in the central unit of pseudorapidity as both for the Hits (*simulated*) and the Recpoints (*reconstructed*). The *reconstructed* to *simulated* ratio is about 0.9 with an ideal configuration of the detector, as can be seen from the comparison between the simulated Hits (*red bin*) and the Recpoints (*black bin*) shown in the left panel of fig. 5.8. In the right panel the same estimation was extracted from the realistic SSD data. Here the

[4] Using the global coordinates we can define the distance between the point and the beam axis as $rad = \sqrt{x^2 + y^2}$ and then the angle $\vartheta = \arctan(\frac{rad}{z})$. This angle defines the direction of the line connecting the point to the vertex with respect to the beam axis.

ratio is suppressed by the large number of *bad channels*, mostly the ones belonging to the disabled ladders.

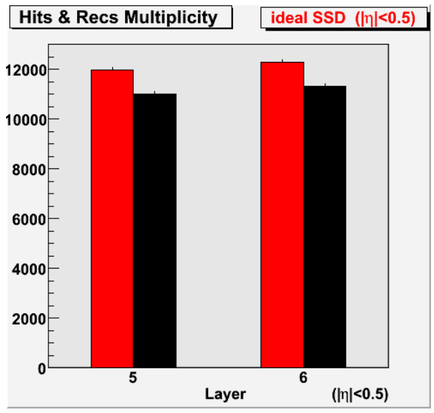

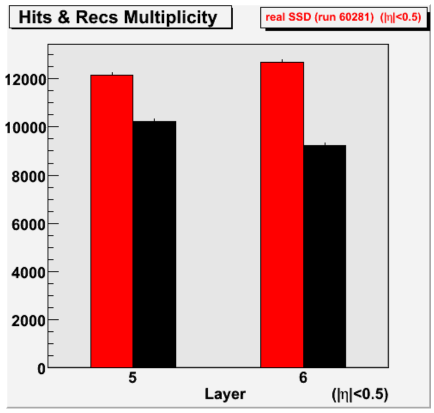

Figure 5.8: Hits and Recpoints total multiplicities in the central pseudorapidity unit ($|\eta| < 0.5$); the ideal SSD case in the left panel, the realistic case (SSD calibrated as in run 60281) in the right panel. The total number of the Hits *(red bin)* generated in the 2000 events of the sample is compared with the total number of Recpoints *(black bin)*. In the realistic case, the Recpoints are suppressed, specially in Layer 6 where 10 ladders were disabled.

5.6.3 The $dN/d\eta$ distribution

In order to characterize the events, it is important to study the charged particle distribution over the η acceptance range covered by the SSD ($|\eta| < 0.9$). Therefore, the η differential distribution of hits and Recpoints multiplicities integrated over the φ coordinate has been calculated. The resulting plots show the effects of the defective regions of the detectors.

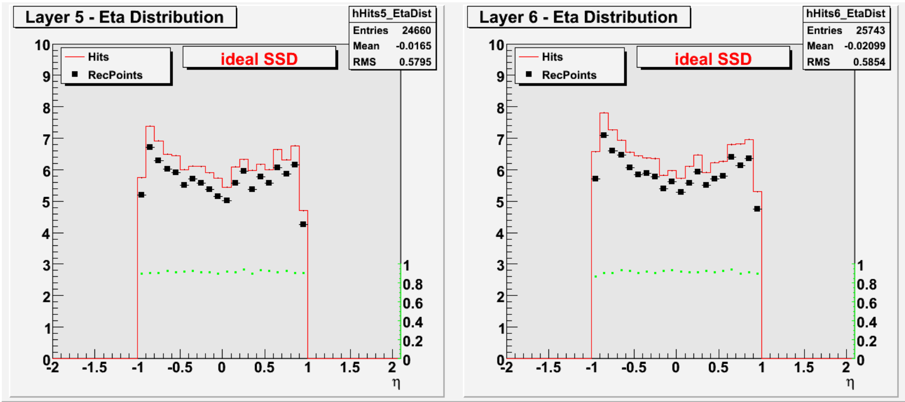

Figure 5.9: Ideal SSD: $dN/d\eta$ distribution of hits *(red line)* and Recpoints *(black squares)*. The reconstruction reaches a 90% efficiency in absence of defects on the SSD along its total coverage range; the *green dots* and the right scale refer to the *reconstructed-to-simulated* ratio.

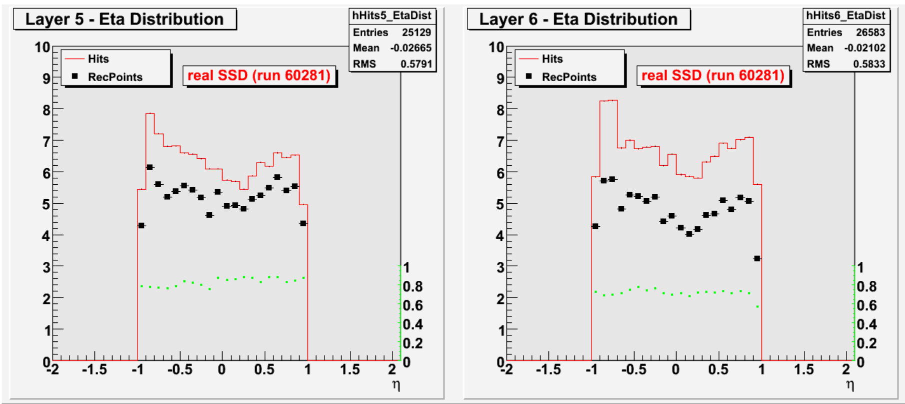

Figure 5.10: Realistic case: $dN/d\eta$ distribution of hits *(red line)* and Recpoints *(black squares)*. Recpoints are unevenly suppressed at η values corresponding to highly defective zones of the detector: the *reconstructed-to-simulated* ratio (*green dots*, right scale) shows a suppression for negative η in Layer 5.

With a perfect detector (see fig. 5.9), the η differential distribution reproduces the results already seen in integrated multiplicity graphs: the point are reconstructed with an 90% efficiency, without any evident distortion within the acceptance range. In figure 5.10 the same distributions are shown for the realistic case. The reconstruction efficiency along η depends on the localization of defects and of disabled ladders. For example on Layer 5, the presence of three disabled half-ladders, all them belonging to the SSD C-Side, causes the suppression of the Recpoints multiplicity for negative η values.

5.6.4 The hits-Recpoints correlation

Another useful index of the measurement reliability has been studied: the correlation of hits and Recpoints multiplicities in the central unit of η (see fig. 5.11).

For each SSD layer, the two-dimensional histograms, according to the color scale, show the density of events with simulated hits (*x-axis*) and reconstructed points y. Fitting the points we obtain the correction to apply to the observed multiplicity to reconstruct the underlying hit multiplicity.

In the ideal SSD case, the histogram points concentrate along the line corresponding to a perfect reconstruction, while in the realistic case they move away from the line and spread out.

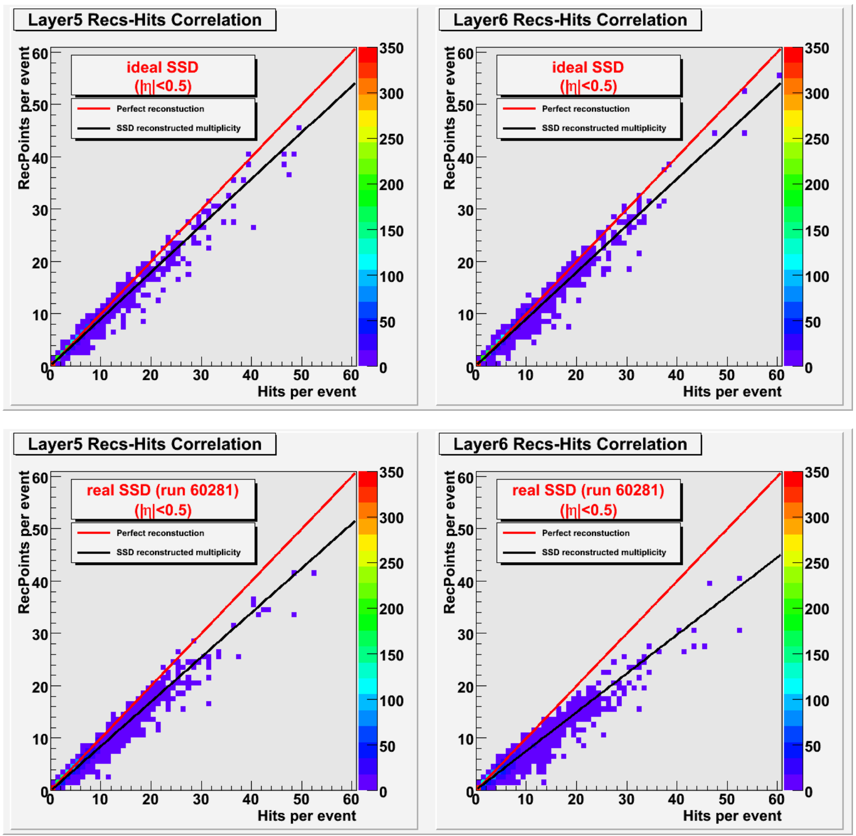

Figure 5.11: Hits-Recpoints correlation in the ideal SSD case *(upper panels)* and in the realistic case *(lower panels)*, for Layer 5 *(right)* and Layer 6 *(left)*. The density of events with simulated hits (*x-axis*) and reconstructed points (*y-axis*) in the range $|\eta| < 0.5$ is plotted. The red line corresponds to a perfect reconstruction, the fit *black line* determines the correction to apply in order to reconstruct the *true* multiplicity.

5.6.5 As a function of the prompt particle multiplicity

Eventually, a preliminary reconstruction of the event global properties has been explored: the number of primary charged particles which were promptly produced by the collision (see fig. 5.12). The Recpoints multiplicity has been studied as a function of this number, that is provided by the Monte Carlo simulator. With the studied geometrical and efficiency corrections, and considering the presence of secondary particles, it is possible to reconstruct the initial multiplicity starting from the space point detected by SSD.

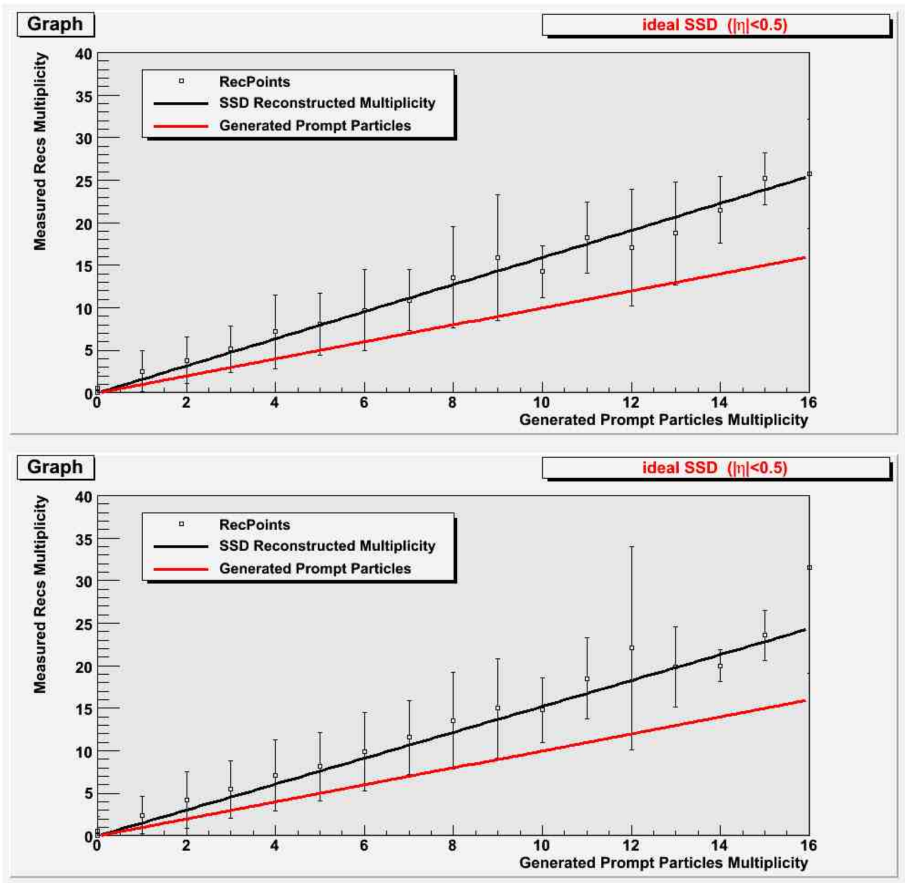

Figure 5.12: Correlation between the measured multiplicity and the number of primary charged particles promptly produced by the collision. Black squares represent the number of reconstructed points in events with the same prompt charge particle multiplicity (x axis). The red line corresponds to the perfect reconstruction of the prompt multiplicity. From the fit (*black line*) it's possible to correct the measure in order to reconstruct the *true* prompt particle multiplicity.

The feasibility study of a multiplicity measurement performed with the SSD has been carried out with a particular emphasis on the efficiency corrections estimation:

the present reconstruction process allows to reach a 90% efficiency in absence of defects on the detector, taking into account only the high quality reconstructed points (*golden Recpoints*) in the final analysis.

Considering the SSD in a realistic configuration, i.e. with the real noise pattern and the real *bad channels* map, the reconstruction reaches the 87% efficiency in the regions presenting less than 10% defective channels, and diminishes with the increasing defects percentage. As it comes from the $dN/d\eta$ study, the disabled half-ladder causes a loss of about 3% to the efficiency in the measurement of the ϕ-integrated multiplicity. Moreover, the possibility to reconstruct the number of prompt charged particles multiplicity with the SSD, once applied the mentioned corrections, has been investigated.

A possible development of this study can concern the analysis of the correlation between points reconstructed on the two SSD layers: the association of these points should allow to reject more efficiently the clusters generated by the noise and to investigate the possibility to separate primary from secondary particles by reconstructing the SSD segments of their tracks.

Conclusions

The physics programme of the ALICE experiment requires very challenging performances to its detector. In order to investigate the Quark-Gluon Plasma formed in the heavy-ion collisions at the LHC energies, ALICE plans to detect, identify and trace an extremely large number of primary and secondary particles over a wide momentum range. The tracking system of the experiment, in particular, is required to accomplish the reconstruction and separation of primary and secondary vertices and the tracking of the produced charged particles with high efficiency and precision.

The thesis is focused on the research activities performed within the production of a part of the tracker, i.e. the Silicon Strip Detector (SSD). The strict performance requirements imposed to keep the quality of the SSD modules close to the full efficiency: the quality of the components before and after each single assembly operation was evaluated and monitored, and their functionality were accurately characterized. An exhaustive and comprehensive test procedure was defined and an extensive campaign of tests and dedicated studies was carried out on the produced devices: besides the monitoring of the production procedures, this protocol allowed to detect a large variety of unexpected defects. Further specific investigations allowed to understand their origin and to find out and apply suitable solutions, with specific processing of the detectors or by implementing proper electronics modifications. Finally, the Trieste SSD group achieved to produce 840 SSD modules, each of them presenting at least 98% properly working channels. This quality level was certified also after the installation of the modules on the detector layers in the final configuration through electrical tests. At the installation in the ALICE experimental site, the detector finally presented only 2% defective channels out of about 2.6 million SSD channels.

The SSD was then completely integrated in the ALICE detector and control systems during the commissioning phase; its capability to detect particles was then tested for the first time through cosmic rays acquisition. This phase allowed on one side to tune and improve the algorithms for the data reconstruction and analysis, on the other to carry out a study of the quality of the acquired data. After a first period of acquisition without filtering the data, the hardware subtraction of the common mode oscillations was introduced, allowing to zero-suppress and consequently reduce the collected data. Several methods of subtraction were discussed and two different algorithms were proposed and tested on real noise data, which proved to be at the same time simple and reliable. One of these common mode correction algorithms is now being implemented in the acquisition hardware and will assure a correct treatment of the first physics data.

In view of the first collisions a simulation study concerning the measurement of the charged particle multiplicity measured with the SSD detector was carried out. The dependence of the measurements on the detector quality was analyzed and the corrections for the acceptance and the efficiency were estimated. This study will thus offer a tool for the analysis of the collision data allowing both to characterize the evolution of the observed events and to monitor the detector efficiency and the quality of the collected data during the experimental activity.

Bibliography

[1] H. Satz, *Colour Deconfinement in Nuclear Collisions*, Rept.Prog.Phys. 63 (2000) 1511

[2] E. Shuryak, *Physics of the first three fermis in high energy heavy ion collisons*, Nucl.Phys. A566 559c-562c (1994)

[3] H. Satz, *Phase Transition in QCD*, Nucl.Phys. A681 (2001) 3-21

[4] S. Gottlieb, *Lattice calculation of the quark gluon plasma*, Journal of Physics: Conference Series 78 (2007) 012023

[5] R. Hagedorn, Riv. Nuovo Cimento 6, 1 (1983)

[6] N. Cabibbo and G. Parisi, Phys. Lett, 59B (1975) 67

[7] F. Karsch, *Properties of the Quark Gluon Plasma: A Lattice Perspective.*, Nucl. Phys. A 783 (2007) 13c-22c

[8] Á. Mócsy, F. Sannino, K. Tuominen, *Confinement versus Chiral Symmetry*, Phys.Rev.Lett. 92 (2004)

[9] V. Koch, *Introduction to Chiral Symmetry*, Laurence Berkeley National Laboratory, (1995)

[10] F. Karsh, E. Laermann, and A. Peikert, *The pressure in 2, 2+1 and 3 flavour QCD*, Phys. Lett. B478, 447 (2000).

[11] J. D. Bjorken, *Highly relativistic nucleus-nucleus collisions: The central rapidity region.*, Phys. Rev. D, Vol. 27, No. 1 (1983) 140-150

[12] U. Heinz, *The Little Bang: Searching for quark-gluon matter in relativistic heavy-ion collisions*, arXiv:hep-ph/0009170v2

[13] Helmut Satz, *The Search for the QGP: A Critical Appraisal*, Nucl.Phys.Proc.Suppl. 94 (2001) 204-218

[14] K.J. Eskola, *On predictions of the first results from RHIC*, arXiv:hep-ph/0104058

[15] K.J. Eskola, K. Kajiantie, P.V. Ruuskanen and K. Tuominen, *Scaling of transverse energies and multiplicities with atomic number and energy in ultrarelativistic nuclear collisions*, Nucl. Phys. B 570 (2000) 379,

[16] D. Kharzeev and E. Levin, *Manifestations of High Density QCD in the first RHIC data*, arXiv:nucl-th/0108006v3

[17] M.Nardi *Hadronic multiplicity at RHIC (and LHC)*, Journal of Physics: Conference Series 5 (2005) 148-161

[18] J. Cleymans and K. Redlich, *Unified Description of Freeze-Out Parameters in Relativistic Heavy Ion Collisions*, arXiv:hep-ph/0104058

[19] V. V. Anisovich1 and M. N. Kobrinsky, *Recent results on anomalous J/psi suppression in Pb-Pb collisions at 158 GeV/c per nucleon*, Phys. Lett. B Vol. 52, Issue 2 (1974) 217-219

[20] F. Antinori et al., *New results from the NA57 experiment*, proc. *The XXXVIIIth Rencontres de Moriond "QCD and High Energy Hadronic Interactions"*, (2003)

[21] E. L. Feinberg, *Direct Production of Photons and Dileptons in Thermodynamical Models of Multiple Hadron Production*, Nuovo Cimento A 34, 391 (1976)

[22] T. Peitzmann, M. H. Thoma, *Direct Photons from Relativistic Heavy-Ion Collisions*, Phys.Rept. 364 (2002) 175-246

[23] The NA50 Collaboration, *A new measurement of J/Ψ suppression in Pb-Pb collisions at 158 GeV per nucleon*, arXiv:hep-ex/0412036v1

[24] H. Pereira Da Costa, for the PHENIX Collaboration, *PHENIX results on J/Ψ production in Au+Au and Cu+Cu collisions at* $\sqrt{s_{NN}}$ *= 200 GeV*, arXiv:nucl-ex/0510051v1

[25] STAR Collaboration (John Adams et al.), *Evidence from d+Au measurements for final state suppression of high p(T) hadrons in Au+Au collisions at RHIC*, Phys. Rev. Lett. 91, 072304, 2003

[26] B. Pastircak, *Status of radiation calculations for mis-injected beam into LHC*, ALICE pres. 31/8/2000

[27] ALICE Collaboration: B. Alessandro et al., *ALICE: Physics Performance Report, Volume II*, J. Phys. G: Nucl. Part. Phys. 32 1295-2040 (2006)

[28] ALICE Collaboration: K. Aamodt et al., *The ALICE experiment at the CERN LHC*, Journal of Instrumentations 3 S08002 (2008)

[29] C. Lippmann for the ALICE collaboration, *The ALICE Transition Radiation Detector*, SNIC Symposium, Stanford, California - 3-6 April, 2006

[30] A. Peisert, *Silicon microstrip detectors*, in "Instrumentation in High Energy Physics", F.Sauli (ed), World Scientific, (1992)

[31] ALICE Collaboration, *ALICE: Technical Design Report of the Inner Tracking System (ITS)*, CERN/LHCC/95-71, (1999)

[32] ALICE Collaboration: F. Carminati et al., *ALICE: Physics Performance Report, Volume I*, J. Phys. G: Nucl. Part. Phys. 30 1517-1763 (2004)

[33] L.Bosisio, I.Rachevskaia, 0.Starodubtsev, R.Weadon, *Test and quality control of double-sided silicon sensors for the ALICE experiment*, 6th International Conference on Large Scale Applications and Radiation Hardness of Semiconductor Detectors - Firenze, (2003)

[34] L. Bosisio, O. Borysov, M. Bregant, P. Camerini, E. Cattaruzza, G. Contin, A. Dyatlovich, E. Fragiacomo, Gacomini, N. Grion, G. V. Margagliotti, S. Naumov, S. Piano, S. Potin, I. Rashevskaya, R. Rui, O. Starodubtsev, *Experience with the Test and Qualification of Double-Sided Silicon Microstrip Sensors for the ALICE Inner Tracking System*, Nuclear Science Symposium Conference Record, IEEE Vol. 3 1429 - 1433, (2006)

[35] D. Bonnet et al., *The HAL25 Front-End Chip for the ALICE Silicon Strip Detectors*, Proceedings of "7th Workshop on the Electronics for LHC Ex-

periments, Stockholm, Sweden, ", September 10-14, 2001 CERN 2001-005, CERN/LHC/2001-034, pp 76-80

[36] C. Hu-Guo et al., *Test and Evaluation of HAL25: The ALICE SSD Front-End Chip*, Proc. of 8th Workshop on Electronics for LHC Experiments, Colmar (France) sept. 2002, CERN-2002-03, ISBN 92-9083-202-9, p135-138

[37] C. Colledani, C. HU, J.D. BERST, *Hal25 User Manual*, IRES - LEPSI, 2002

[38] G. Contin, *Il tracciatore interno di ALICE: Test e caratterizzazione dei rivelatori a microstrip di silicio e dell'elettronica di lettura*, Tesi di Laurea, Universita' di Trieste, 2004

[39] *IEEE Std.1149.1 Testability*, Texas Instruments, Semiconductor Group

[40] M. Bregant, O. Borysov, L. Bosisio, P. Camerini, G. Contin, F. Faleschini, E. Fragiacomo, N. Grion, G.-V. Margagliotti, S. Piano, I. Rachevskaia, R. Rui et al., *The ALICE vertex detector: Focus on the micro-strip layers*, Nucl.Instr.Meth. A569 (2006)

[41] M. Bregant, O. Borysov, L. Bosisio, P. Camerini, G. Contin, F. Faleschini, E. Fragiacomo, N. Grion, G.-V. Margagliotti, S. Piano, I. Rachevskaia, R. Rui, F. Benedosso et al., *Assembly and validation of the ALICE silicon microstrip detector*, Nucl.Instr.Meth. A570 312-316 (2007)

[42] F. Faleschini, *Modules Tester Software v.2 - Documentation*, private communication, 2005

[43] L. Bosisio, *I-V Measurements on SSD Modules*, private communication, 2005

[44] G. Giacomini, L. Bosisio, I. Rashevskaya, O. Starodubtsev, *Noise Characterization of Double-Sided Silicon MicroStrip Detectors with Punch-Through Biasing*, IEEE-NSS 2008 Conference Record, Paper N30-386

[45] R. Kluit, P. Timmer, J. D. Schipper, V. Gromov, A.P. de Haas, *Design of ladder EndCap electronics for the ALICE ITS SSD.*, Proceedings of the 7th Workshop for LHC and Future Experiments, Stockholm Sweden (2001)

[46] R. Kluit, P. Timmer, J.D. Schipper, V. Gromov, P. Kuijer, G.J. Nooren, J. Buskop, A.P. de Haas, *Realization of ladder EndCap electronics for the ALICE ITS SSD.*, Proceedings of the 10th Workshop for LHC and Future Experiments, Boston U.S.A. (2004)

[47] F. Carena, W. Carena, S. Chapeland, R. Divià, J-C. Marin1, K. Schossmaier, C. Soós, P. Vande Vyvre, A. Vascotto, *The ALICE Experiment Control System*, 10th ICALEPCS Int. Conf. on Accelerator and Large Expt. Physics Control Systems, Geneva, 10 - 14 Oct 2005

[48] O. Cobanoglu et al., *The ALICE-LHC online data quality monitoring framework: present and future*, Proceedings of the IEEE RT2007, Real Time Systems conference, Fermilab, Batavia Illinois U.S.A. (2007).

[49] F. Roukoutakis et al., *The ALICE-LHC online data quality monitoring framework*, Proceedings of the Computing in High Energy Physics (CHEP 2007), Victoria BC Canada

[50] M.J. Rossewij, A.P. de Haas, J.A. Wisman, P.G. Kuijer, D. Killian, *FEROM, The ALICE SSD read out system*, Workshop on Electronics for LHC experiments, Amsterdam The Netherlands (2003)

[51] N. Manthos, G. Sidiropoulos and P. Vichoudis, *An Efficient Hardware Design for Rejecting Common Mode in a Group of Adjacent Channels of Silicon Microstrip Sensors Used in High Energy Physics Experiments*, IEEE Transactions On Nuclear Science, Vol. 53, No. 3 (2006)

[52] R.A. Fini, *Multiplicity of charged particles in relativistic heavy-ion interactions*, Nuclear Physics A 749 (2005) 325c-328c

[53] T. Virgili, *Measuring charged particle multiplicity in ALICE*, Journal of Physics: Conference Series 5 105-114 (2005)

[54] J.F. Grosse-Oetringhaus, *Measuring charged particle multiplicity distribution with the ALICE detector*, ALICE-INT-2008-002

[55] The Off-line Project of the ALICE experiment, *The ALICE Offline Bible*, The ALICE experiment, 2007